DOSIMETRY AND APPLICATION OF MAGNETIC NANOPARTICLES AS AN INTRAOCULAR SHIELDING METHOD IN IODINE-125 EYE PLAQUE BRACHYTHERAPY

A Dissertation

SUBMITTED TO THE FACULTY OF THE

UNIVERSITY OF MINNESOTA BY

Courtney Claire Oare

IN PARTIAL FUFILLMENT OF THE REQUIREMENTS FOR THE DEGREE OF

DOCTOR OF PHILOSOPHY

Clara Ferreira, PhD, Bruce Gerbi, PhD

May 2022

For my Uncle David, who fought the good fight.

AWKNOWLEDGMENTS

I am lucky to have not one, but two amazing advisors. Thank you to Dr. Clara Ferreira, a constant stream of guidance and support. Her diligence, creativity, and sense of balance have taught me valuable qualities of a physicist and investigator. A large thank you to Dr. Bruce Gerbi for supporting me in the revival of this project. Without his extensive knowledge and mentorship, this work would not be possible. Thank you to Dr. Yoichi Watanabe for his contributions and guidance in the face of challenges. Thank you to Dr. Jian-Ping Wang for his participation and willingness to support this work. Finally, a warm thank you to Dr. JP Dailey for unwavering support and praise. He has taught me what dedication and successful collaboration look like.

I would like to thank remaining faculty who have sharpened my physics and critical thinking skills over the past five years: David Sterling, Dr. Eric Ehler, Dr. Parham Alaei, Dr. Damien Mathew, Dr. Ngoneh Jallow, and Dr. Jessica Lawrence. I would also like to thank classmates for insightful conversations and friendship. Thank you to the administrative staff for logistical support and positive encouragement.

The deepest thank you to my family. My mother, Laurie, for teaching me confidence and how to work hard. My father, Andy, a steadfast source of reassurance and open ears. My brother AJ, whose kindness, and humor lightens any room. To Michael, for continuous support and commitment. A special thank you to my grandfather, Leslie, a Minnesota alumnus whose wit and dedication to family are unparalleled. To all family and friends who have provided encouragement. I would not be able reach this point without your support.

ABSTRACT

Uveal melanoma is a rare diagnosis but the most common intraocular malignancy. Eye plaque brachytherapy has been the standard of care since the introduction of the Collaborative Ocular Melanoma Study (COMS), which proved excellent tumor control and survival for uveal melanoma patients. Despite these successes, normal tissues of the eye receive excessive dose during treatment that is historically unavoidable. The purpose of this work is to implement a novel intraocular shielding technique to reduce normal tissue dose while maintaining tumor control, using a magnetic plaque and ferromagnetic nanoparticles. The ferromagnetic nanoparticles studied have previously been used intraocularly for retinal detachment. A new application of ferromagnetic nanoparticles is studied.

Previously literature has extensively studied outcomes and incidence rates of normal tissue complications for plaque brachytherapy patients, however a gap exists addressing what normal tissue dose is acceptable to avoid such complications. To answer this question, a retrospective study was conducted with uveal melanoma patients treated with COMS plaques. The conclusions can not only help predict normal tissue complication in the future, but also justify the amount of shielding necessary with magnetite nanoparticles.

A proof-of-concept magnetic plaque was designed to guide ferromagnetic nanoparticles around the tumor, creating a shield for normal tissues. The distribution of ferrofluid was fully characterized with film and Monte Carlo (MC) methods to determine dose distribution throughout the eye. Using a novel film calibration technique, radiochromic film was calibrated using low energy Iodine-125. In addition, the MC-simulated source and COMS plaque were benchmarked to validate the source code and the accuracy of the modeled sources and plaque.

In this work the retrospective study is presented followed by film and MC measured dose distribution in the eye with ferromagnetic nanoparticle shielding. Lastly, the fluid flow and fluid distribution are simulated with multiphysics software. The results can be clinically applied to establish how much shielding is necessary to prevent normal tissue toxicity, and what magnitude of dose reduction is feasible based on the presented proof-of-concept design.

TABLE OF CONTENTS

LIST OF FIGURES

LIST OF TABLES

ABBREVIATIONS AND SYMBOLS

AAPM	American Association of Physicists in Medicine
ABS	American Brachytherapy Society
BMI	Body Mass Index
CI	Confidence Interval
COMS	Collaborative Ocular Melanoma Study
CT	Computed Tomography
EBRT	External Beam Radiotherapy
EFH	Education Series EFH Ferrofluid
EO	Ethylene Oxide
GAMOS	GEANT4-Based Architecture for Medicine-Oriented Simulations
HDR	High Dose Rate
HE	High Equivalence
HR	Hazard Ratio
ICRU	International Commission on Radiation Units and Measurements
ISO	International Standards Organization
LDR	Low Dose Rate
MC	Monte Carlo
MNP	Magnetic Nanoparticle
MRI	Magnetic Resonance Imaging
MVCT	Megavoltage Computed Tomography
NIST	National Institute of Standards and Technology
NOD	Net Optical Density
NRC	Nuclear Regulatory Commission
OAR	Organ at Risk
OD	Optical Density
OOTF	Ophthalmic Oncology Task Force
PDMS	Polydimethylsiloxane
PMMA	Polymethyl Methacrylate
PV	Pixel Value
ROI	Region of Interest
RR	Relative Risk
TLD	Thermoluminescent Dosimeter
TPS	Treatment Planning System
UV	Ultraviolet
VA	Visual Acuity
VEGF	Vascular Endothelial Growth Factor
WAFAC	Wide Angle Free Air Chamber

CHAPTER 1: INTRODUCTION

1.1 Low Dose Rate Brachytherapy in Current Clinical Practice

Brachytherapy, sometimes called internal therapy, uses sealed radioactive sources for delivery of radiotherapy. The prefix brachy- means "short", coinciding with the treatment of tissues at short distances from the source. Brachytherapy is used to treat breast, prostate, cervical, skin, and eye cancers to name a few. Often it is used in combination with external beam radiotherapy (EBRT), surgery, or chemotherapy [1]. The hallmark of brachytherapy is a steep dose fall off around a source, limiting dose to proximal tissues and sparing normal tissue. In addition, treatment time is typically shorter than EBRT, and is usually well-tolerated by patients due to high dose gradients.

Since 1898 with the discovery of radium salts by Marie Curie and William Roentgen's 1895 discovery of X-rays, radium has been the most common source used for therapy. Historically radium sources were constructed as radium-226 (^{226}Ra) needles or tubes and have helped define brachytherapy dosimetry parameters. Radium sources have been replaced with other sources including cobalt-60 (^{60}Co), cesium-137 (^{137}Cs), iridium-192 (^{192}Ir), iodine-125 (^{125}I), gold-198 (^{198}Au), and palladium-103 (^{103}Pd)[2]. Based on their source strengths, half-lives, and size, these sources are especially advantageous for brachytherapy applications.

Brachytherapy sources can be temporarily or permanently implanted. High dose rate (HDR) sources have a dose rate greater than 20 cGy/min in accordance with the International Commission on Radiation Units and Measurements (ICRU) Report 38 [3]. Most often HDR sources are used for temporary implants. Alternatively, low dose rate (LDR) brachytherapy pertains to sources with a dose rate of 0.5-2 cGy/min and are used as temporary or permanent implants.

HDR sources are housed in a remote after loader device, transporting the source via catheter to the treatment site for a defined time. The after loader shields the source when it is not in use to limit occupational and public exposures to Nuclear Regulatory Commission (NRC) limits and contains interlocks to ensure safe treatment. Catheters or applicators are used to transfer interstitial or intra-cavitary sources. Sources can also be placed adjacent to the target area with a skin applicator, or intravascularly (within blood vessels)[4]. Currently, ^{192}Ir is the most used source for HDR brachytherapy and can be used to treat intracavitary tumors such as cervical cancers, or disease sites on the body's surface. LDR sources deliver dose over a longer time than HDR sources, and typically sources are placed interstitially for prostate cancers or sarcomas. LDR procedures are advantageous to the patient as they are completed in one fraction, if not permanently.

Brachytherapy has had many advancements in the previous decade. Combining brachytherapy with improved image techniques including computed tomography (CT), magnetic resonance imaging (MRI), and ultrasound has led to improved delineation of target tissues and source placement. Real time imaging also allows for implementation of adaptive and individualized treatment planning techniques.

1.2 Eye Plaque Brachytherapy for Uveal Melanoma

Each year in the United States 2500 cases of uveal melanoma and 350 cases of retinoblastoma are diagnosed, with twice as many cases in other countries [5]. Uveal melanomas most commonly arise from the choroid of the eye (>80%), and less commonly from the iris or the ciliary body [6]. Ocular melanomas are most often primary, however a small percentage originate from primary cutaneous sites [7]. Primary ocular melanomas have a high risk of metastasis to the liver. Risk factors associated with the onset of uveal melanoma are limited. Individual characteristics such as fair skin, light eye color, cutaneous nevi and freckles, or the inability to tan are associated factors [6–8]. While solar ultraviolet (UV) radiation is a well-known risk factor for

cutaneous melanoma, there is no conclusive evidence to suggest its risk for uveal melanoma. Despite these conclusions, artificial UV light, from welding or use of sunlamps has an associated risk for choroidal melanoma.

Symptoms of choroidal melanoma are dependent on tumor location and size. Upon diagnosis patients describe vision changes, floaters, eye pain, irritation, or intraocular pressure. Additional pressure in the eye may cause secondary retinal detachment. Many tumors (30%) remain symptomless and go years undiagnosed [7]. Choroidal and ciliary body melanomas are dome, or mushroom shaped, choroidal melanomas present as a subretinal mass. Conversely, iris melanomas present as a pigmented lesion on the interior iris and are typically asymptomatic and may be noticed by a patient or during a routine exam. A diagnosis is completed with a slit lamp biomicroscope and ultrasound. Current diagnosis accuracy is remarkably high, about 99%.

Enucleation was primarily used until 1930 when Moore used interstitial radon seeds to treat a choroidal melanoma [9,10]. Later, ^{226}Ra applicators were created, followed by the first eye plaque, using ^{60}Co [11,12]. Later the beta emitter, ruthenium-106 (^{106}Ru) and low energy gamma emitter, ^{125}I plaques were created [13,14]. ^{106}Ru, ^{125}I, ^{103}Pd, and cesium-131 (^{131}Cs) are modern sources used today for plaques (Table 1.1).

Table 1.1 Properties of brachytherapy isotopes [4,15]

Isotope	Emission Type	Average Energy (MeV)	Half-life
^{222}Rn	α	5.49	3.8 d
^{226}Ra	α + γ	4.79, 0.19	1600 y
^{192}Ir	γ	0.38	74 d
^{60}Co	γ	1.25	5.3 y
^{106}Ru *	β	3.54	372 d
^{90}Sr	β	2.27	28.8 y
^{125}I *	γ	0.027	59.4 d
^{103}Pd *	γ	0.021	17 d
^{131}Cs	γ	0.030	9.7 d

* ^{106}Ru, ^{125}I, and ^{103}Pd are currently used in modern eye plaque techniques

In the late 1980's the Collaborative Ocular Melanoma Study (COMS) group (National Institutes of Health, Bethesda, MD) reviewed survival differences among enucleation and eye plaque patients [16]. COMS Report 10 concluded no survival difference among patients with medium-sized tumors (apex height < 10 mm, basal diameter < 16 mm) receiving plaque therapy versus patients undergoing enucleation in a randomized trial [17,18]. The group also standardized the modern COMS plaque consisting of a gold-alloy backing ("Modulay") and a Silastic insert which holds radioactive seeds in place. Modulay backings are manufactured by Trachsel Dental Studio (Rochester, MN), with diameters ranging from 10 to 24 mm, in 2 mm intervals[19]. Grooves in the Silastic insert hold the seeds 1 mm from the scleral surface of the eye. See Figure 1 displaying the side view of a 14 mm COMS plaque.

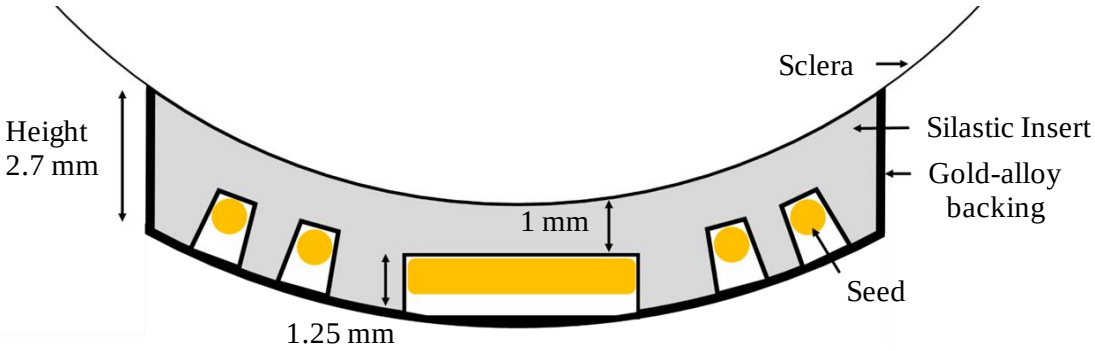

Figure 1.1 A standard COMS plaque, with a gold-alloy backing, and a Silastic seed carrier. The plaque is sutured to fit adjacent to the scleral surface of the eye.

Over the past 25 years the COMS group has published several studies looking at tumor control, treatment toxicity, and quality of life for plaque patients after treatment, especially compared to those who underwent enucleation. COMS Quality of Life Report 3 concluded that patients treated with brachytherapy maintained significantly better vision function than those with enucleation within the first 5 years of treatment [20]. However, patients treated with brachytherapy were more likely to present anxiousness due to the fear of recurrence or metastasis. Based on COMS group findings, plaque therapy become more appealing to uveal melanoma (and

retinoblastoma) patients over enucleation due to eye preservation and vision retention [6,21,22]. Chapter 1.6 expands upon additional treatment methods for uveal melanoma.

1.3 Prescription Dose and Brachytherapy Dose Formalism

In the United States ^{125}I and ^{103}Pd plaques are commonly used sources, while in Europe and Russia, ^{106}Ru and ^{90}Sr sources are popular. The plaque is temporarily sutured to the eye for about 3-7 days. The radioactive seed source strengths are adjusted to achieve the prescribed dose at a defined location. In the original COMS clinical trials, 100 Gray (Gy) was prescribed to 5 mm from the inner sclera, or the tumor apex, whichever is larger [16]. The American Brachytherapy Society – Ophthalmic Oncology Task Force (ABS-OOTF) dose recommendations depend on isotope, but range from 70 – 100 cGy at tumor apex, and that the prescription isodose encompasses the tumor [23]. For COMS plaques, ABS-OOTF recommends following the current COMS standard practice of >60 Gy/h at the tumor apex, with a nominal prescription dose of 85 Gy to the tumor apex or 5 mm from the inner sclera, whichever is larger. Typically, the plaque size is selected by adding a 2 mm margin to each side of the base diameter.

The American Association of Physicists in Medicine (AAPM) Task Group (TG) 43 describes the dosimetry formalism for photon-emitting brachytherapy sources[2]. TG-43 was updated in 2004 to reflect the National Institute of Standards and Technology (NIST) adoption of the air-kerma strength (S_K), rather than apparent activity, as the primary standard[24]. TG-43 presents a two-dimensional (2D) dose formalism (Eq. 1.1) including the dose rate constant (Λ), geometry function ($G(r,\theta)$), radial dose function ($g(r)$), and anisotropy function ($F(r,\theta)$), where r represents distance from the source center, and θ represents the angle from the longitudinal source axis. Each parameter will be described in the following sections for a line source, which best represents encapsulated brachytherapy seed sources, as opposed to a point source. The coordinate system used for brachytherapy dosimetry calculations is illustrated in Figure 1.2.

$$D(r,\theta) = S_k * \Lambda * \frac{G_l(r,\ \theta)}{G_l(r_0,\theta_0)} * g(r) * F(r,\theta) \qquad \text{Eq. 1.1}$$

where $r_0 = 1$ cm and $\theta_0 = 90°$

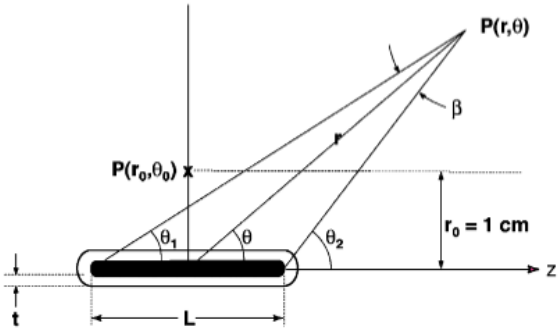

Figure 1.2 Coordinate system for brachytherapy dosimetry calculations
Image is obtained from AAPM TG43 Update 1 [24]

Air Kerma Strength, S_K

Source strength, S_K, is found by measuring the air kerma (K) at a known calibration distance in free space along the transverse axis of the source. The measurement point must be far enough from the brachytherapy source to treat it as a point source. The units of S_K are in U, which is equivalent to 1 cGy cm^2 h^{-1}. Air kerma is measured in vacuo, meaning that air or medium attenuation should be corrected for. The updated version of TG-43 has an revised definition of S_k in which a low-energy cut off value is used to eliminate inclusion of contaminant photons that increase dose at small distance, however, do not contribute to doses at distances greater than 0.1 cm [24]. Typically, this low energy cut off value is 5 keV. Determining air kerma rate at a far enough distance (d) in vacuo and due to photons greater than δ=5 keV, air kerma strength is calculated by Eq. 1.2:

$$S_K = \dot{K}_\delta(d)d^2 \qquad \text{Eq. 1.2}$$

In line with standards laboratories, air kerma strength has largely replaced specification of radiation sources by activity (mCi) or equivalent mass of radium. 1.27 U/mCi can be used to convert from activity to air kerma strength for ^{125}I. The measured exposure rate at a point in space is proportional to the product of the source's activity and exposure rate constant. However, the exposure rate constant must be accurate to determine activity. The quantity of exposure is less commonly being used, thus air kerma strength is the most appropriate definition of radionuclide source strength, as recommend by the AAPM.

Dose Rate Constant, Λ

A source's dose rate constant, Λ, is dependent on the source type and its encapsulation. Λ is the ratio of dose rate at a reference point (r_0 = 1 cm, θ_0 = 90°) and S_k, or dose rate per U. The resulting units for Λ are cGy h^{-1} U^{-1}, or cm^{-2}:

$$\Lambda = \frac{\dot{D}(r_0, \theta_0)}{S_k} \qquad \text{Eq. 1.3}$$

Geometry Function

The geometry factor accounts for the loss of photon fluence at increasing distance from the source, in accordance with the inverse square law. The line source approximation used for brachytherapy sources accounts for changing distance from the source as the measurement point moves along or across the source. The line source approximation is as follows:

$$G_L(r,\theta) = \begin{cases} \dfrac{\beta}{L\, r\, sin\theta} & if\ \theta \neq 0 \\ r^2 - \dfrac{L^2}{4} & if\ \theta = 0 \end{cases} \qquad \text{Eq. 1.4}$$

where L is the active source length, and β is the angle delimited by the tips of the line source at the calculation point (r,θ). Since β is dependent on the active source length, L, it is not included in AAPM TG-43, but is expanded on here:

$$\beta = \sin^{-1}\left(\frac{L\sin\left(tan^{-1}\left(\frac{r\,sin\theta}{rcos\theta - \frac{L}{2}}\right)\right)}{\sqrt{(r\sin\theta)^2 + \left(r\,cos\theta + \frac{L}{2}\right)^2}}\right) \quad \text{Eq. 1.5}$$

The geometry function can therefore be tabulated for each polar coordinate and distance knowing the length of the source [25]. When θ = 90° equation 1.4 and 1.5 can be simplified to

$$G_L(r,\theta_0) = \frac{2\tan^{-1}\left(\frac{L}{2r}\right)}{Lr} \quad \text{Eq. 1.6}$$

Radial Dose Function

The radial dose function describes dose fall off at increasing distance from the source center. The sharp dose fall off is the hallmark of brachytherapy and is largely due to photon attenuation and scatter in the medium and source encapsulation. The radial dose for a line source is defined by Equation 1.7:

$$g_L(r) = \frac{\dot{D}(r,\theta_0)}{\dot{D}(r_0,\theta_0)}\frac{G_L(r_0,\theta_0)}{G_L(r,\theta_0)} \quad \text{Eq. 1.7}$$

where θ_0 is 90° and r_0 is 1 cm. Equation 1.6 may be used to calculate $g_L(r)$ at various distances (r) along the transverse axis, but many treatment planning systems (TPS) utilize a fifth order polynomial to fit the radial dose function, avoiding interpolation [24]. According to the AAPM, the fitted polynomial parameters should agree within two percent of the data. Additionally, a fitted radial dose curve should only be used for the range for which it was originally fitted.

Anisotropy Function

The 2D anisotropy function describes the change in dose as the polar angle changes along the transverse plane. At 90 degrees, the anisotropy function is unity. The function decreases as θ nears 0 or 180 degrees, toward the seed ends, as seed encapsulation thickness increases. Equation cis 1 cm:

$$F(r,\theta) = \frac{\dot{D}(r,\theta)}{\dot{D}(r,\theta_0)}\frac{G_L(r,\theta_0)}{G_L(r,\theta)} \qquad \text{Eq. 1.8}$$

Each dosimetry parameter has existing consensus data for each radionuclide source and model, which can be adopted by users for clinical treatment and research. Consensus data is a compilation of Monte Carlo (MC) studies and dosimetric measurements in literature evaluated by the AAPM.

1.4 Dose-Related Side Effects in Eye Plaque Brachytherapy

The ABS recommends a nominal prescription dose of 85 Gy in a homogenous medium at 5 mm depth for COMS ^{125}I plaques [2]. Since the plaque is placed on the scleral surface of the eye, normal ocular tissues may receive high radiation doses. Damage to the macula, optic disc, lens, and sclera may cause further vision complications. The following sections will address recognized side effects and the known mechanisms of radiation-induced damage, incidence, and studied dose limits for radiation retinopathy, cataracts, and scleral necrosis.

Radiation Retinopathy

Upon exposure to radiation, the retina experiences non-proliferative changes including occlusive vasculopathy in all eyes treated with ^{125}I [26,27]. Eventually, severe ischemic necrosis may lead to vision loss. Proliferative radiation retinopathy is experienced as angiogenesis, in which

growth factor production compensates for weakened blood vessels and is experienced by 6% of patients. For juxtapupillary choroidal melanomas (within 1 mm of the optic disc) it is reported that after 5 years over 66% and 24% of patients experience non-proliferative and proliferative retinopathy, respectively [28,29]. Radiation retinopathy can also present as cystoid macular edema.

Radiation maculopathy is type of retinopathy related to the macula, while radiation optic neuropathy is related to the optic nerve. Both incidences of retinopathy are more likely to occur with high radiation doses, and tumor proximity to the macula and optic disc. In addition, eyes with larger tumor heights and volumes are more likely to experience retinopathy. Radiation dose to the optic disc is associated with optic neuropathy and vision loss [30–33]. Dose tolerances to the optic nerve have been reported to range between 30-60 Gy, and a limit 50 Gy is the current clinical standard for fractionated EBRT [30,32,34–36].

Cataracts

Cataracts are one of the most common and well-studied complications in eye plaque brachytherapy. Radiation damage to protective enzymes of the lens causes opacity, and related vision loss. COMS Report 27 observed that within the first 5 years of follow-up, 68% of the studied eyes developed cataracts [37]. Beyond 5 years, 83% of eyes were reported to have cataracts. Additional retrospective studies have found cataract incidence rates ranging from 24 – 60% [32,33,38]. The variability seen across studies may be due to the proximity of studied lenses, radiation doses, tumor size, or the inclusion of patients with previous cataracts and lens replacement procedure. COMS Report 27 found a relationship between lens dose and cataract formation. 18% of lenses receiving a dose of 24 Gy or more underwent cataract surgery, while only 4% of patients with lens dose below 12 Gy underwent cataract surgery. Previous external beam studies have found cataract formation is unlikely below 10 Gy, and extremely unlikely at doses below 5 Gy [39,40]. However, EBRT biological dose differs from dose received by low dose rate sources.

Scleral Necrosis

The sclera is an avascular structure in the eye, making radiation-induced damage very rare, and occurring with extreme dose levels [26]. Patients with scleral necrosis experience dry eye, and pain years after irradiation. The mean onset time has been reported between 49 and 70 months after plaque treatment, however most cases occur within the first 5 years [41,42]. Patients with larger tumor heights are more likely to experience scleral necrosis, as increasing tumor height requires increased dose rate to achieve the desired prescription dose. In the formerly mentioned study, Kaliki et al., found a significant relationship between incidence and scleral dose ≥ 400 Gy (P = 0.0455), while Radin et al. studied 23 patients experiencing scleral necrosis with a mean of 223 Gy to the tumor base (sclera) [41,42]. Eyes with scleral doses greater than 400 Gy should be closely monitored post-treatment.

In addition to the side effects listed above, secondary glaucoma, vitreous hemorrhage and retinal detachment are possible. Secondary glaucoma occurs in less than 15% of treated eyes and is due to similar factors as retinopathy: angiogenesis, inflammatory factors, and ischemia [26,29,32,33]. If untreatable, added pressure and pain in the eye may cause concern for enucleation. A vitreous hemorrhage or retinal detachment are due to lost adhesion of the retinal and scleral layers. Many cases of uveal melanomas are diagnosed with a preexisting vitreous hemorrhage or retinal detachment due to the choroidal tumor mass. In addition, radiation impacts the surrounding tissue, increasing the possibility of hemorrhage or detachment after treatment. After 5 years, about 15% of patients experience vitreous hemorrhage, while less than 2% experience retinal detachment.

The above side effects lead to changes in vision that may diminish a patient's quality of life. While survival outcomes are excellent for plaque brachytherapy, a large majority of patients experience a decline in visual acuity (VA) [16–18]. COMS Report 16 found that 49% of treated eyes experience a VA decline of 6 Snellen lines or more within 3 years of treatment [29,33,38,43].

Additionally, 43% of eyes declined to a VA of 20/200 or worse, the clinical definition of blind. To improve a patient's quality of life, strategies have been implemented to reduce side effects discussed.

1.5 Side Effect Reduction Strategies in Eye Plaque Brachytherapy

Strategies to alleviate side effects can be grouped into two categories, preventative and responsive. Preventative strategies work to reduce dose to normal tissues in the planning process and at the time of treatment. Reducing dose to normal tissues would prevent tissue damage from radiation, and ideally can alleviate negative side effects experienced by patients. The second type of strategy is responsive to side effects as they arise month to years after treatment. The following sections will detail current practices based on these two approaches.

Preventative Strategies

Preventative strategies are becoming more commonly researched to spare normal tissue, while achieving adequate cell kill. Shielding materials are used to attenuate dose to sensitive tissue in EBRT. Examples include tungsten lens shields placed on the eye or gonadal shielding in extraordinary circumstances. Due to the intraocular nature of uveal melanoma, however, such techniques are not applicable to the eye. In one intraocular shield attempt iodine contrast substances were originally studied in the 1990's as an intravitreal shielding mechanism, effectively absorbing ^{125}I photons, however evident toxicity was noted [44].

Another material studied for intravitreal ^{125}I shielding is 1000-centiStoke silicone oil, a common vitreous replacement material. The study found that compared to a saline solution, the 17 mm of silicone oil attenuated 48% of the photons emitted from an ^{125}I seed [34]. Ex-vivo thermoluminescent dosimeter (TLD) measurements in cadaver eyes, with a plaque placed 7.6 mm from the optic nerve, showed that the silicone oil attenuated 25- and 35% of the dose at the macula

and optic nerve, respectively. Structures further away from the plaque benefited from the most attenuation. Case-controlled studies found reduced rates of radiation retinopathy for silicone oil eyes [45,46]. While significant attenuation was seen with silicone oil, it was least effective for structures close to the plaque, which are typically structures in need of dose reduction. Additionally, a complete vitrectomy is required, causing higher likelihood of cataracts due to oxygen exposure to the lens. Additionally, removal of the vitreous fluid may increase complication rates of retinal detachment. Overall, silicone oil eyes found less damage to the optic disc and macular region, showing the effectiveness of the preventive strategy, but this comes with risks of a more involved surgical technique.

Gold nanoparticles that have a high atomic number (Z) represent an additional preventative strategy, encouraging dose enhancement at the tumor location. The photoelectric effect explains how the number of interactions increases for decreasing energies, and increasing atomic number [47]. Photons with low energies transfer energy entirely to tightly bound electrons during collision with an atom. Since high-Z materials contain tightly bound electrons the photoelectric effect is most common with high atomic number atoms and low energy photons. When gold (Z = 98) nanoparticles are latticed inside an ocular tumor, low energy photons and the photoelectric effect will increase dose to the tumor, requiring a lower prescription dose. Therefore, normal tissues can be spared when using the dose enhancement properties of gold nanoparticles. Rezaei at al. showed that a dose enhancement factor of 1.44 is achievable for gold nanoparticles in the presence of a Pd-103 COMS 20 mm eye plaque [48]. In vitro studies would be necessary to supplement these Monte Carlo findings. Biocompatibility of gold nanoparticles has been studied in the eye and is dependent on size - particles smaller than 30 nm showed cytotoxicity through in vitro studies [49].

Responsive Strategies

Cataract formation is one of the least concerning side effects after radiation therapy due to the wide availability of lens replacements. The minimally invasive procedure is common with aging as well as a corrective method after vitreoretinal complications. Over 95% of cataract patients report vision improvement after lens replacement surgery [26]. On the other hand, retinopathy and maculopathy are much more complicated to treat.

Retinopathy can be managed upon diagnosis with laser therapies, and photodynamic therapy. Laser therapy and photocoagulation attempt to reduce neovascularization present due to radiation [50]. Photodynamic therapy also resolves neovascularization, using systemic infusion of verteporfin and a laser to target verteporfin-bound choroidal neovascular membranes. Laser therapy can also treat macular edema, and studies have shown improved short term vision outcomes in edema patients undergoing laser treatment. Unfortunately, laser therapy treatments use many parameters making comparison across studies difficult. Between such differences and lack of follow-up data, it is unclear if laser therapy has long term vision benefits.

Antibody blocking agent, Anti-VEGF (vascular endothelial growth factor) has proven useful in preventing radiation toxicity in sensitive normal tissues by eliminating underlying toxicities such as edema. Anti-VEGF can treat macular degeneration and radiation induced retinopathy by reducing edema and retinal hemorrhages [51–53]. One downside to anti-VEGF treatments is the frequency of injections, every 6-8 months following the onset of retinopathy. Moreover, steroids such as triamcinolone and dexamethasone implants have had success in reducing macular edema and optic neuropathy after treatment [26,50]. Steroids and Anti-VEGF therapies may help treat unwanted side effects of radiation.

Radiation retinopathy remains the most common side effect with variable effectiveness from therapeutic modalities. While responsive methods to alleviate retinopathy or maculopathy upon diagnosis are common, there is a strong need to improve preventative methods. More

aggressive strategies need to be implemented to improve prognosis for patients undergoing plaque therapy.

1.6 Alternative Treatment Modalities for Uveal Melanoma

Based on findings in the COMS group studies, most primary uveal melanomas are treated with plaque brachytherapy, however alternate forms of radiation include Gamma Knife® and charged particles (historically helium ions, but more recently protons). Large tumors (base dimension >16 mm, height >10mm), or tumors whose location may not physically be suitable for plaque brachytherapy are the best candidates for charged particle therapy.

Helium ion therapy has shown excellent control rates (> 95% after 15 years), due to the sharp dose fall off beyond the target [54]. This type of therapy is preferred for large tumors or those near the optic disc (juxtapupillary or circumpapillary tumors) where plaque placement is physically challenging. Notched plaques are useful for juxtapupillary tumors, especially with modified seed loading as described by Lee et al., however dose to the optic disc still remains high [22]. One prospective randomized study compared helium ion to plaque therapy, and found that helium ion patients had improved control and survival outcomes [55][56]. However, glaucoma and/or cataract formation were significant for patients with >50% of lens in the treatment beam. Additionally high rates of vision loss were noted; after 4 years, over 50% of patients had onset of vision loss, while after 10 years 66% of patients were legally blind. These rates show that normal tissue damage is prominent due to the beam entrance dose in helium ion therapy. Due to excessive costs, helium ion therapy is no longer available in the United States[57].

After 1985 proton therapy became the charged particle of interest for uveal melanoma. Proton therapy is hypothesized to be advantageous, especially to peripheral tissues of the eye due to sharp dose fall off. Higher rates of tumor control are achievable with proton therapy, and survival rates are comparable to plaque brachytherapy[58]. Similar to helium ions, protons are preferred for

large tumors, or juxtapupillary tumors that fall too close to the optic disc. An anterior entrance dose is required, even for anterior tumors leading to toxicities, especially cataract formation. Additionally, after 8 years chances of conserving vision of 20/40 and 20/200 were only 32% and 42%, respectively [58]. Proton therapy is steadily gaining availability, but for many institutions the limited expertise and necessary capital curb its feasibility. Only 13 centers globally offer charged particle therapy for ocular melanoma [55]. For proton therapy to be the primary method of care, it must be available to patients, be cost effective, and be able to treat melanomas of all size and location without excessive side effects.[59] To date, these criteria are not met.

Gamma Knife® has excellent control rates (94%), comparable to COMS plaques, and a low enucleation rate of 7% [60]. It is predicted that the complication rate (for radiation retinopathy, cataracts, or vitreous hemorrhage) from Gamma Knife® surgeries are near 40%, and some studies, this probability increases to 75%. Such a high rate of complications brings concern, since Gamma Knife® is becoming the most cost-effective treatment strategy due to the single fraction dose, and the outpatient procedure format. The best treatment method depends on the size and location of the tumor, in addition to resources available to the patient.

1.7 GEANT4-based Architecture for Medicine-Oriented Simulations (GAMOS)

In recent decades the use of Monte Carlo (MC) dosimetry has become a commonplace tool for simulation, treatment planning, and dosimetry calculations in radiation oncology and radiology applications [61,62]. MC simulations aim to make sense of randomness, by performing events millions or billions of times. For example, flipping a two-sided coin one million times would give an accurate estimate of probability. This idea can be applied to other random events, including radiation interactions. The term MC originates from the popular casino in Monaco, connected to randomness and odds.

The use of MC calculations has dated back to the 1700's and became increasingly useful in the early twentieth century [63]. During World War II, the Manhattan project was the first application of nuclear interactions, used to simulate neutron interactions through shielding. MC simulations are advantageous for problems that are too large to solve analytically, or in cases where experimentation is too costly or impractical. Disadvantages include the necessary computing resources, and those solutions are reflective of the model which can be prone to errors. Again, MC calculations are only an estimate, and analytical or experimental approaches should be considered along with utilizing simulations.

Geant4 is a toolkit for physics simulation of particle interactions with matter, with a flexible and user-friendly framework [64–66]. Applications of Geant4 range from high-energy physics, astrophysics, and radiation shielding and medical physics. Geant4 can be used alone, or it can be used with software tools such as GAMOS (Geant4-based Architecture for Medicine-Oriented Simulations) for increased functionality. GAMOS allows the user to create a custom geometry and materials, including many predefined NIST materials. The GAMOS generator can consist of single particles or isotopes defined by time, energy, direction, position and/or volume. The physics list is chosen by the user and defines particle types, their energy loss, range, and cross-section tables.

In GAMOS, an original particle is defined as an "event," and each interaction or "track" is followed for the particle until the particle's energy falls below the user-set production cut. Determining the correct energy cut off can help a user save time in simulations, but caution should be taken to ensure that errors are not introduced with the elimination of low-energy particles. GAMOS offers functionality to measure energy, kerma, or dose in the user-defined geometry making it an excellent software option for MC calculation.

TG-268 and TG-43U1 provide recommendations for reporting parameters and utilizing MC dosimetry in brachytherapy[24,67]. TG-268 provides a template for reporting MC parameters

and transport codes utilized for transparency in publications and reports. TG-43U1 recommends using adequate histories to ensure that results have $1\sigma \leq 2\%$ for $r \leq 5$ cm, and for S_k calculations $1\sigma \leq 1\%$. MC calculated results should be confirmed with physical measurements. MC statistics represent the precision of calculations, but do not predict the accuracy of the simulated results.

1.8 GAFCHROMIC® EBT3 Film Dosimetry

Radiochromic film is a widely popular dosimetry tool due to its excellent spatial resolution and subsequent ability to evaluate high gradient radiation fields. When calibrated, radiochromic film is easy to manage and provides absorbed dose values. Radiochromic film is self-developing and does not require processing after exposure [68]. After exposure to radiation, polymerization of diacetylene molecules occurs, forming polydiacetylene dye, turning the film blue with increasing dose [69,70]. GafChromic EBT3 film is a model ideal for brachytherapy sources, with two substrate layers directly attached to the active layer. AAPM Task Group 235 considers EBT3 a Type 3 film configuration, as shown in Figure 1.3.

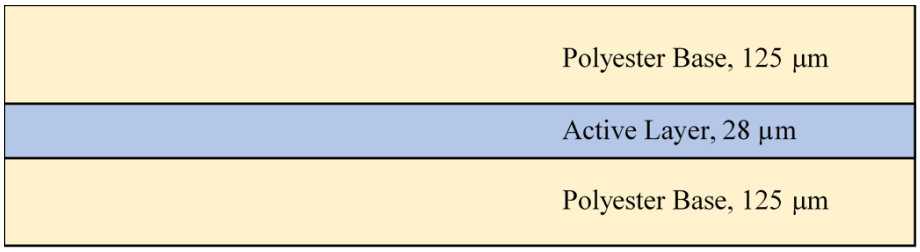

Figure 1.3 EBT3 Gafchromic dosimetry film structure. The film contains and active layer with marker dye, surrounded by two polyester substrate layers. The layered design prevents water from diffusing into the active layer, except at the edges of the film.

EBT3 GafChromic film has excellent spatial resolution, as low was 25 μm, and operates at temperatures up to 60°C. EBT3 film has a useful dose range from 0.1 to 20 Gy. Additionally, EBT3 film is water resistant, except at the edges of the film, where water diffuses into the active layer. GafChromic film is advantageous as it has nearly energy dependent in the 100 keV to the MV

range. Additionally, film composition is nearly tissue equivalent (EBT3 Z_{eff} = 7.26, vs. water Z_{eff} = 7.42. At energies below 100 keV for brachytherapy sources such as ^{125}I, a separate film calibration is needed.

Absolute dose to film is measured by the change in optical density (OD). OD can be determined with:

$$OD = log\frac{I}{I_0} \quad \text{Eq. 1.9}$$

where I is the intensity of light transmitted through exposed film, and I_0 is the intensity transmitted through unexposed film. A flatbed scanner with RGB capability can be used to for GafChromic film using dose-response curves in each color channel. The pixel value (PV) is obtained from scanned film and can be used to create a dose response curve Equation 1.10 gives the calculation for determining optical density based on PV and a 16-bit scan for each color channel:

$$OD = log_{10}\left(\frac{65535}{PV}\right) \quad \text{Eq. 1.10}$$

It is important to measure the OD of a background, or 0 cGy, film piece to obtain the net optical density (NOD). A calibration curve is used to convert measured OD to dose, using a fitted equation. Equation 1.11 is the recommended fit for a dose response curve using GafChromic film:

$$NOD = a + \frac{b}{Dose - c} \quad \text{Eq. 1.11}$$

where a, b, and c are fitted parameters. The red channel curve yields the best result for dose values up to 10 Gy. A larger dose range can be achieved using all three-color channel dose-response curves.

It is recommended to wait 24 hours to read out film. There exists some change in OD within the first 24 hours of irradiation, and afterward studies have shown only a 2.5% change from 24 hours to 14 days post-irradiation. Additionally, studies have shown lateral dependence of film orientation during scanning, likely due to the orientation of crystals in the active layer. For this reason, it is recommended to scan film in the same orientation and side, and in reproducible positions on the scanning bed. Finally, unused film should be stored in a cool, dark place to avoid altering the background exposure, or altering film characteristics.

1.9 Magnetic Nanoparticles in Medicine

Magnetic nanoparticles (MNPs) are more commonly studied in medical applications and are increasingly introduced into clinical practice. Common applications include targeted drug delivery, imaging contrast agents, hyperthermia treatment, magnetic imaging, and diagnostic techniques [71–73]. MNPs offer many unique traits – they can be manipulated and detected by magnetic fields, they have a high atomic number, and they have a large surface area to volume ratio. When placed in an external magnetic field, the particles will orient in the given direction, and when removed from the external magnetic field, particles return to a random orientation state. Additionally, they have a reactive surface, meaning biocompatible coatings or functional groups for cellular targeting [74]. There are still gaps in knowledge about MNPs, and further applications to be discovered. A few applications are described.

Drug delivery with MNPs was proposed as early as the 1970s [72]. A drug can be contained within or coupled to the surface of MNPs and distributed to a site with an externally applied magnetic field. For example, magnetically directed enzyme and drug therapies can be used to treat many conditions including prostate cancer and retinal disease [74,75]. Specific targeting has led to the use of MNPs in hyperthermia treatments for cancers, by increasing targets to 40-43℃, enhancing the cell-killing effects in radiation therapy and chemotherapy [76]. When exposed to an

alternating magnetic field, the particles produce heat. Magnetic hyperthermia has been used in clinical trials ranging from head and neck cases, superficial tumors, melanomas, and cervical cancers. Moreover, MNPs are widely used as an FDA approved imaging contrast agent in MRI for bowel, liver, spleen, and lymph node imaging [77].

MNPs have previously been used in the eye for targeted retinal drug delivery, as well as an internal magnetic tamponade for retinal detachment. In the case of retinal detachment, a magnetic tamponade would allow repair at any location in the eye [78]. Iron oxide (Fe_3O_4) nanoparticles with polymer stabilizers known as polydimethylsiloxane (PDMS) are injected into the vitreous fluid, and directed toward the magnetic tamponade, promoting repair of the detached retina (Dailey et al. 1999; Mefford et al. 2007; Riffle et al. 2008). After reattachment, the fluid is removed from the vitreous fluid. The magnetic fluid was tested in rabbit eyes, finding no cellular toxicity [82,83]. The non-Newtonian nature of the fluid is advantageous as it can be injected through a small syringe. A microscopic view (10X) of this ferrofluid shows the clusters of magnetite nanoparticles (circular shape) suspend by PDMS stabilizers (Figure 1.4). The very bright white spots show a small amount of air bubbles in the sample, while the circular shapes are the magnetite nanoparticles.

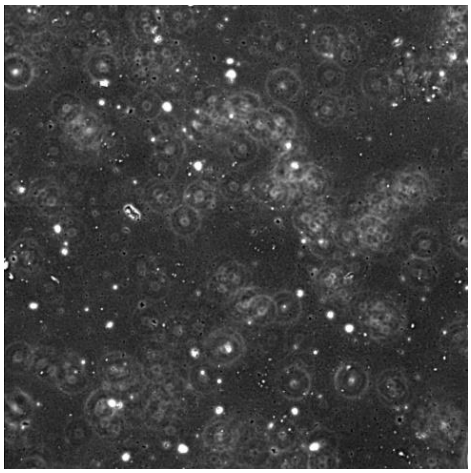

Figure 1.4 PDMS-Fe_3O_4 nanoparticles under a 10x microscope.

While MNPs are a new frontier in medicine, safety and toxicity concerns should be addressed before approval of the drug, device, or treatment. As mentioned before, the affinity of MNPs for functional groups and protective coatings allows particles to be non-toxic and biocompatible [71]. Several studies have been performed using rabbit eyes and cell cultures, finding no toxicity or negative side effects [82–85]. Biocompatibility depends on the duration of use, location, and patient population. The International Standards Organization (ISO) has created guidelines for medical devices, and describes biocompatibility as "ability of a medical device or material to perform with an appropriate host response in a specific application" [86]. The FDA has highlighted how to use ISO guidance to perform physical, in vitro, and in vivo testing [87].

1.10 Multiphysics Simulations

COMSOL Multiphysics software is widely used in science and engineering applications to model or solve problems [88]. A variety of user interfaces are available with the ability to create a user-defined geometry, material properties, and boundary physics conditions.

1.11 Specific Aims

The primary aim in clinical radiation therapy practice is to achieve balance between tumor control, and sparing dose to normal tissues. In eye plaque brachytherapy, survival and tumor control rates are excellent, however many patients endure normal tissue toxicity due to high doses to sensitive structures. Therefore, to improve visual outcomes in ^{125}I plaque patients, it is proposed to utilize PDMS magnetite nanoparticles with a magnetic plaque as an intraocular shielding device during ^{125}I eye plaque therapy. Unlike previous shielding strategies with silicone oil, only a small volume of high-Z material would be required, making the proposed technique advantageous.

An institutional retrospective study addressed the gaps in literature to identify a magnitude of dose reduction to improve normal tissue toxicity rates. In addition, the fluid's attenuating abilities were fully characterized with film dosimetry and MC simulations. Finally, a prototype

device was created to evaluate MNP dose reduction to normal tissues and elimination of side effects.

1.12 Description of Forthcoming Chapters

Chapter 2 outlines the materials and methods used for each aim. The retrospective study data collection and statistical tests are thoroughly described. The film calibration as well as measurements set ups are explained. In addition, MC simulation geometries and methodology for benchmarking and measuring and ^{125}I source and loaded COMS plaque are explained.

Chapter 3 presents the results of the retrospective COMS study for the statistical tests performed. The patient population demographics are presented in addition to key findings and noteworthy results that impact the shielding requirements of a high-Z intraocular shielding device.

Chapter 4 presents film and MC simulation results. Film calibration results and MC source and plaque benchmarking data are presented. Film measurements are compared to similar MC simulation results as a benchmark, but also presenting the dose reduction potential of a high-Z intraocular shielding device. The attenuation and HVL of the PDMS fluid are presented in addition to the dose reduction throughout the eye and ocular structures. The limitations of the studies are also discussed.

Chapter 5 introduces COMSOL multiphysics simulation. Input parameters, materials, and components are described, and the simulated fluid flow is shown.

Chapter 6 addresses the main findings, and significance of this work. The clinical relevance and need for the high-Z intraocular shielding device is justified based on the results across the presented aims. Future work and development prior to clinical use of the shielding device is discussed.

CHAPTER 2: METHODOLOGY

2.1 Retrospective Study: Materials and Methods

A single-institution retrospective study was conducted to evaluate uveal melanoma patient outcomes with respect to normal tissue dose. Patient charts were reviewed for all COMS plaque patients treated between 2005 and 2019 at the University of Minnesota Medical Center. Patients with less than 5 months of follow-up data were excluded from the study, as well as patients that underwent enucleation. Of the 74 COMS patients, 52 met the inclusion criteria and were used in the analysis.

2.1.1 Demographics and Data Collection

Upon receiving IRB approval, demographic data was recorded for each patient including age, sex, body mass index (BMI), smoking status, and laterality (i.e., right, or left eye). The patient's best corrected visual acuity (VA) before treatment was recorded and noted as the baseline vision. A VA of 20/200 or worse is considered blind based on the legal definition in the United States [89]. Preexisting conditions were recorded including glaucoma, macular degeneration, cataracts, vitreal and retinal detachment. Patients with a history of lens replacement for cataracts were excluded from cataract data and results.

Follow-up visit data was recorded including measured VA, the physician's impression of radiation retinopathy, cataracts, glaucoma, or macular degeneration. Change in vision was recorded as the difference between baseline and follow-up VA. One to five Snellen lines lost since baseline was noted as 'Mild VA Decline,' and 'Moderate VA Decline' was recorded for a loss more than five Snellen lines. A patient was considered blind if their VA reaches 20/200 or worse, and they were not blind prior to treatment.

To begin the treatment planning process, fundus photographs were obtained by the ophthalmologist to determine tumor base dimension and distance the lens, macula, and optic disc. Ultrasound images are used to determine tumor height. Using the plaque coordinate system as described by Kline et al., with the origin at the inner sclera, the measured dimensions are used to define normal tissue coordinates [90]. Doses are calculated as point dose to water utilizing the treatment planning system (TPS) (BrachyVision, version 11.0.47, Varian Medical Systems, Palo Altos, CA). 85 Gy was prescribed to 5 mm depth, or the tumor height, whichever was greater, as recommended by the ABS [23].

2.1.2 Statistics

Several statistical tests were performed to relate outcomes to dose and distance of organs at risk (OAR). A univariate (t-test) analysis, relative risk (RR) analysis, Kaplan-Meier hazard ratios, and logistic regression were performed and are described in the following sections. For each test performed, it was hypothesized that a large dose or small distance to an OAR was related to incidence of negative outcomes.

Univariate Analysis

A univariate analysis was performed to find toxicities that had a significant ($p \leq 0.05$) relationship to demographics or treatment parameters, such as dose or distance to an OAR. A one-sided, two sample t-test was performed for each demographic-, dose-, and distance-toxicity relationship. It was hypothesized that increasing dose (or decreasing distance) would be related to worse outcomes. For example, the dose to the macula was evaluated between two groups of patients: those who developed radiation retinopathy and those who did not. To account for preexisting conditions, the analysis was repeated without patients that had glaucoma, macular degeneration, or retinal detachment. Results that remained significant after accounting for

confounding variables were considered robust. A p-value adjustment is not desirable for this dataset due to the exploratory nature of the study and the sample size [91].

Relative Risk Analysis

A relative risk (RR) estimate compared the proportions of two groups (high vs. low dose/distance) developing an unwanted toxicity. Dose above and below the median dose (or distance) defined high and low dose groups. The null hypothesis states that the 95% confidence interval (CI) contains 1.0. If the null hypothesis is rejected, there exists a significant ($p \leq 0.05$) risk estimate. Relevant OAR dose, distance, and demographics and toxicities were evaluated. Cofounding variables, preexisting conditions were accounted for with sensitivity tests.

Kaplan-Meier Hazard Ratio

For variables with significant RR, Kaplan-Meier cumulative incidence curves were created to show toxicity overtime among high and low dose groups. Again, high, and low dose groups are defined as above or below median dose to the OAR to maintain equal group size. Upon death or lost contact, patients were censored. Log rank tests were used to determine the significance of the incidence curves, in addition to hazard ratio. Hazard ratio is different than relative risk as it takes time of the event (toxicity) into account by comparing incidence rate. A single time to event was evaluated for each patient. Univariate, relative risk, and Kaplan-Meier statistical analyses were performed in Microsoft Excel (version 2202) using the Data Analysis toolkit and the StatPlus add on (version 7.6.5.0, AnalystSoft Inc.).

Logistic Regression

For variables with significant hazard ratios, a logistic regression was performed to visualize the predicted probability of toxicities with increasing dose. A spline regression with R statistical software (version 4.0.5).

2.2 Development of a Magnetic Plaque

The primary goal of this work is to characterize PDMS-Fe_3O_4 as a shielding material in the presence of a magnet. As mentioned in chapter 1.9, the non-Newtonian nature of PDMS makes it easily transferrable through a small syringe. A custom, magnetic COMS plaque was designed with this goal in mind, without altering the treatment planning process substantially.

A convex magnet was designed to fit inside the COMS gold-alloy backing. The custom magnet (N52-Grade, Sintered NdFeB, Bunting-DuBois, DuBois, PA) is axially magnetized in the Z direction of the plaque with a magnetic flux density of approximately 1.4 Tesla (T). The convex magnet has a diameter of 20 mm, with a 14.55 mm inner radius of curvature, and a 15.75 mm outer radius of curvature making it only 1.2 mm thick. The N52 grade magnet is protected with a gold coating and has a maximum operating temperature of 100 °C. Plaque sterilization methods, such as gas sterilization using ethylene oxide (EO), will be necessary to avoid intrinsic damage to the magnet.

A custom COMS plaque backing was created to allow room for the magnet beneath the silastic insert. Trachsel Dental Studio (Rochester, MN) has been the sole manufacturer of COMS plaques since their origination in the 1980's. Currently, a 20 mm plaque has an inner lip height of 3.5 mm. For the custom plaque, the manufacturer extended the lip height 1.25 mm to account for the placement of the magnet. The suture eyelets were not added to the initial plaque design for ease of film measurements, but they can be added at a later time. A 20 mm plaque was chosen to evaluate effectiveness of the device for a medium tumor ($\leq$ 16 mm diameter, $\leq$ 10 mm tumor height) as COMS diameters are selected by adding a 2 mm margin to the tumor base diameter. Figure 2.1 shows the magnet (left), as well as the 20 mm plaque with the adjusted lip height. In Chapter 5 the magnet is modeled using Multiphysics Software, and the magnetic field lines are calculated (see Figure 5.1).

Figure 2.1 Custom NdFeB Magnet and 20 mm COMS Plaque with Adjusted Lip Height

2.3 Radiochromic Film Dosimetry: Materials and Methods

2.3.1 Low Energy Calibration and Scanning Parameters

Radiochromic film is energy independent at energies above 100 keV and requires a separate calibration at lower energies, including ^{125}I. A calibration curve was obtained by exposing GafChromic™ EBT3 film pieces from the same lot (#04022005) to a single IsoAid ^{125}I seed. A custom phantom was created by machining a seed slot into a 1 cm thick piece of Gammex Solid Water® High Equivalence (HE) (Sun Nuclear Corporation, Melbourne, FL). The single ^{125}I seed is therefore surrounded by Solid Water, with enough in each direction (5 cm or more) to achieve full scatter conditions. Distance was measured from the film center to the seed center. For a time-efficient calibration, two film pieces were placed above and below the source. The set up is detailed in Figure 2.2.

To obtain a calibration curve, eight dose points were collected ranging from 0 – 800 cGy. Dose from the single seed was calculated using the TG-43 updated formalism (see Equations 1.1-1.7) while accounting for decay throughout the exposure period [24,92]. Doses were second

checked with the TPS (BrachyVision, version 11.0.47, Varian Medical Systems, Palo Alto, CA). The TPS and hand-calculated doses agreed within 2%.

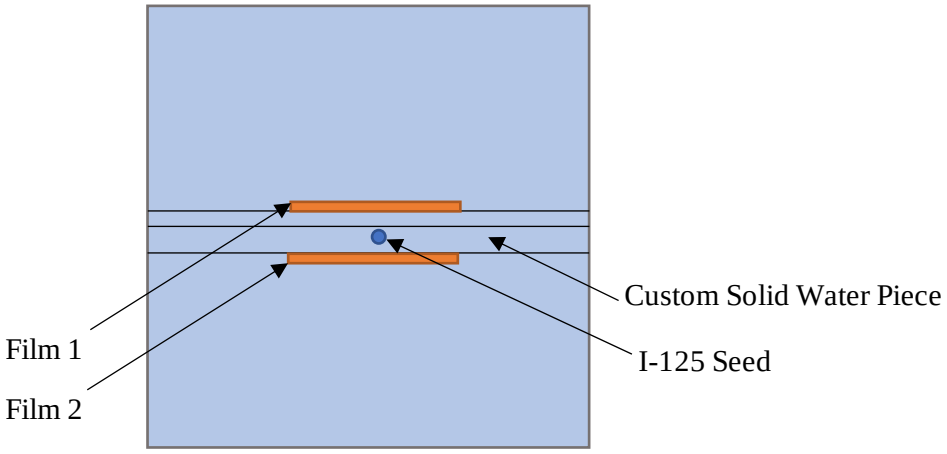

Figure 2.2 Film Calibration Setup

Film was read out using a flatbed scanner (Epson Expression 11000XL, Seiko Epson Corp., Tokyo, Japan), and associated software EPSONSCAN. The scanner ran three times to ensure warmup, and each film piece was then scanned twice to determine scanning consistency. A foam board was used as a positioning template to achieve a reproducible and flat film position. RBG-positive images were obtained with a depth of 16 bits per color channel, and a spatial resolution of 72 dpi (1 pixel = 0.353 mm). To quantify uncertainty in scanning times, one exposed film was read out three times at 24, 48, and 72 hours, and change in NOD was measured to be minimal (< 0.2 %). Therefore, film could be read anytime between 24 and 72 post-irradiations. The scanned images were saved in tag image file format (.tiff) and analyzed with ImageJ platform (National Institutes of Health, Bethesda, MD). At the area of highest dose, a 5 x 5 pixel region of interest (ROI) was used (approximately 1.5 mm x 1.5 mm). This size was chosen to improve the signal to noise ratio, while also maintaining a small region for accurate dose measured. The mean PV of the ROI was recorded for the red color channel, which was converted to OD and then NOD (see Eq. 1.10). The ROI selection is detailed in Figure 2.3.

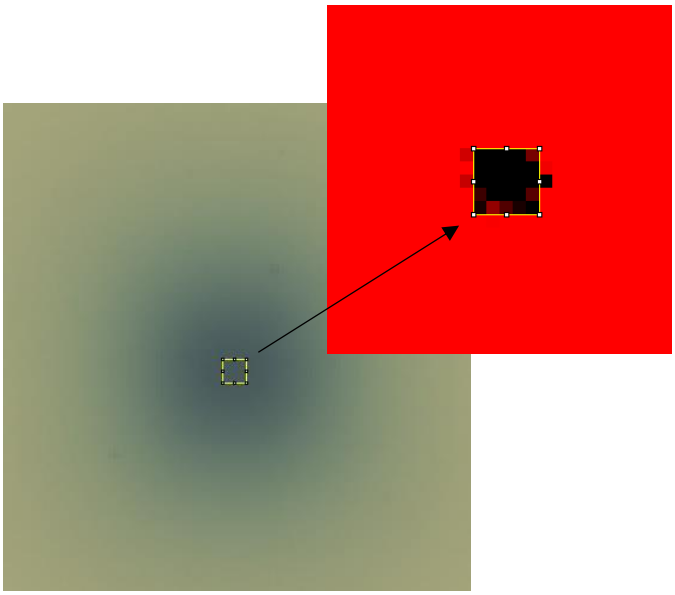

Figure 2.3 ROI Selection for Calibration Film
Left: Scanned EBT Gafchromic film.
Right: 5 x 5 pixel ROI based on maximum pixel values using red color channel.

A calibration curve was formulated using calculated dose values and measured NOD values. A curve was fit to the manufacturer recommended function (see Eq. 1.11) so that dose can be determined based on measured NOD.

2.3.2 HVL Characterization

A custom acrylic phantom was created with depth holes ranging from 0.5 – 2.0 mm so that a small amount of known fluid thickness can be quantified (See Figure 2.4). A 1 mm layer of the PDMS Fe_3O_4 was placed in the depth phantom and covered with a saran wrap layer (12.7 μm thick). The Solid Water used for film calibration was again used to hold the ^{125}I seed in a reproducible position. The seed was placed directly beneath the depth phantom with fluid, and a piece of GafChromic film was placed above to measure the attenuation (Figure 2.5). Again, Solid Water surrounded the seed and film to provide at least 5 cm of backscatter.

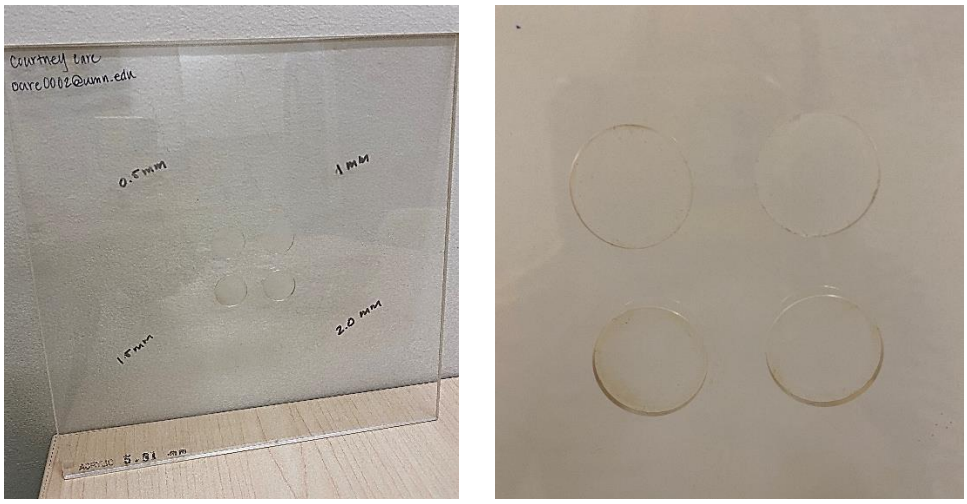

Figure 2.4 Attenuation Depth Phantom. Four depth holes were drilled into an acrylic slab with dimensions 30 cm x 30 cm x 0.581 cm. The depth holes are 0.5, 1, 1.5, and 2 mm in depth for attenuation measurements of known liquid thickness.

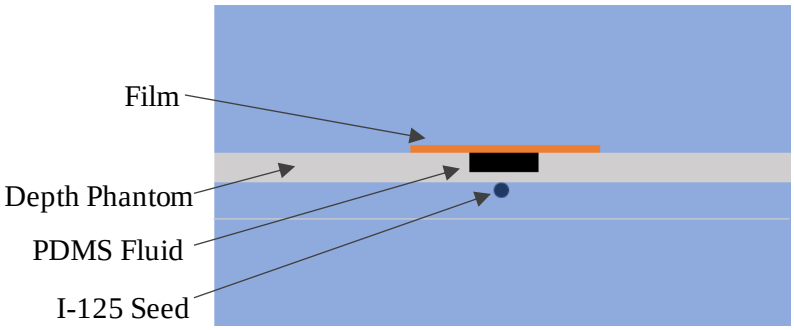

Figure 2.5 Film HVL Measurement Setup

The linear attenuation coefficient (μ) and fluid HVL was measured using the following equations:

$$\mu = -\frac{\ln\left(\frac{I}{I_0}\right)}{x} \qquad \text{Eq. 2.1}$$

$$HVL = \frac{\ln(2)}{\mu} \qquad \text{Eq. 2.2}$$

where I is the attenuated dose, I_0 is the dose without fluid, and x is the fluid thickness. I_0 was measured with the same setup, but without fluid.

2.3.3 Film-Measured PDMS Dose Reduction

Materials

To perform measurements with the fluid in place, eye phantoms were 3D printed with VeroClear (Stratasys, Eden Prairie, MN), a clear plastic that the manufacturer claims to be to polymethyl methacrylate (PMMA) equivalent. The phantoms were designed having a scleral thickness of 1 mm, with tumor base diameter of 16 mm, and various tumor heights (3-, 5- and 8-mm) (Figure 2.6). It is hypothesized that varying tumor sizes will affect the fluid distribution and resulting dose. The VeroClear composition is proprietary to the manufacturer, however an attenuation test with an ^{125}I source showed water equivalence, and the material was assumed to be water in subsequent measurements.

Figure 2.6 3D-Printed Eye Phantoms with Increasing Tumor Heights

A total of 24 seeds were calibrated for treatment using an HDR-1000 Plus vented well chamber (S/N A120136, Standard Imaging, Middleton, WI) and a MAX 4000 Plus electrometer (S/N J200787). The electrometer performed a background reading, and environmental temperature and pressure were corrected for. Additionally, a low energy pressure correction factor was applied

due to the range of electrons created by low energy photons within the size of the cavity which may otherwise cause an overresponse. Current (pA) was measured for 24 seeds to determine the source strength and comparison to the manufacturer stated source strength. The standard deviation for the 24 current measurements was 0.20 pA. The seeds were loaded into a Silastic insert. The Silastic thickness was measured (2.12 mm) and confirmed to be within the acceptable range (2.25 ± 0.5 mm) [93].

EBT3 GafChromic film (lot #: 04022005) was cut into four pieces (10.2 cm x 12.7 cm) and marked in the upper right corner to maintain orientation and direction. Film was handled with guidance in accordance with AAPM TG-55 and -235 [68,94]. While the film is water resistant, the edges did see <5 mm of water penetration throughout the 46-51 hours of exposure. Each film piece was centered to avoid water effects of damage at the ROI. A 20 x 20 x 20 cm^3 water tank was used to establish adequate scatter equilibrium around the plaque. Solid Water and a 3D-printed hold kept the plaque from rocking or moving during measurement.

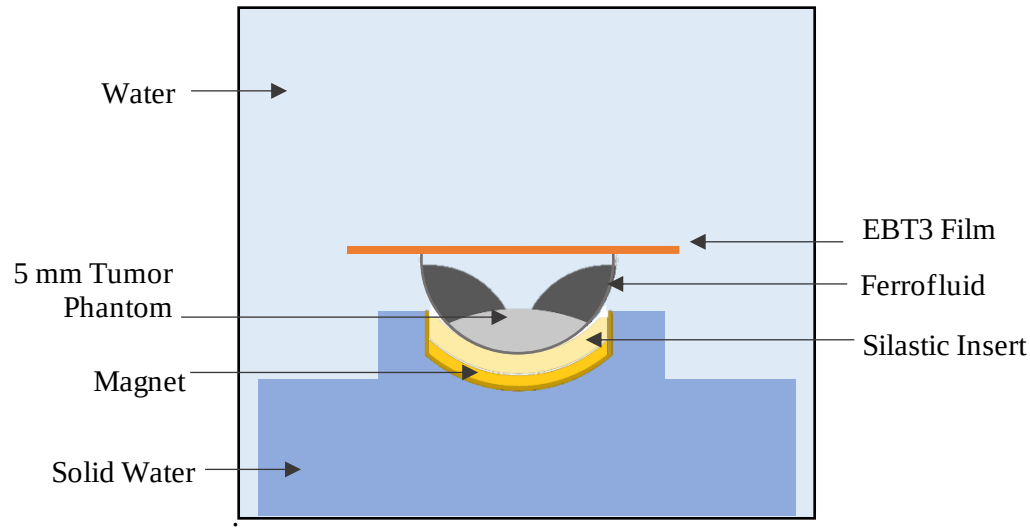

Figure 2.7 Film Water Tank Setup with the Magnetic Plaque, and 5 mm Tumor Phantom

Due to insufficient human capital and low supply of PDMS, it's use was limited to HVL measurement. This challenge was overcome in future film measurements by using a more

accessible and cost-effective ferrofluid (EFH1, Ferrotec Corporation, Tokyo, Japan). This educational EFH series ferrofluid (from here on referred to as EFH), is composed of 15% magnetite, 30% oil soluble dispersant, and 55% hydrotreated light petroleum. The magnetite proportion is less than that of PDMS, but for proof-of-concept measurements, the EFH fluid is a reasonable alternative. After evaluating its HVL, 0.8 ml of EFH was added to the 3-, 5- and 8-mm tumor phantoms. Additionally, 1.8 ml was added to the 8 mm tumor phantom to evaluate dose distribution with a larger tumor height.

2.4 Monte Carlo Transport Simulations: Materials and Methods

GAMOS version 6.1.0, a Geant4 plugin for medically oriented simulations, was used for all simulations [64–66,95,96]. A new brachytherapy source was created to simulate an IsoAid Advantage™ ^{125}I seed. The ^{125}I is evenly distributed as silver halide, in a very thin, 1 µm coating, on a silver rod with a 0.5 mm diameter, and 3 mm in length. The source is housed in a 0.5 mm thick titanium capsule, 0.8 mm in diameter, and 4.5 mm in length (see Figure 2.8). The rounded ends of the capsule are slightly larger, 0.1 mm thick [97]. The ^{125}I energy spectrum obtained from TG-43U1 recommendations, with a mean energy of 28.37 keV, displayed in Table 2.1 [24].

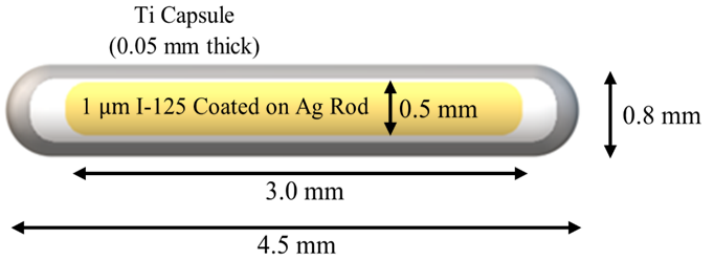

Figure 2.8 IsoAid Advantage™ ^{125}I seed. The seed is encapsulated in 4.5 mm long titanium housing, 0.5 mm thick, with larger end cap thickness. ^{125}I is coated onto a 3 mm long rod, with a 0.5 mm diameter.

Table 2.1 ^{125}I spectrum, obtained from AAPM Task Group 43 Update.

Photon energy (keV)	Photons per disintegration
27.202	0.406
27.472	0.757
30.980	0.202
31.710	0.0439
35.492	0.0668
Weighted Mean: 28.37 keV	Total: 1.476

An important step in MC dosimetry is the determination of an energy cutoff value. The cutoff value prevents the tracking of large quantities of low energy particles and save long computing time. An energy cutoff discontinues particle production beyond the energy level, but deposits dose or energy in the voxel or volume of interest. For brachytherapy sources, a small cutoff value is encouraged, typically 5 keV [24]. GAMOS utilizes range cuts, the default value being 0.1 mm for all processes. With our low energy ^{125}I source and phantom geometries are much smaller in brachytherapy simulations and dosimetry, the range cut use for all simulations in this work is 0.0001 mm.

2.4.1 Benchmarking an ^{125}I Source

Prior to using a new MC geometry for a brachytherapy seed, the source should be benchmarked with consensus data and experimental measurement. TG-43 parameters including dose rate constant, radial dose, and anisotropy function were checked for reproducibility with consensus data and similar source assessment studies.

Dose Rate Constant

Air kerma strength was evaluated by placing the ^{125}I seed at the center of the geometry, consisting of dry air at sea level (0.01% C, 75.53% N, 23.18% O, 1.28% F by weight). The geometry used to measure air kerma similar to the NIST wide angle free air chamber (WAFAC)

which extends from 82.5° – 97.5° (90°±7.5°)[98]. This section of a sphere was placed 40 cm from the seed center by (inner radius = 39.5 cm, outer radius = 40.5, thickness 1 mm) to score air kerma with the GmG4PSKerma GEANT4 scorer. The obtained air kerma was corrected by inverse square of the distance, d, and the attenuation of air to simulate the events *in vacuo* as recommend by TG-43. In addition, the air attenuation correction factor is utilized and air kerma strength was calculated.

$$S_k = K(d) * (d^2) * e^{\mu d} \qquad \text{Eq. 2.3}$$

where μ is the linear attenuation coefficient of air at standard temperature and pressure for 30 keV.

The dose rate at 1 cm, 90°, is evaluated by placing the source in a geometry consisting of water and Solid Water. A 0.1x0.1x0.1 mm^3 water voxel is used to score dose with the GEANT4 GmG4PSDoseDeposit. Dose rate constant was evaluated by dividing the measured 1 cm dose rate in water by the air kerma strength. 1 x 10^9 events (or histories) were performed to achieve $1\sigma < 1\%$ as recommended by AAPM TG-43U1. Water and Solid Water dose rate constants were both calculated.

Radial Dose Function

The seed was placed at the center of a water geometry (40x40x40 cm^3). Rings were placed radially around the source at 90° to achieve better statistics. The GmG4PSDoseDeposit scorer was used in each ring, extending from 0.5 to 10 cm. The ring thickness increased with increasing distance. As recommended by Taylor et al., for $r \leq 1$ cm, a 0.1 mm, $1 < r \leq 5$ cm, 0.5 mm, and $r >$ 5 cm, 1 mm ring thicknesses were used [99]. The world and voxel geometries are composed of water or Solid Water.

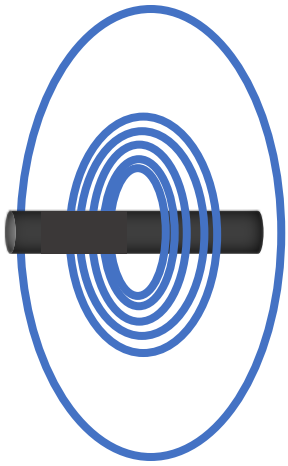

Figure 2.9 Radial Dose MC Geometry. Concentric rings extend from 0.5 to 10 cm at 90° from the source axis.

Anisotropy Function

The anisotropy function is evaluated to ensure encapsulation accuracy of the new source at surrounding angles and distances. To evaluate in MC, rings were placed at radial distances (0.5, 1, 2, 3, 5, and 7 cm) and angles (0, 10, 20, 30, 40, 50, 60, 70, 80, and 90°). Due to symmetry of the IsoAid source, rings can be utilized to increase the scoring volume with no change in distance, thus reducing statistical error. Figure 2.10 demonstrates the ring geometry used for 40° anisotropy measurements at ranging distance from the source center.

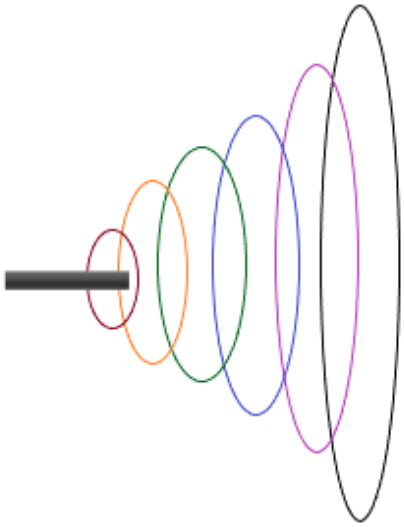

Figure 2.10 Anisotropy MC Geometry. Each ring is placed at an angle 40° relative to the source axis and placed at increasing distances from the source center.

2.4.2 Benchmarking a COMS Plaque

A 20 mm plaque was used for film measurements and was simulated in MC for comparable studies. The plaque geometry was based on the description in AAPM Task Group 129 [5]. The simulated plaque backing was composed of gold Modulay that had a 15.05 mm outer radius of curvature, was 0.5 mm thick, and had a lip height of 2.75 mm. The Silastic insert had a 14.55 mm outer radius of curvature and a 12.3 mm inner radius of curvature (with a default thickness of 2.25 mm). The Silastic is 20 mm in diameter. Most importantly, the benchmarked ^{125}I seeds were placed within the Silastic at locations and angles according to the seed center coordinates and angles described in Table 1 of Task Group 129 for a 20 mm plaque. The simulated center of the MC geometry is the inner sclera to align with standard COMS dosimetry and the treatment planning system.

NIST elements, densities, and material compositions were used for components in the GAMOS geometry. Solid Water, Modulay, and Silastic were user-defined materials in GAMOS. Solid Water a density of 1.03 g/cm^3 (8.13% H, 19.37% O, 65.80% C, 2.21% N, 0.14% Cl, 1.78% Ca, 0.20%

Na, 1.11% Mg, 1.14% Si), in line with the composition from the manufacturer of Solid Water used in film measurements. The mass composition of Modulay (ρ = 15.8 g/cm^3) is 77% Au, 14% Ag, 8% Cu, and 1% Pd. The Silastic is a medical grade elastomer MDX4-4210 (Dow Corning Crop., Midland, MI) with a mass composition of 39.9% Si, 28.9% O, 24.9% C, 6.3% H, and 0.005% Pt [5]. The Silastic has a density of 1.12 g/cm^3, and an effective Z (Z_{eff}) of 11. For comparison, the density of water is 1.0 g/cm^3 and Z_{eff} of 7.4. EFH and PDMS fluid compositions are described in Table 2.2.

Table 2.2 PDMS and EFH Ferrofluid Composition

	PDMS	EFH
Element	Mass Fraction	
Fe	0.5065	0.1085
O	0.2634	0.4309
C	0.1124	0.0900
H	0.0226	0.0400
Si	0.0650	
S	0.0600	0.0593
N		0.1569
P		0.1147
Density	2.232 g/cm^3	1.421 g/cm^3

As described in Section 2.1.1 the treatment planning procedure for COMS plaques is based on tumor dimensions and OAR distances measured with fundus photography and ultrasound, performed by the ophthalmologist. The tumor base diameter and OAR distances from the tumor margin are determined using the plaque coordinate system proposed by Kline at al. [90]. For MC simulations OAR coordinates are defined using this plaque coordinate system, in which the sclera is the origin. One patient's coordinates were used to benchmark the 20 mm MC plaque with the treatment planning system (Table 2.3).

Table 2.3 Plaque Coordinates used for MC and TPS Calculations

Structure	X	Y	Z
Tumor Apex (5 mm)	5	0	0
Eye Center	11.3	0	0
Lens	11.3	7.7	0
Macula	11.3	11.3	0
Optic Disc	8.3	10.6	0
Inner Sclera	0	0	0

Dose was scored at each structure location by converting the output, dose per event (Gy) to dose based on the number events calculated with the exposure time, number of sources, and the source strength (1 Bq = 1 event/second). A small (0.1 mm x 0.1 mm x 0.1 mm) dose scoring box was placed at the location of the tumor apex, eye center, and inner sclera. A ring geometry was used for the lens, macula, and optic disc to increase dose scoring efficiency at the specified distance, assuming a symmetric dose.

For comparison to TG-43, TG-129 and treatment planning systems, the 20 mm plaque was benchmarked with the treatment planning system as well as TG-43 hand calculations. Dose from a heterogeneous plaque (silastic and backing) was calculated in addition to a water-only geometry. Finally, the homo/heterogeneous dose ratio was compared to values given in TG-129.

2.4.3 HVL Characterization

The ferrofluid was characterized by measuring attenuation properties in the presence of ^{125}I photons. MC simulations and Gafchromic film are both utilized for measurements and are compared. Additionally, the attenuation can be hand-calculated based on the elemental composition. The attenuation coefficient of the mixture can be calculated using Equation 2.4, based on the weight (w) of each element, and known attenuation coefficients of elements (i). This section will address the MC and hand-calculated attenuation properties of ferrofluid.

$$\frac{\mu}{\rho} = \sum_i w_i \frac{\mu}{\rho_i} \qquad \text{Eq. 2.4}$$

The analyzed ferrofluid (Fe_3O_4-PDMS) is composed of 30% magnetite, 70% silicone-based polymer, PDMS provides stability and prevents coagulation of magnetite particles. To characterize a material in MC, the density and composition by weight are inputted (see Table 2.2).

The MC geometry was created to mimic the HVL measurements performed with film. A single IsoAid ^{125}I seed was placed 5.81 mm from a voxelized detector to score dose. Two simulations were run: one with a 1 mm layer of fluid adjected to the detector, and one simulation without. See Figure 2.11 for the MC attenuation set up geometry. Two simulations calculated dose with and without a 1 mm layer of PDMS. A planar array of scoring voxels (1 mm^3) was used with 10^9 events to achieve statistical uncertainties $1\sigma \leq 0.2\%$.

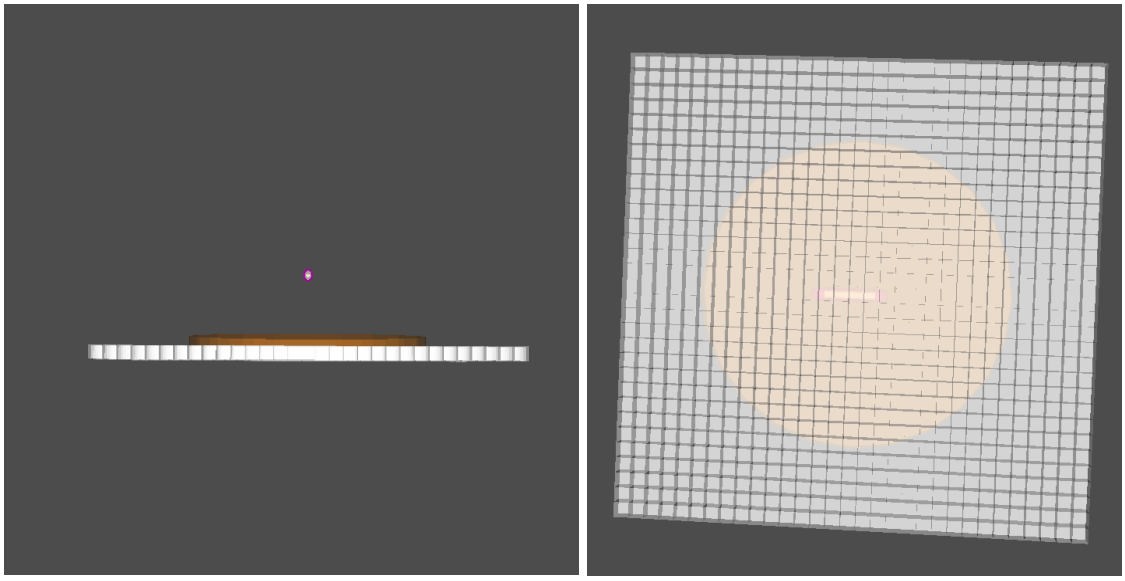

Figure 2.11 Attenuation MC Geometry. *Left:* The seed is placed 5.81 mm from the voxelized dose scoring phantom to mimic the film measurement geometry with a 1 mm fluid layer. *Right:* A planar array of voxels, 31 x 31 x 1 mm^3 for dose scoring.

2.4.4 MC-Calculated PDMS Dose Reduction

MC simulations were used to measure dose distribution throughout the eye with the intraocular shield. First, film measurements were validated by simulating the geometry in GAMOS.

EFH fluid was distributed around 3-, 5-, and 8-mm tumor heights. The fluid distribution around the tumor and magnet is complex and to help model it, measurements were taken using megavoltage computed tomography (MVCT) images from a Radixact® system (Accuray, Sunnyvale, CA). The images were analyzed, and structures (ferrofluid, tumor, magnet, plaque, silastic, etc.) were segmented in Velocity (Version 4.1, Varian Medical Systems, Palo Alto, CA). See Figure 2.12 for MVCT images to segment the plaque and fluid structures in Velocity. The ferrofluid structure size measurements in Velocity encouraged an accurate MC model and fluid geometry.

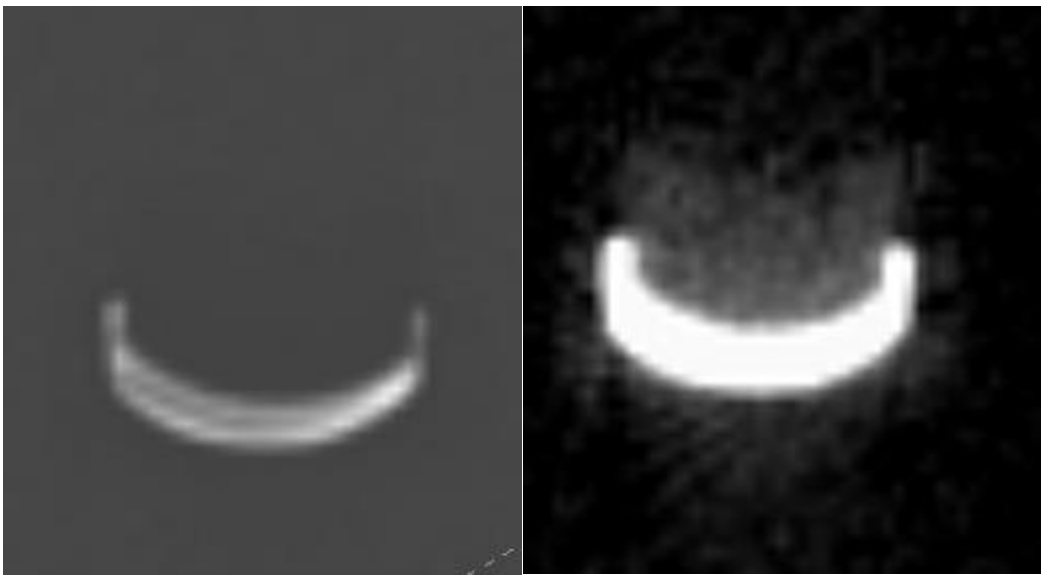

Figure 2.12 MVCT Images of 20 mm Plaque + Magnet (Left) and Ferrofluid (Right).

Dose was scored horizontally, or parallel to the plaque, to mimic film geometry. At 11.3 mm from the source, 1x1x1 mm^3 voxels filled a 1x31x31 mm^3 water phantom, which scored dose using the GmG4PSDoseDeposit GEANT4 dose-scoring tool. Given the exposure time and source strength used for film measurements, dose per event was converted to dose in each voxel. These horizontal EFH measurements were compared to film EFH measurements, and then repeated using PDMS.

In addition to horizontal measurements, vertical dose distribution was measured perpendicular to the plaque. 0.5x0.5x0.5 mm^3 voxels were utilized (voxels were in close proximity

to the sources). Dose per event results were converted to dose based on the exposure time and source strength to achieve the nominal homogenous dose of 8500 cGy to 5 mm or the tumor apex, whichever is greater, based on ABS COMS recommendations [23]. Vertical dose was measured for 0.8 ml PDMS and EFH for all three tumor heights. Additionally, 1.8 ml of each ferrofluid was measured for the 8mm tumor height.

Lastly, to align with the treatment planning procedures performed at our institution, dose reduction by PDMS was summarized for increasing distance from the tumor margin along the sclera. PDMS dose reduction was calculated for increasing structure to tumor margin (ST) using dose scored to water in 1 mm thick rings, increasing along the edge of the eye. This result will have the most clinical implication to the current treatment planning process.

2.5 Multiphysics Simulations: Materials and Methods

COMSOL version 6.0.0 was used to perform time dependent simulations utilizing the Magnetic Fields – No Currents, Laminar Flow, and Level Set physics interfaces. A geometry was created to mimic an eye (11.3 mm inner diameter), a tumor (3-, 5-, or 8-mm height), a concave NdFeB magnet (inner radius of curvature = 14.55 mm, outer radius of curvature = 15.77 mm, diameter = 20 mm), and needle (diameter = 1 mm) for fluid (PDMS) injection. Important materials and parameters were defined in the simulation (Table 5.1) that were required for magnetic fields or laminar flow.

Table 2.4 COMSOL Material Parameters

Parameter	N52 (Sintered NdFeB)	PDMS-Fe3O4	Water
Density (g/cc)	2.320	2.32	1000
Dynamic Viscosity (Pa-s)	-	10	0.001
Relative Permeability	1.05	1.05	0.999
Remanent Flux Density (T)	1.44	-	-

The magnetic field lines and Gauss lines are modeled to evaluate how the fluid is expected to interact with the magnet, but also how to provide safety information to patients for the duration of the implant. The magnetic field falls off with the inverse square ($1/r^2$) of the distance. The earth's magnetic field is approximately 0.5 G (0.05 mT) [100]. Ideally patients should keep distances greater than the 0.5 Gauss. In MRI safety, 5 G is the standard distance at which ferromagnetic objects should not approach the bore. Gauss lines ranging from 50 to 0.5 G are studied to anticipate what distances patients should keep from ferromagnetic materials and objects during the procedure, but also at home.

Lastly, fluid is modeled in three tumor sizes using the laminar flow interface. The needle releases fluid at a rate of 1.6e-7 m^3/s for 5 seconds, distributing a total of 0.8 ml of fluid. This amount was increased to 1.8 ml for the 8 mm tumor. The time dependent study was performed until fluid settled at the tumor (<10 seconds).

CHAPTER 3: RETROSPECTIVE STUDY RESULTS

3.1 Demographics and Outcomes.

Of the 52 patients with adequate follow-up data the median follow-up time was 3.6 (range 0.5 – 13.5) years, the median age was 67 (range 24 – 91) years, and median BMI was 29 (range 19 – 49). Table 3.1 summarizes demographics and preexisting conditions for the studied patients.

Table 3.1 Patient Demographics (n = 52)

Follow-up Time (Years)	Median	3.6
	Range	0.5 – 13.5
Age (Years)	Median	67
	Range	24 - 91
BMI	Median	29
	Range	18.6 – 48.9
Sex	M	28 (54%)
	F	24 (46%)
Smoking Status	Former	28 (52%)
	Current	5 (9%)
	Non-Smoker	23 (39%)
Laterality	Left	28 (52%)
	Right	26 (48%)
Plaque Diameter (mm)	12	2 (4%)
	14	5 (10%)
	16	17 (33%)
	18	18 (35%)
	20	7 (16%)
	22	3 (6%)

Pre-existing eye conditions (treated eye)	
Vitreal or Retinal Detachment	14 (27%)
Glaucoma	7 (13%)
Macular Degeneration	6 (11%)
Cataract	4 (8%)

Table 3.2 presents the dosimetry data obtained from treatment planning records of the 52 patients, as well as distance of the macula, optic disc, and lens from the inner sclera reference point. Tumor heights ranged from 1.23 to 10 mm. The median optic disc and macula doses were about 42

and 52 Gy, respectively. Maximum doses to the optic disc and macula were much higher, 114 and 218 Gy.

Table 3.2 Dosimetry and Distance – Descriptive Statistics of the Sample

Dosimetry	Median (Gy)	Min Dose (Gy)	Max Dose (Gy)
Tumor Apex	97.3	18.5	174.8
Inner Sclera	252.2	134.0	568.4
Opposite Retina	7.5	3.2	19.5
Macula	52.1	8.6	218.0
Optic Disc	41.5	10.2	114.4
Lens Center	16.0	4.9	59.1
Distance	Median (mm)	Min (mm)	Max (mm)
Macula Distance	10.6	3.0	19.5
Optic Disc Distance	11.0	4.8	21.6
Lens Distance	16.3	9.2	18.3

Incidence rates of outcomes in the studied patient population are shown in Table 3.3. 85% demonstrated mild VA decline, 40% experienced moderate VA decline, and 38% developed blindness after treatment. Over half of patients (65%) experienced RR, and 65% developed cataracts in the treated eye.

Table 3.3 Observed Outcomes

Side Effect	Frequency *n* (%)
Mild VA Decline (1 - 5 Snellen Lines)	44 (85%)
Moderate VA Decline (≥5 Snellen Lines)	21 (40%)
Blind (20/200 or worse)	20 (38%)
Radiation Retinopathy	34 (65%)
Cataract	29 (65%)
Lens replacement	7 *Excluded*
Vitreous Detachment	6 (12%)
Glaucoma	4 (8%)

One of the most important outcomes to follow for patients was VA changes over time (Figure 3.1). There is a clear positive trend as time elapsed increases, however the R^2 value (0.26) is low due to wide variation in data. The proportion of patients not RR or VA decline are shown with cumulative incidence curves in Figure 3.2.

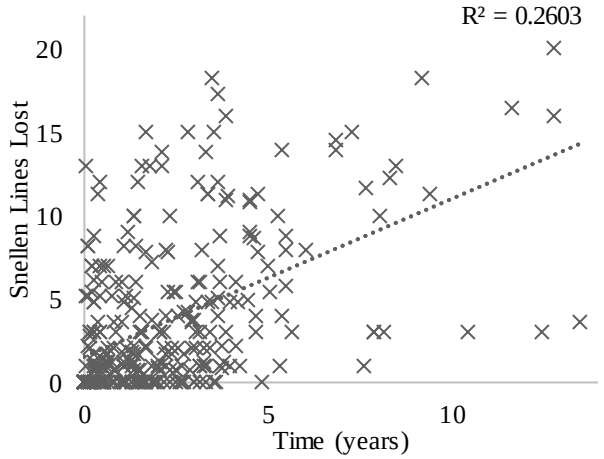

Figure 3.1 VA Decline overtime.

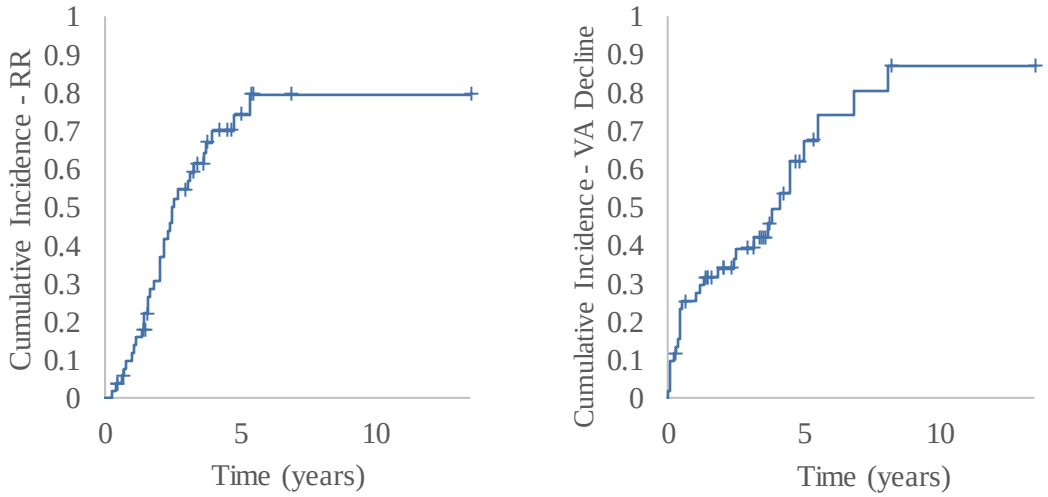

Figure 3.2 Cumulative Incidence Plots for Radiation Retinopathy (left) and VA (right), depicting proportion of patients' overtime.

3.2 Statistics

Based on the univariate analysis, age, dose, and distance to the macula and optic disc are significantly related to incidence of RR. Dose to the optic disc corresponds to moderate vision decline, and lens dose is related to the development of cataract formation. Outcomes from the univariate analysis are shown in Table 3.4. Many variables had significance removed based on sensitivity tests with confounding variables including glaucoma, macular degeneration, and existing cataracts.

A RR analysis was performed with 95% confidence interval estimates (Table 3.5). The median doses to macula and optic disc were 52 and 42 Gy which are used to define high and low dose groups. The median dose to the lens was 16 Gy. Dose to the optic disc (D_{OD}) >42 Gy and dose to the macula (D_{Macula}) > 52 Gy had significant RR for both radiation retinopathy, moderate VA decline, and onset of blindness. Dose to the lens (D_{Lens}) >16 Gy posed a RR for cataracts. Several variables lost significance due to confounding preexisting conditions.

Kaplan-Meier cumulative incidence curves showed a significant relationship between radiation retinopathy and D_{Macula} > 52 Gy and D_{OD} >42 Gy. For retinopathy, a significant hazard ratio was found for D_{Macula} > 52 Gy and D_{OD} >42 Gy (2.40 and 2.03, respectively). Lastly, D_{Lens} > 16 Gy had a significant log rank test as well as a significant hazard ratio (2.59). These results, in addition to insignificant findings for moderate VA decline are shown in Figures 3.3 A-E. Onset of blindness was also evaluated but had an insignificant hazard ratio and log rank test.

A logistic regression was performed for each dose-toxicity relationship that had a significant univariate analysis. The predicted probability of radiation retinopathy is seen to incease with macula dose (Figure 3.4). Similar results are seen for optic disc dose – retinopathy and lens dose – cataract formation. This information as well as the data provided in the relative risk and

Kaplan-Meier analyses can be helpful guidance to determine the likelihood that a patient may experience unwanted side effects after treatment.

Table 3.4 Univariate Analysis Results:
Significant ($p \leq 0.05$) relationships between demographics, dose, and distance with toxicities.

Toxicity:	Variable:	P:	Mean with Toxicity	Mean without Toxicity
Radiation Retinopathy	***Optic Disc Dose (Gy)**	**0.03**	55.5	35.6
	***Optic Disc Distance (mm)**	**0.03**	11.1	13.6
	***Macula Dose (Gy)**	**0.001**	87.6	39.7
	***Macula Distance (mm)**	**0.01**	9.8	12.7
	Tumor Height (mm)	0.41	4.24	4.41
	Plaque Diameter (mm)	0.06	17.6	16.6
	***Age**	**0.04**	67.9	61.3
	BMI	0.30	30.6	29.4
Moderate VA Decline	***Optic Disc Dose (Gy)**	**0.01**	59.0	41.6
	[a b] Optic Disc Distance (mm)	0.04	10.9	12.7
	[a c] Macula Dose (Gy)	0.02	89.6	58.4
	[a] Macula Distance (mm)	0.01	9.33	11.7
	Tumor Height (mm)	0.31	4.33	4.04
	Plaque Diameter (mm)	0.14	17.5	16.8
	Age	0.09	65.9	60.1
	BMI	0.36	30.2	29.5
Blind	[a b] Optic Disc Dose (Gy)	0.04	61.6	45.1
	[a b c] Optic Disc Distance (mm)	0.04	10.5	12.7
	[a b] Macula Dose (Gy)	0.05	95.2	64.4
	Macula Distance (mm)	0.11	9.42	11.1
	Tumor Height (mm)	0.09	4.43	3.96
	Plaque Diameter (mm)	0.11	17.5	16.5
	Age	0.22	64.9	61.4
	BMI	0.42	30.1	29.6
Cataract	***Lens Dose (Gy)**	**0.003**	19.9	13.6
	Lens Distance (mm)	0.07	15.9	16.6
	Tumor Height	0.06	4.49	3.51
	Plaque Diameter	0.38	17.3	17.1
	Age	0.95	62.9	58.6
	BMI	0.27	29.8	28.8

*Indicates significance ($P \leq 0.05$) without confounding variables

[a] Preexisting glaucoma removes significance

[b] Preexisting macular degeneration removes significance

[c] Preexisting retinal detachment removes significance

Table 3.5 Relative Risk Analysis Results

Toxicity	Characteristic	RR	95% CI
Radiation Retinopathy	***Dose to Optic Disc >42 Gy**	**1.68**	(1.34 – 2.11)
	[a,b]Proximity to Optic Disc <10 mm	1.32	(1.01 – 1.73)
	***Dose to Macula >52 Gy**	**1.74**	(1.41 – 2.15)
	[b]Proximity to Macula <10 mm	1.67	(1.34 – 2.07)
	Age >65	0.89	(0.66 – 1.21)
	***Sex (M)**	**1.38**	(1.08 – 1.78)
	BMI >30	1.24	(0.96 – 1.61)
	Smoking History	1.00	(0.72 – 1.37)
Moderate VA Decline (> 5 Snellen Lines)	***Dose to Optic Disc > 42 Gy**	**2.50**	(1.58 – 3.95)
	[b]Proximity to Optic Disc <10 mm	2.08	(1.34 – 3.22)
	***Dose to Macula > 52 Gy**	**2.34**	(1.41 – 3.88)
	Proximity to Macula <10 mm	1.07	(0.60 – 1.90)
	Age >65	0.72	(0.42 – 1.25)
	Sex (M)	1.00	(0.42 – 2.39)
	***BMI > 30**	**1.94**	(1.16 – 3.23)
	Smoking History	0.88	(0.50 – 1.55)
Blind	***Dose to Optic Disc > 42 Gy**	**3.73**	(1.30 – 4.35)
	[c]Proximity to Optic Disc <10 mm	1.89	(1.16 – 3.06)
	***Dose to Macula > 52 Gy**	**2.03**	(1.21 – 3.40)
	[c]Proximity to Macula <10 mm	2.17	(1.35 – 3.48)
	Age >65	0.65	(0.36 – 1.17)
	***Sex (M)**	**2.00**	(1.22 – 3.28)
	BMI >30	1.06	(0.53 – 2.11)
	Smoking History	1.52	(0.92 – 2.53)
Cataract	***Lens Dose >16 Gy**	**1.71**	(1.34 – 2.18)
	Proximity to Lens <15 mm	1.30	(0.94 – 1.78)
	Age >65	1.20	(0.90 – 1.60)
	Sex (M)	1.20	(0.90 – 1.60)
	BMI >30	1.33	(0.92 – 1.91)
	Smoking History	0.78	(0.45 – 1.36)

***** Indicates significance ($P \leq 0.05$) without confounding variables

[a] Preexisting glaucoma removes significance

[b] Preexisting macular degeneration removes significance

[c] Preexisting retinal detachment removes significance

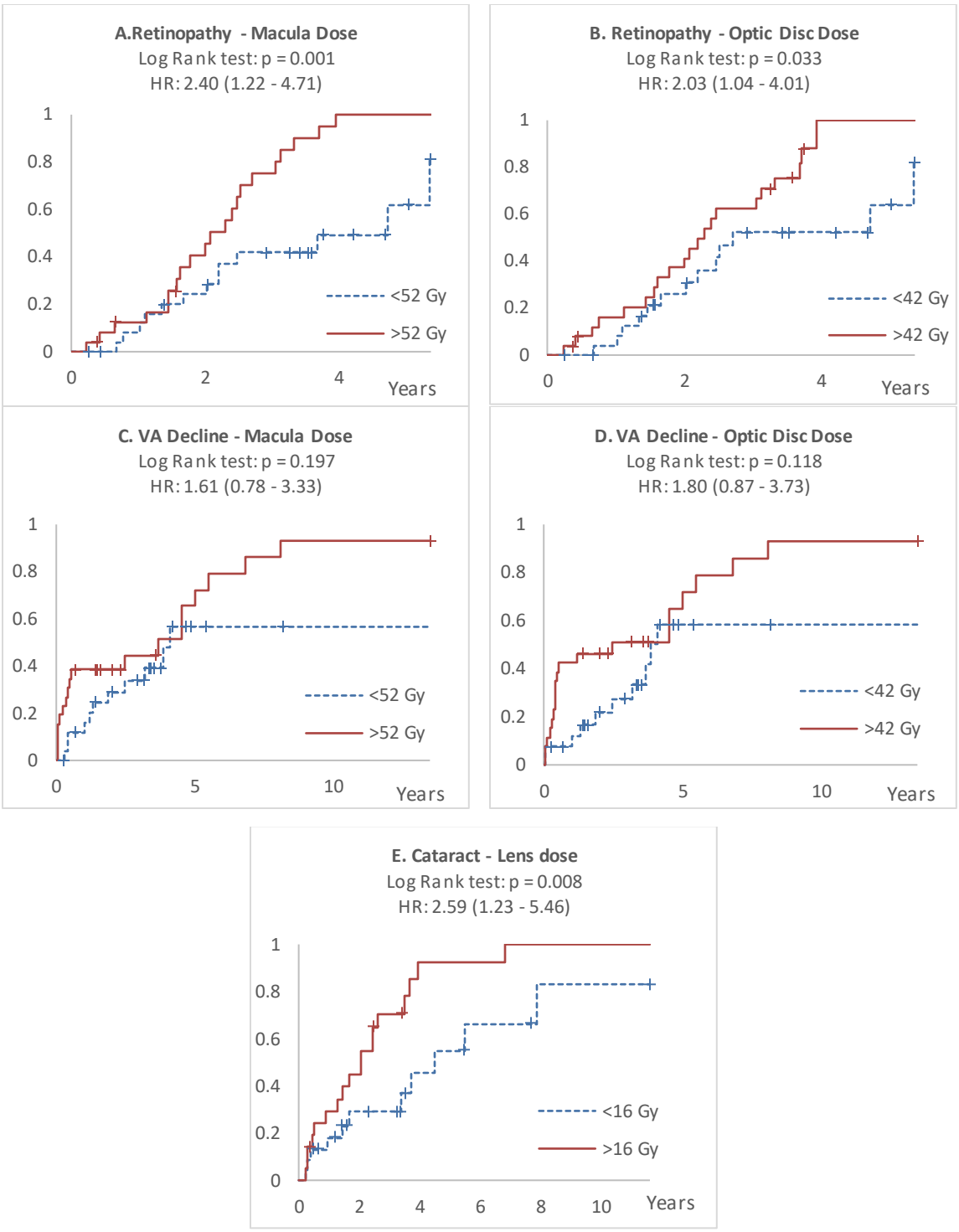

Figure 3.3 A-E High- vs. Low- Dose Cumulative Incidence curves are shown for two dose groups and resulting toxicities. Log Rank and hazard ratios are displayed for each. *A and B:* Radiation retinopathy is shown for two groups, one receiving a high D_{Macula} (>52 Gy). A similar curve is displayed for D_{OD} (>42 Gy). *C - D* Moderate VA decline curves are displayed for D_{Macula} and D_{OD}. *E:* Cataract toxicity is compared overtime for groups with D_{Lens} > 16 Gy.

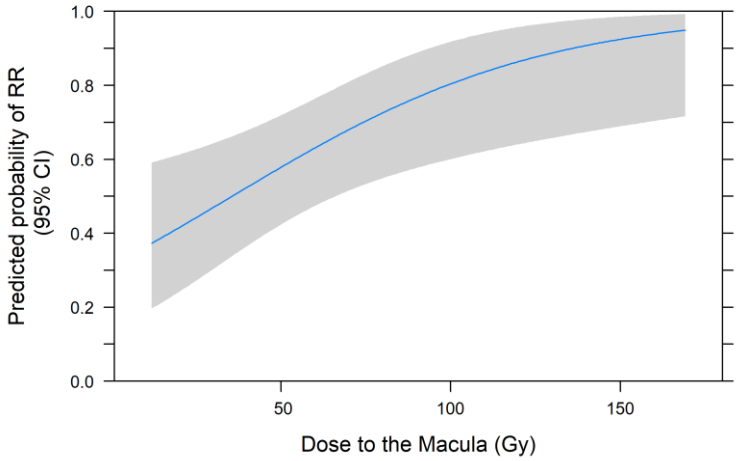

Figure 3.4 Logistic regression: macula dose and radiation retinopathy with 95% CI

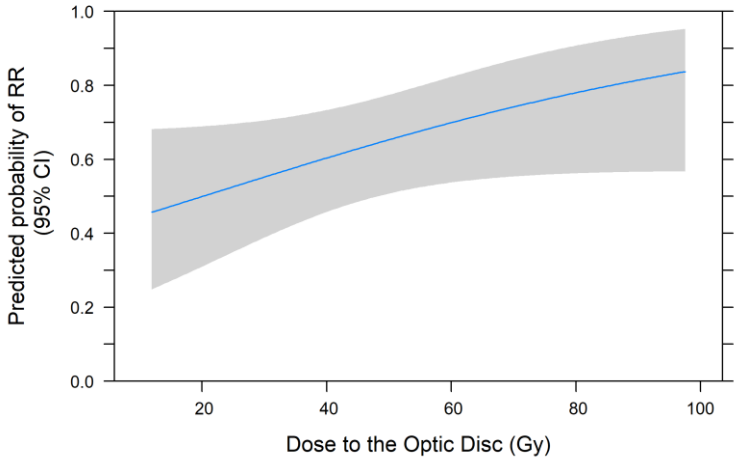

Figure 3.5 Logistic regression: optic disc dose and radiation retinopathy with 95% CI

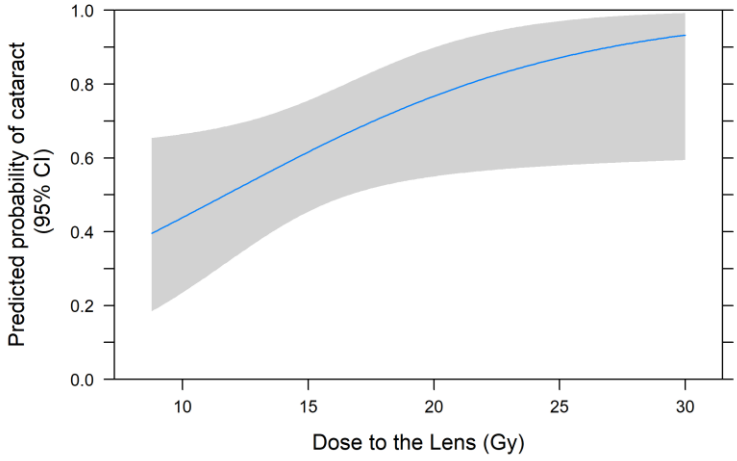

Figure 3.6 Logistic regression: lens dose and cataract with 95% CI

3.3 Discussion

The results from both the demographic data and the statistical analyses align with previous literature [32,33,101,102]. The evaluated doses (D_{Macula} >52, D_{OD} >42 Gy) were very similar to findings by Gunduz et al. who reported high retinopathy rates at D_{Macula} > 57 Gy, D_{OD} >44 [101]. Their conclusion is strengthened by this work. The incidence rate of retinopathy (65%) falls within the wide range of previous literature in addition to rates of moderate VA decline (40%) and cataract formation (65%) [21,23,32,33,37,39,43,103].

The univariate and relative risk sensitivity tests performed suggest that radiation retinopathy may be predicted by D_{Macula} and D_{OD}, and VA decline may be predicted by D_{OD}. Moreover, the analyses indicate the cataracts may be predicted by D_{Lens}. The Kaplan-Meier incidence plots indicate that a cumulative proportion of patients experience toxicity over time. Additionally, D_{Macula} > 52 Gy and D_{OD} > 42 present a significant hazard ratio for radiation retinopathy, and D_{Lens} > 16 Gy presents a significant hazard ratio for cataracts.

Regarding dose reduction, at least half of patients studied would benefit from reduced macula dose and optic disc dose. Table 3.6 shows how the percentage of patients with high dose levels (D_{Macula} >52, D_{OD} >42, D_{Lens} >16) would change with additional HVLs, or reducing the dose in half. One HVL would reduce the percentage of high dose patients to 21% or less, and two HVLs would reduce the number of high dose patients to nearly zero. This important finding indicates that 2 HVLs of shielding would adequately improve quality of life for many patients undergoing eye plaque therapy.

Table 3.6 HVL's required to reduce dose adequately

	% Of Patients remaining with High Dose		
	Current (%)	1 HVL (%)	2 HVLs (%)
Macula Dose > 52 Gy	50	21	2
Optic Disc Dose > 42 Gy	50	15	0
Lens Dose > 16 Gy	50	12	0

Limitations

This study comes with many limitations, the main disadvantage being the small size of the patient population and the lack of long-term follow-up. False negatives likely exist for retinopathy and VA decline due to short follow-up duration for some patients, as these toxicities can take years to develop post treatment. While confounding variables were accounted for in univariate and relative risk analyses, studied outcomes such as cataracts or retinopathy may impact vision decline. Additionally, side effect reduction strategies including anti-VEGF therapy for macular edema or laser therapy for neovascularization were not accounted for. The study was performed believing patients received the standard of care for their side effects. Future studies (or a prospective trail) should be completed with a larger sample size with adequate long-term follow-up to represent the patient population.

In this work homogenous dose point calculations were solely used based on the institutional treatment planning process. AAPM TG-129 recommends using both homogenous and heterogeneous dose calculations to account for the gold-alloy backing and Silastic seed carrier, however a commercial heterogenous TPS is not available. Correction factors from TG-129 (and additional literature) can be utilized for heterogenous dose calculation, however these correction factors are only published for the central axis dose points [5,22]. While AAPM recommends using homogenous and heterogeneous dose calculations, the results presented follow the current clinical practice at this institution.

CHAPTER 4: RADIOCHROMIC FILM DOSIMETRY AND MC SIMULATION RESULTS

4.1 Film Calibration

Upon analyzing film exposed to eight dose points, the curve fitting tool in MATLAB was used to determine values of a, b, and c to form a useful calibration curve. The film-measured dose points matched the calculated dose points within 3%. The manufacturer recommended fit is used (Dose = a + b/(NOD – c), where a =-589.1, b = -459.7, and c=0.7814). The R^2 = 1.00 and the adjusted-R^2 = 0.9999.

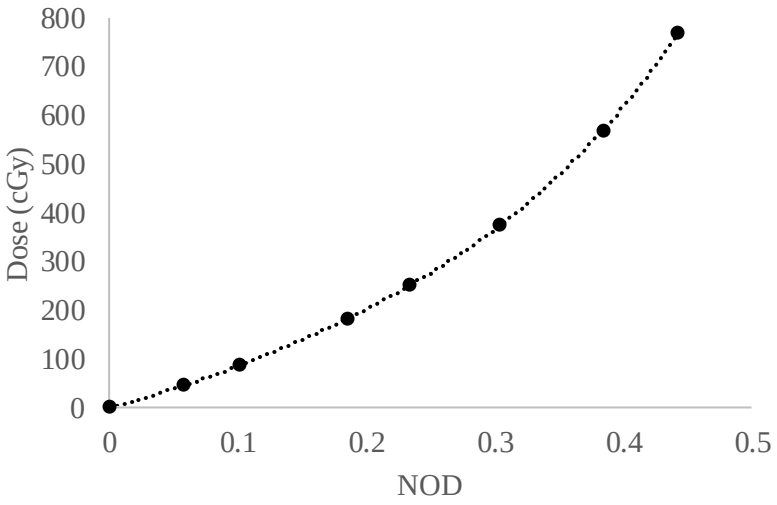

Figure 4.1 EBT3 GafChromic™ Film Calibration Curve for ^{125}I

4.2 MC Benchmarking

4.2.1 IsoAid Advantage ^{125}I Source

Air Kerma Strength and Dose Rate Constant

The MC-measured dose rate constant in this work was calculated to be $\Lambda = 0.995 \pm 0.002$ cGy/h/U for liquid water and 1.049 ± 0.002 cGy/h/U for Solid Water. In comparison, the TG-43 consensus value is 0.981 cGy/h/U for IsoAid ^{125}I sources [104]. This consensus value is based on previous MC-calculated dose rate constants, $\Lambda = 0.980 \pm 0.03$ and 0.962 ± 0.005, using PTRAN and MCNP4C codes [97,105]. Recent ^{125}I studies have calculated dose rate constants to be 1.038, and $1.118 \pm 0.5\%$ cGy/h/U for other manufacturers using GEANT4-GATE and MCNP5 [106,107]. It should be noted that Zaker et al. discovered MCNP4C2 uses a cross section library giving erroneous dose rate constant and radial dose measurements for low energy gammas. Interestingly, Solberg et al. used MCNP4C code, which many TG-43 consensus data rely on. For this reason, the work of Meigooni and Zaker are considered best benchmarks for the IsoAid source modeled in this work (Oare).

Table 4.1 Dose Rate Constant Comparison

Reference	Method	Λ (cGy/h/U)	Error
Oare	G4-GAMOS	0.995	± 0.002
Solberg et al.	MCNP4C	0.962	± 0.005
Meigooni et al.	PTRAN	0.980	± 0.03
Meigooni et al.	TLD (SW)	1.020	± 0.08
Zaker et al.	MCNP5	1.119	±0.006
TG-43U1S1	Various	0.981	

Radial Dose Function

The radial dose function from a line source $g_L(r)$ measured in water and Solid Water compared well to previous MC calculated functions [97,105,107]. The average ratio of this work

compared to Meigooni et al. was 0.98, TG-43/Solberg et al. was 0.94, and Zaker et al. was 1.00. The radial dose calculated in this work falls within the uncertainty range of consensus data and previous reports (Figure 4.2 and Table 4.2).

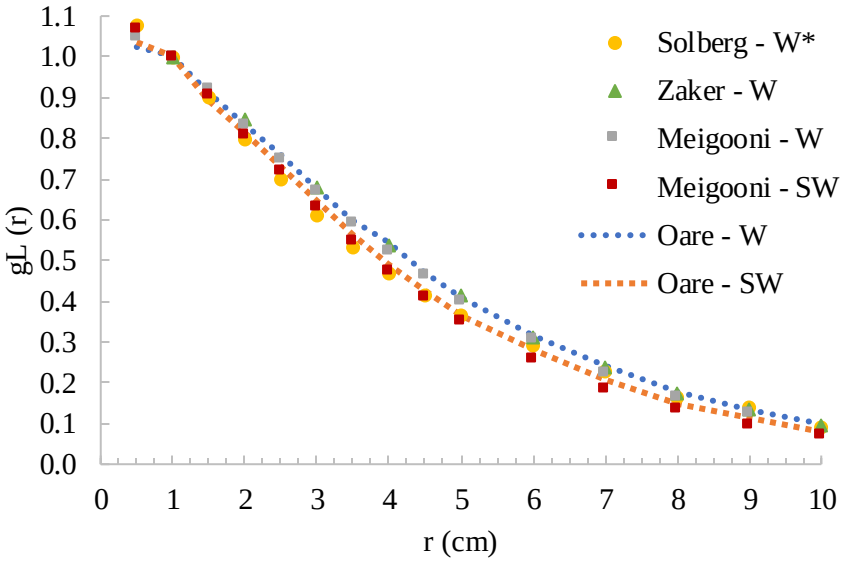

Figure 4.2 MC- Calculated Radial Dose Function
*Indicates TG-43 consensus data. W = water, SW= Solid Water

Table 4.2 Radial Dose Function Results and Comparison (Homogenous only)

Radial Distance (cm)	Oare	Solberg*	Meigooni	Zaker	Ratio Solberg/ Oare	Ratio Meigooni/ Oare	Ratio Zaker/ Oare
0.5	1.024	1.080	1.048	-	1.05	1.02	-
1	1.000	1.000	1.000	1.000	1.00	1.00	1.00
1.5	0.913	0.902	0.923	-	0.99	1.01	-
2	0.837	0.80	0.834	0.848	0.96	1.00	0.99
2.5	0.762	0.701	0.75	-	0.92	0.98	-
3	0.680	0.611	0.669	0.680	0.90	0.98	1.00
3.5	0.600	0.533	0.592	-	0.89	0.99	-
4	0.543	0.468	0.523	0.537	0.86	0.96	1.01
4.5	0.473	0.414	0.462	-	0.88	0.98	-
5	0.406	0.368	0.399	0.414	0.91	0.98	0.98
6	0.313	0.294	0.305	0.312	0.94	0.97	1.00
7	0.239	0.227	0.222	0.240	0.95	0.93	0.99
8	0.179	0.165	0.163	0.175	0.92		1.02
9	0.134	0.141	0.126	0.137	1.05		0.98
10	0.099	0.090	-	0.096			1.03
				Average:	0.94	0.98	1.00

Anisotropy Function

The anisotropy function also compared well with previous MC studies for IsoAid ^{125}I sources. Toward the source tip, at low angles, the differences are most prominent. This is likely due to variations in source encapsulation geometries. Some literature described the source end encapsulation having a maximum thickness of 0.1 mm while other work dismissed end cap thickness variation in geometry description. On average, this work compared to Solberg et al. with a ratio of 1.03, and to Meigooni et al. with a ratio of 0.99. Quantitative anisotropy results were not published by Zaker et al.

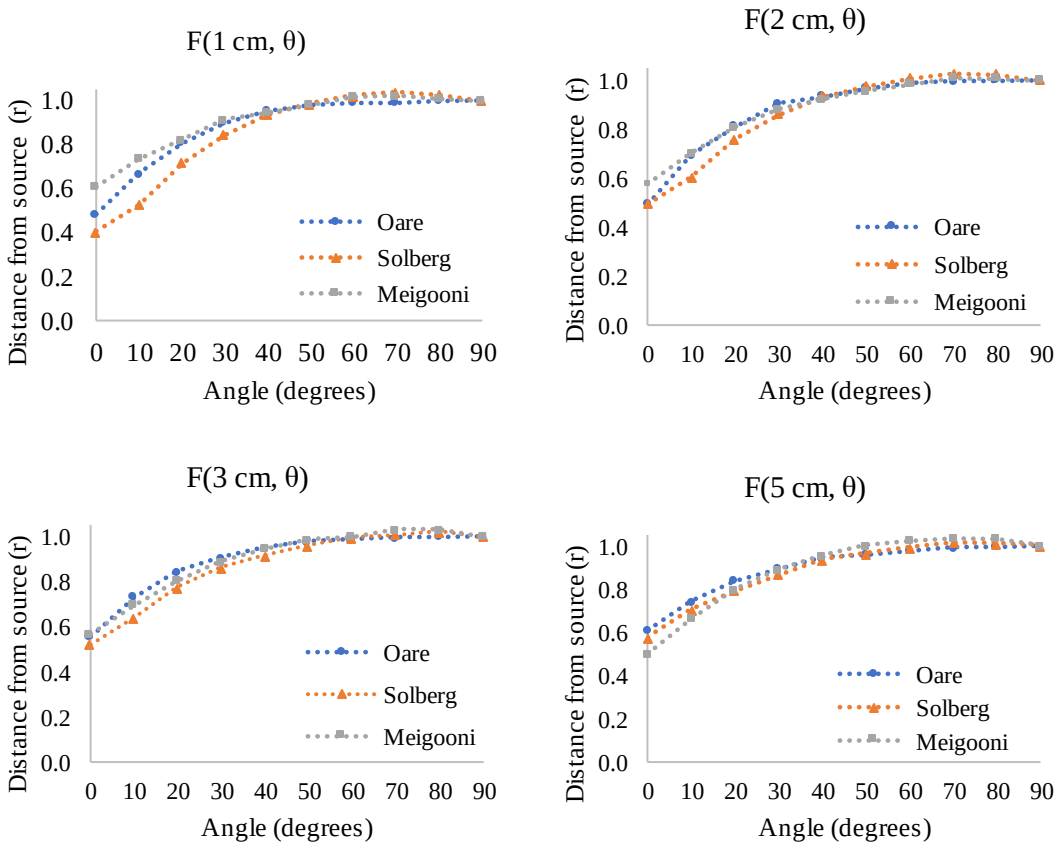

Figure 4.3 MC Calculated Anisotropy Function. This work is compared to previously reported dosimetry parameters in TG-43U1 for an IsoAid Advantage™ source[97,104,105].

4.2.2 COMS 20 mm Plaque

A 20 mm plaque was simulated with materials and seed coordinates defined in AAPM TG-129, with the inner sclera as the origin. Dose was scored at the tumor apex, eye center, lens, macula, optic disc, and inner sclera in a homogenous, water geometry (for coordinates see Table 2.3). The homogenous MC dose calculations are compared to the TPS, and TG-43 hand calculation in Table 4.3. Additionally, dose was scored in a heterogenous environment with the Silastic seed carrier and modulay backing. Homogenous-heterogeneous doses calculated with MC compared to the TG-129 report are presented in Figure 4.4 [108]. Attenuation due to seeds themselves is a concern near off-

axis dose points, where the seeds themselves change the number of photons hitting the dose target. This was evaluated by measuring dose to each structure with individual seeds vs. all 24 seeds of a 20 mm COMS plaque. It was found that interseed attenuation causes dose underestimation up to 1% on the central axis as up to 3% off axis.

Table 4.3 MC Homogenous Dose Comparison with TG-43 calculations and the TPS

	Homogenous Media Dose (Gy)		
Structure	MC	TG-43 Calc	TPS
5 mm Apex	82.8 ± 0.028	83.7	81.9
Eye Center	29.1 ± 0.004	31.0	30.7
Lens	24.6 ± 0.002	25.6	25.3
Macula	19.1 ± 0.002	20.2	20.0
Optic Disc	29.3 ± 0.002	31.7	31.2
Inner Sclera	226 ± 0.165	225.7	224.0

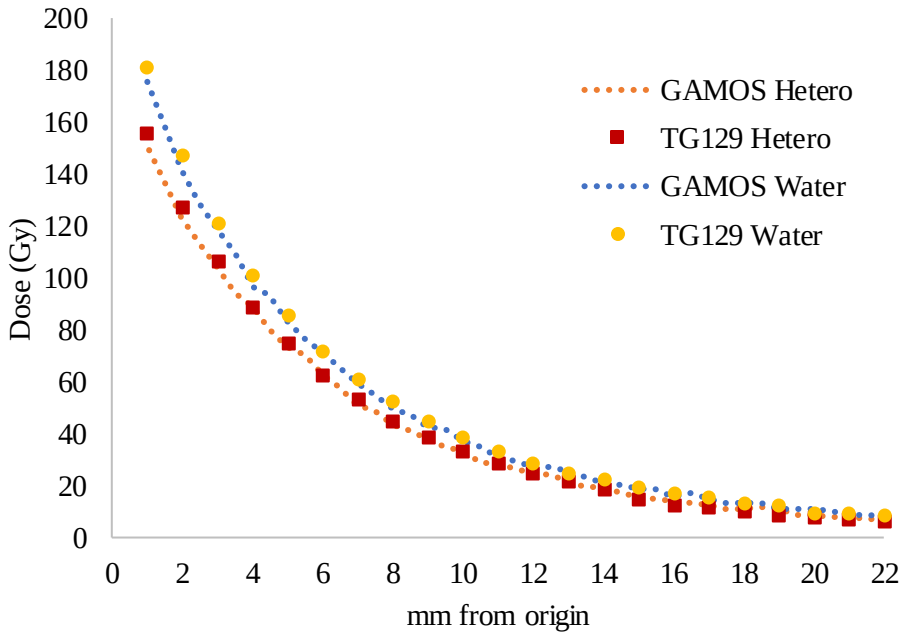

Figure 4.4 Homogenous and Heterogenous Dose: Comparison to TG-129

4.3 HVL Characterization

The film, MC, and hand-calculations for HVL and attenuation coefficients are displayed in Table 4.4 and Figure 4.5. An estimated 1.3 mm HVL is promising, indicating that only small amount of PDMS would be required to reduce dose to OARs in the eye. The EFH fluid used for film measurements in the following chapter was measured to have an HVL of 3.35 mm. PDMS is 2.6 times more attenuating than EFH.

Table 4.4 PDMS Measured HVLs and Linear Attenuation Coefficients

Method	μ (mm)	HVL (mm^{-1})
Analytical	0.551	1.26
MC	0.518 ± 0.014	1.338 ± 0.035
Film	0.541 ± 0.035	1.282 ± 0.090

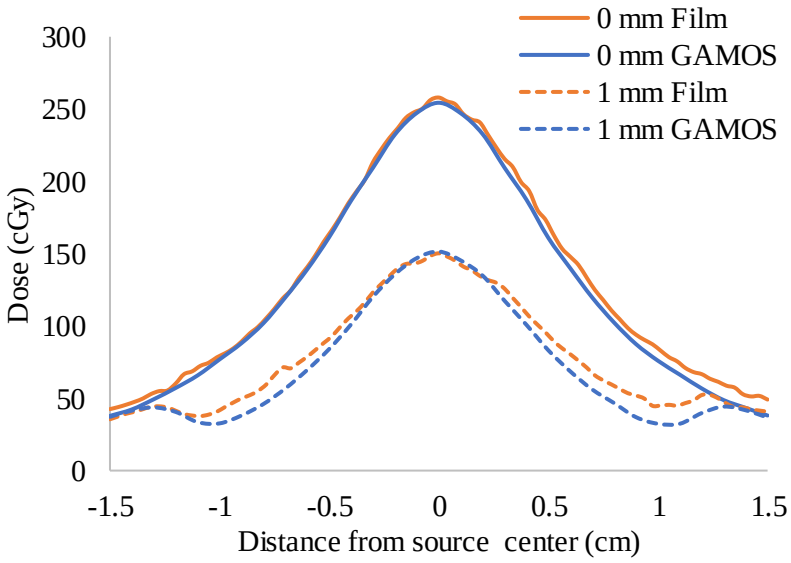

Figure 4.5 MC vs. Film Attenuation.

4.4 Film and MC-Calculated Dose Reduction to the Eye7

4.4.1 Film and MC – Measured Horizontal Dose Reduction

The EFH fluid in the presence of the magnet in the eye phantoms is shown in Figure 4.6. The fluid remains in place despite motion against gravity, proving the strength and feasibility of the custom magnet.

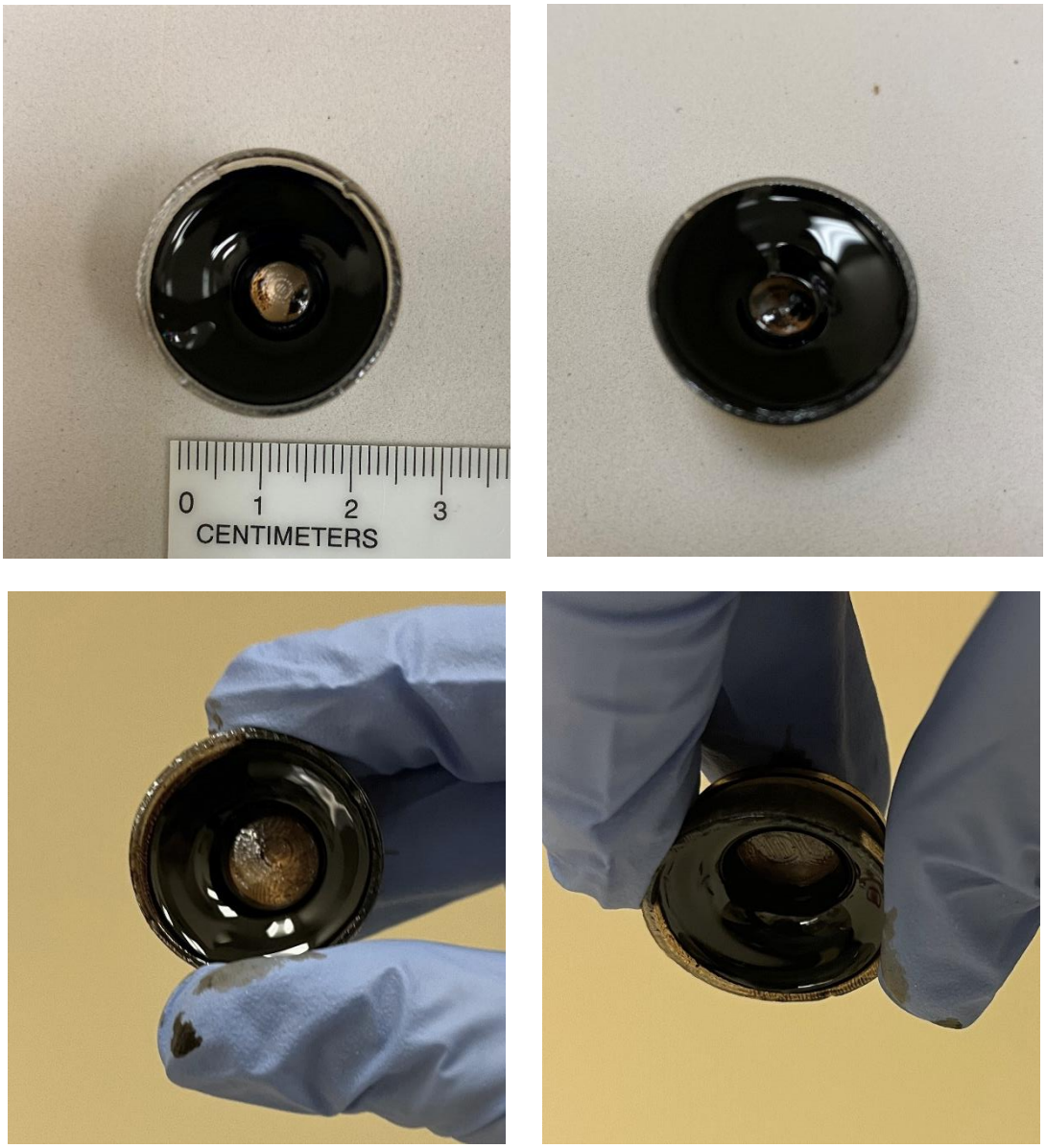

Figure 4.6 EFH Fluid Distribution with Magnet.
Top Left: 5 mm tumor, 0.8 ml EFH, *Top Right*: 8 mm tumor, 1.8 ml EFH
Bottom: Ferrofluid staying in place against gravity (3 mm tumor)

Dose to film was measured horizontal (parallel) to the plaque at the eye center (11.3 mm from the inner sclera). Since the 8 mm tumor displaced fluid, causing less dose reduction along the central axis, 1.8 ml of fluid was also measured for the large tumor height. There is agreement between film and MC-measured results (Figure 4.7), however in comparison the film appears noisy. Additionally, the 3D printed tumor adds uncertainty due to printing homogeneity and/or the consistency of the PMMA-equivalent material. When repeated with PDMS, the dose reduction can be visualized in Figure 4.8 for each tumor size and volume of added PDMS. At the eye center and periphery, the film measured EFH dose reduction percentages are shown in Table 4.5. The periphery represents a possible OAR. The results show that less than 1 ml of PDMS can reduce dose by 81, 85, and 78% for 3-, 5-, and 8-mm tumor heights. Due to the magnet and distribution of the fluid, the central dose is not reduced to the same extent.

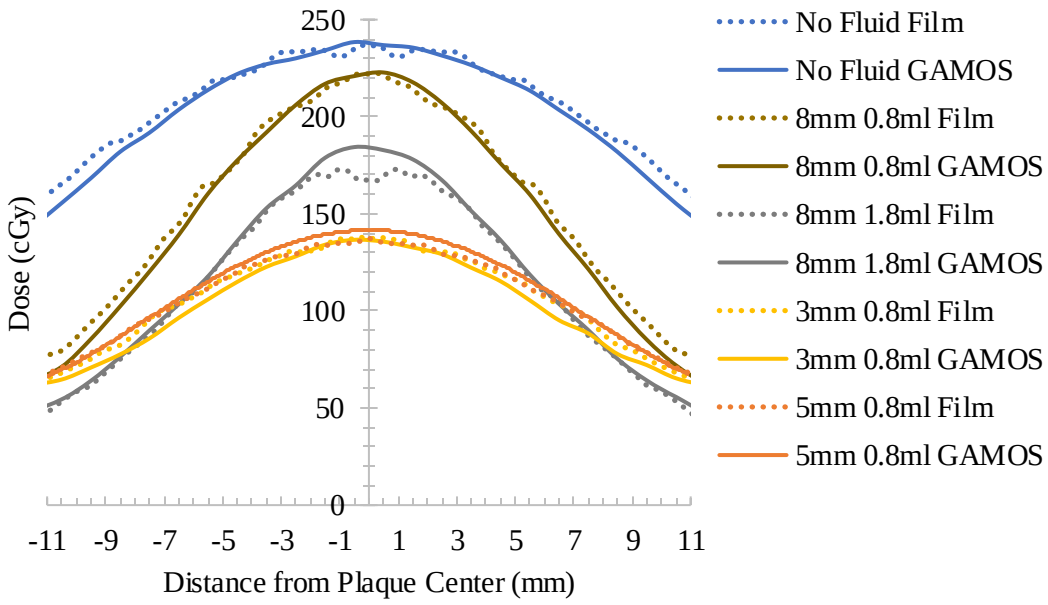

Figure 4.7 MC and Film Measured Dose Distribution with EFH Fluid.

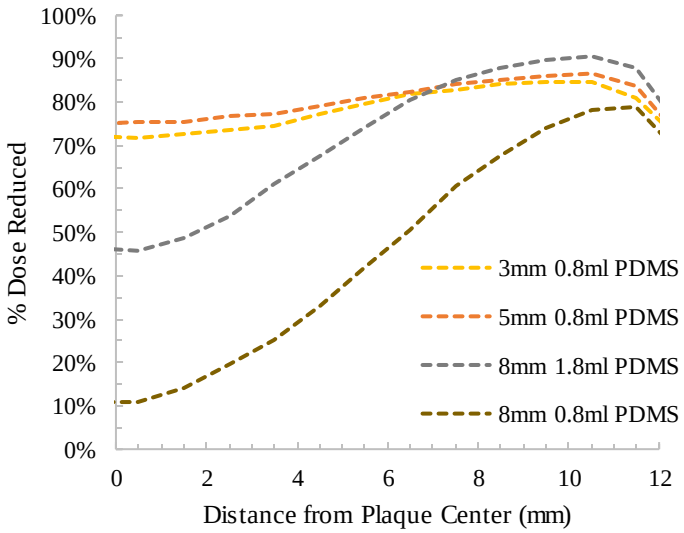

Figure 4.8 MC-Measured % Dose Reduction of PDMS

Table 4.5 Film and MC % Dose Reduction of EFH

Location (X, Y, Z)		Eye Center (11.3, 0, 0)			Eye Periphery (11.3, 11.3, 0)		
Tumor Height	Volume Fluid	Film EFH	MC EFH	MC PDMS	Film EFH	MC EFH	MC PDMS
3 mm	0.8 ml	42%	43%	**72%**	59%	58%	**81%**
5 mm	0.8 ml	42%	41%	**65%**	57%	54%	**82%**
8mm	0.8 ml	6%	6%	**11%**	52%	54%	**78%**
8 mm	1.8 ml	26%	23%	**46%**	70%	66%	**88%**

4.4.2 MC – Measured Vertical Dose Reduction

Film dosimetry is limited to a 2D planar dose distribution, and homogenous geometry (i.e., not in proximity to ferrofluid). To measure dose in areas that would otherwise be too complex experimentally, MC calculated dose distributions are used. Dose was calculated vertically with the plaque to analyze how the fluid attenuates dose throughout the eye. The dose distribution from a 20 mm COMS plaque with no fluid is present (Figure 4.9). The source strength is adjusted to

achieve the nominal 8500 cGy to water at 5- and 8-mm prescription points. Due to the heterogenous dose calculations in GAMOS, this prescription dose falls near 7440 and 7350 cGy for the 5- and 8-mm tumor heights, respectively.

Prescription Dose: 7400 cGy

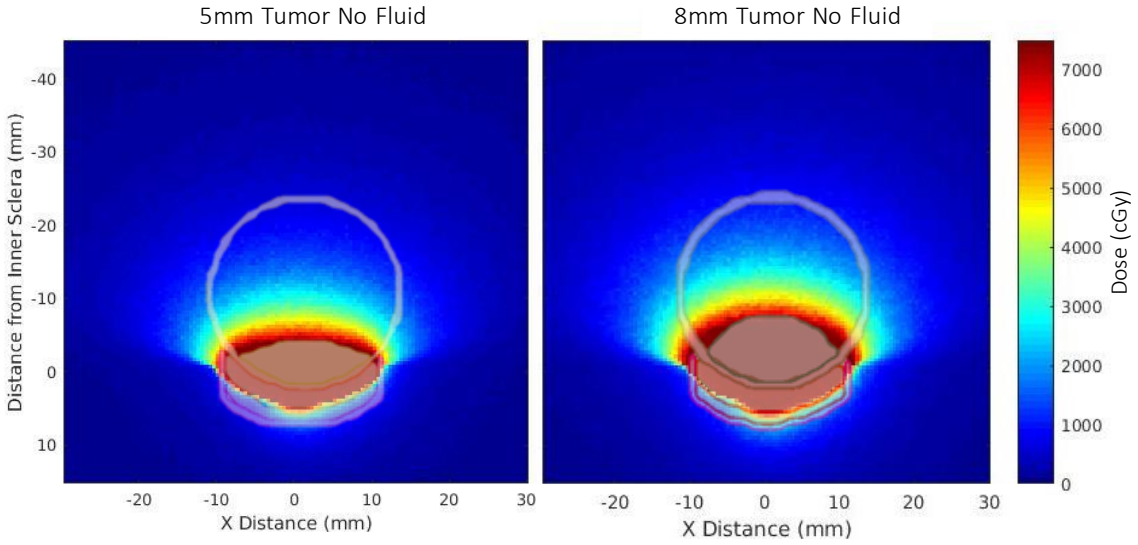

Figure 4.9 The dose distribution from a 20 mm COMS plaque with no fluid in place. A nominal dose of 8500 cGy is prescribed to the 5 and 8-mm tumor apexes (corresponding to 7400 cGy when simulated in a heterogenous MC geometry). Velocity contours are overlayed to show the eye, tumors, magnet, Silastic insert, and plaque backing.

A vertical dose distribution was calculated for the three tumor heights, with 0.8 ml of EFH or PDMS. Additionally, percent dose reduced (compared to no fluid) was plotted. For the 8 mm tumor height, 1.8 ml of EFH and PDMS was additionally simulated. Figures 4.10 – 13 display the vertical dose distribution results. In addition, percent dose reduced for increasing distance from structure to tumor margin (ST) is shown in Table 4.6 and diagrammed in Figure 4.14. Beyond 7 mm from the tumor margin the dose can be reduced by over 80 percent.

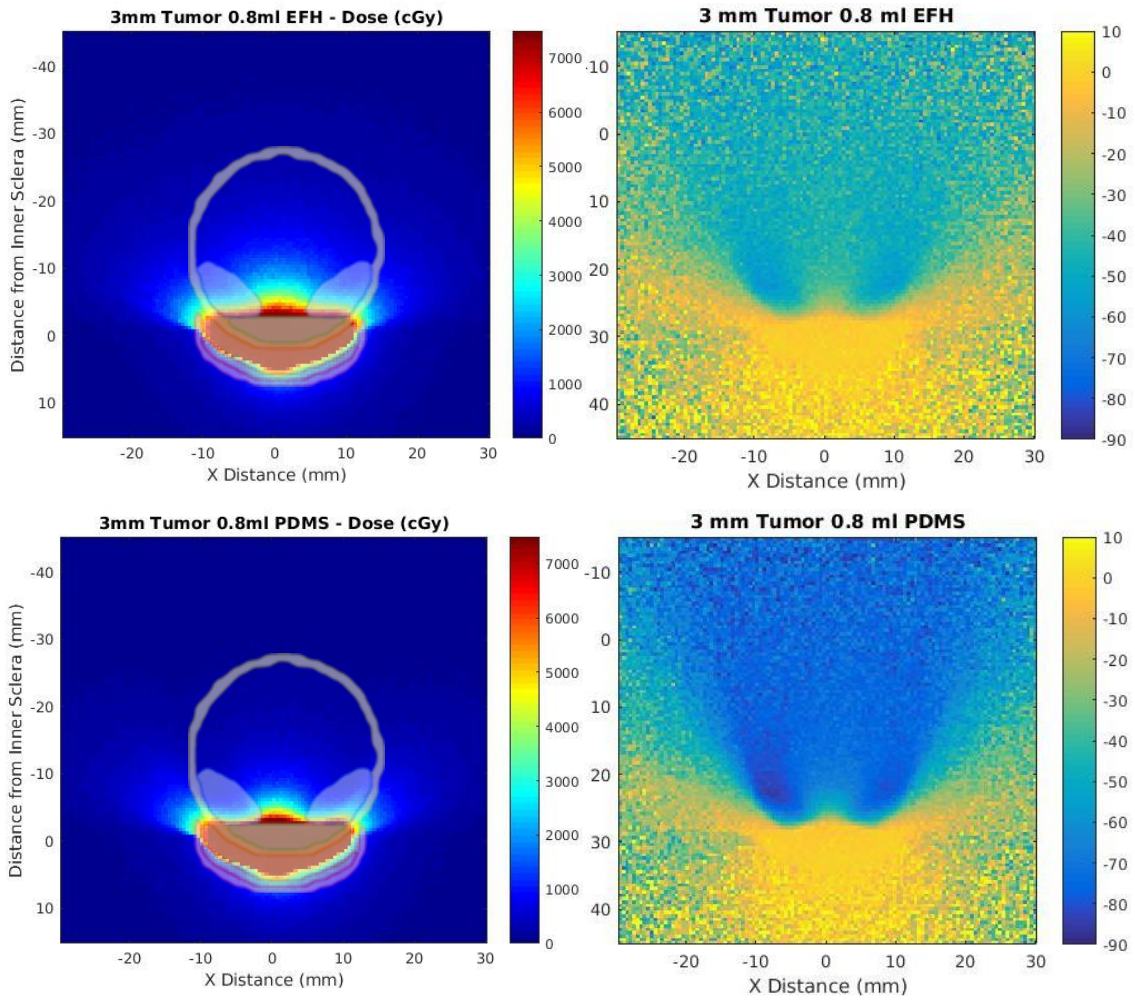

Figure 4.10 The 3 mm Tumor with 0.8 ml EFH and PDMS – Vertical Dose Reduction. EFH dose (top left) and percentage of dose reduced (top right) are shown along with the PDMS dose (bottom left) and dose reduced (bottom right). Percent dose reduced is listed as a decimal. 3 mm tumor is contoured along with the fluid distribution (blue) sclera, plaque, magnet, and Silastic insert.

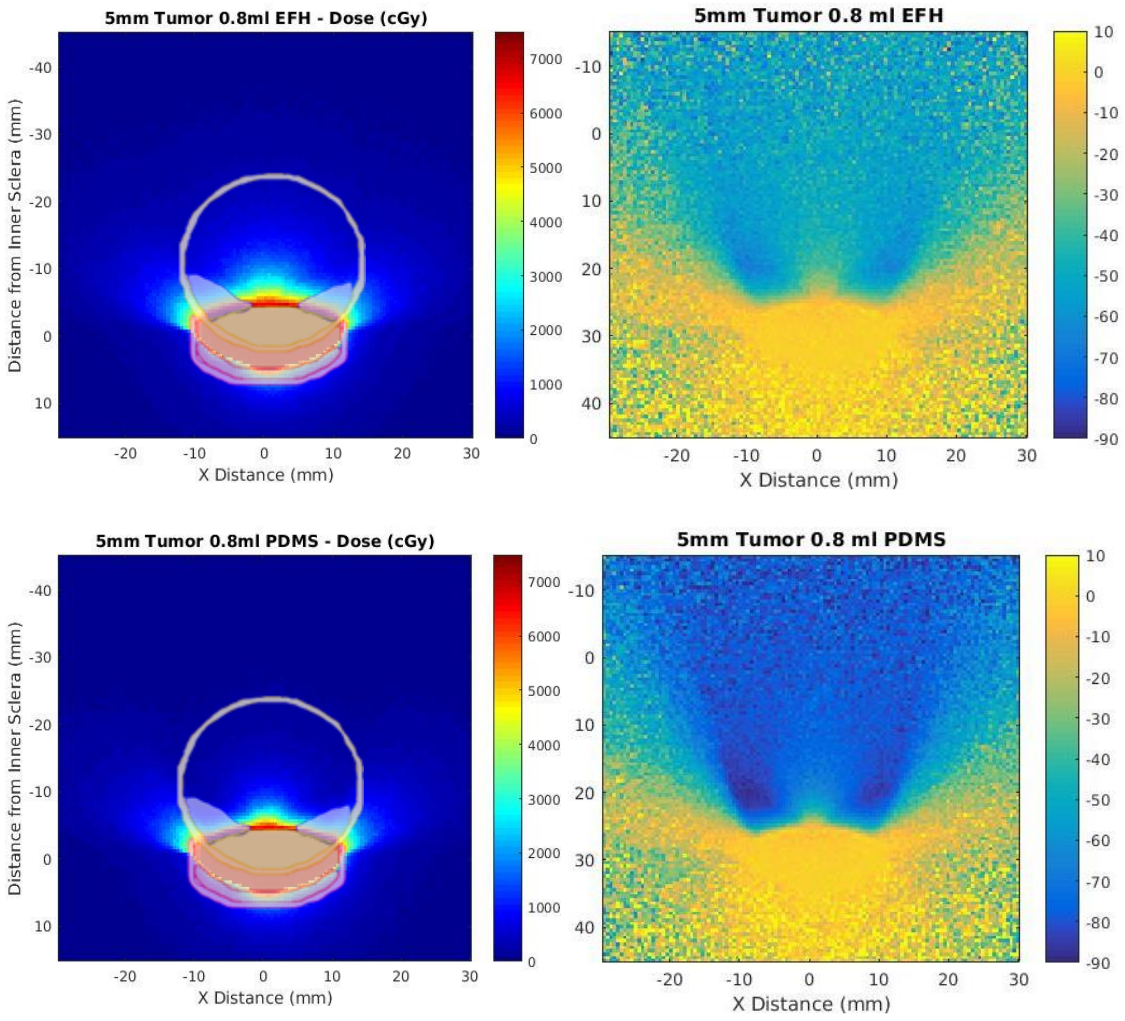

Figure 4.11 The 5 mm Tumor with 0.8 ml EFH and PDMS – Vertical Dose Reduction

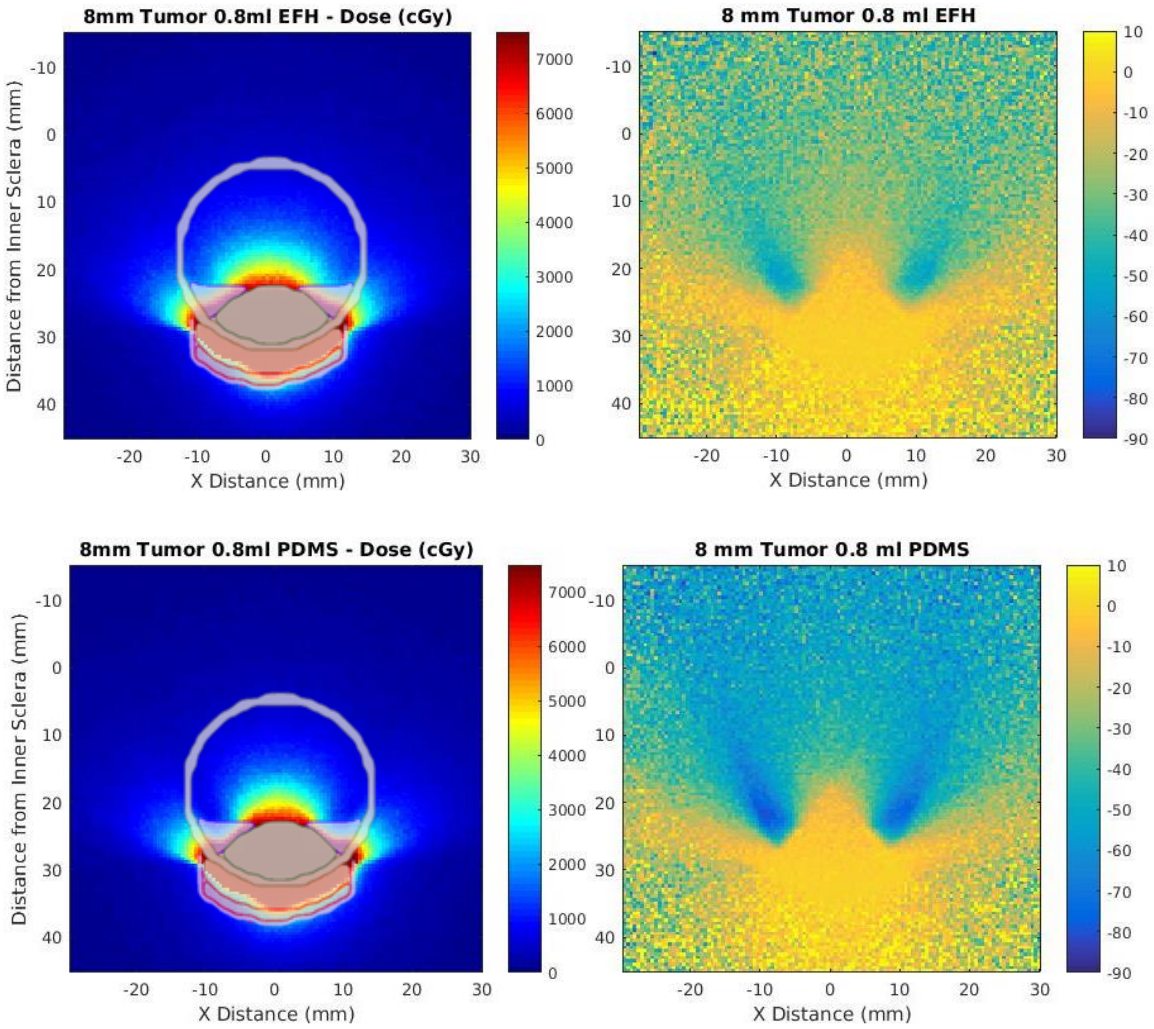

Figure 4.12 The 8 mm Tumor with 0.8 ml EFH and PDMS – Vertical Dose Reduction

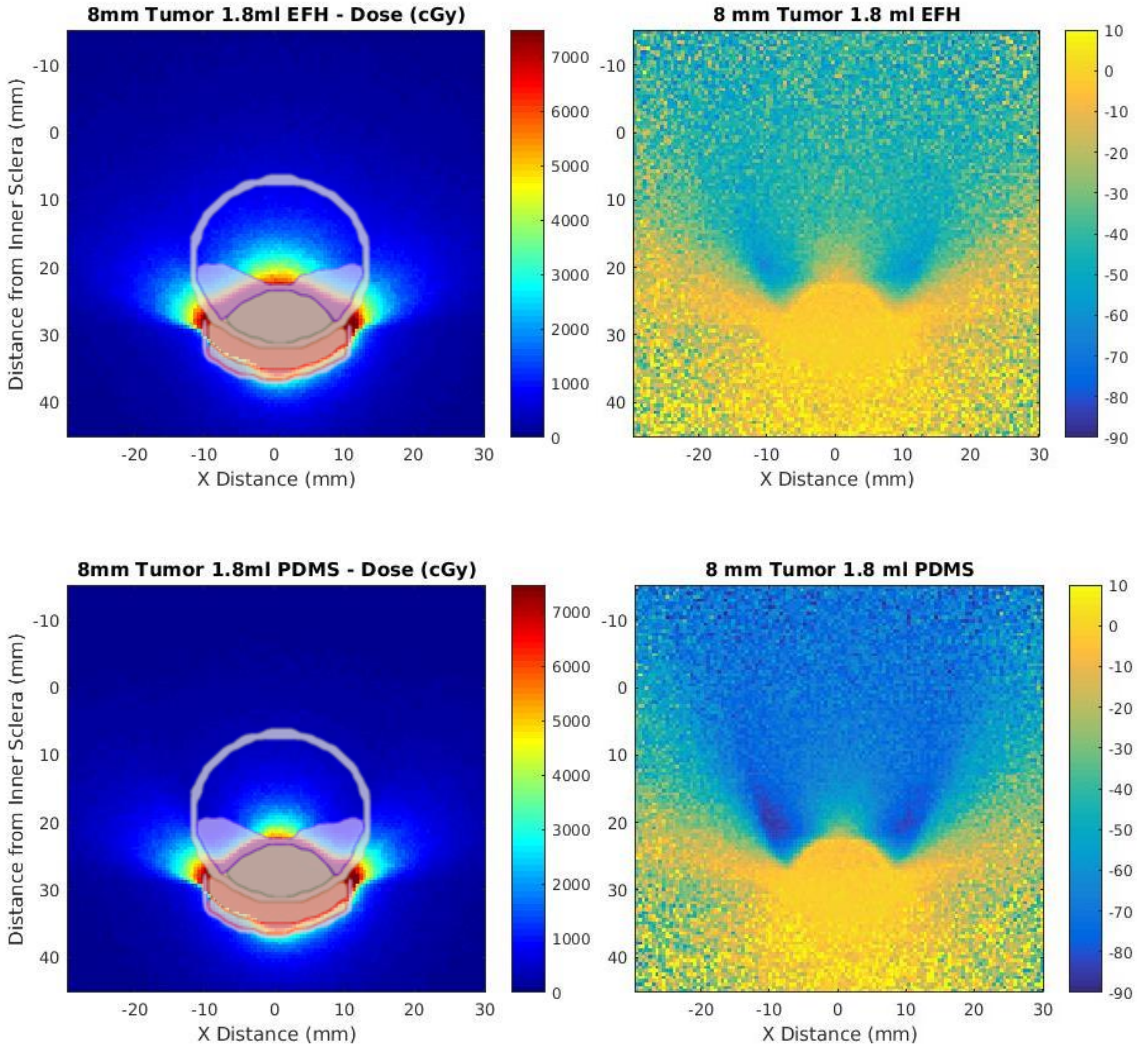

Figure 4.13 The 8 mm Tumor with 1.8 ml EFH and PDMS – Vertical Dose Reduction

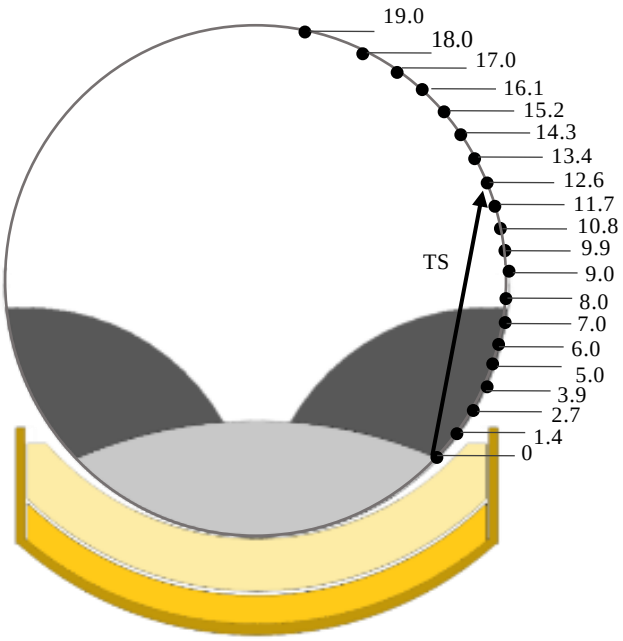

Figure 4.14 Distance from tumor margin to structures (TS) along the sclera edge of eye

Table 4.6 Percent Dose Reduced at increasing TS with 0.8ml PDMS

TS (mm)	3mm Tumor	5mm Tumor	8mm Tumor	8mm Tumor, 1.8 ml
1.4	41%	37%	38%	38%
2.7	51%	50%	49%	49%
3.9	60%	57%	58%	58%
5.0	67%	65%	65%	65%
6.0	74%	71%	73%	73%
7.0	83%	78%	80%	81%
8.0	86%	80%	83%	82%
9.0	90%	80%	85%	85%
9.9	91%	80%	83%	84%
10.8	91%	81%	82%	82%
11.7	91%	80%	77%	81%
12.6	91%	81%	75%	80%
13.4	90%	79%	72%	77%
14.3	92%	82%	73%	78%
15.2	90%	79%	69%	75%
16.1	91%	78%	65%	75%
17.0	89%	78%	65%	75%
18.0	90%	78%	64%	73%
19.0	90%	72%	65%	68%

4.5 Uncertainties

Type A and B uncertainties for GafChromic film measurements are quantified in Table 4.7. Type A, or random uncertainties, are typically the standard deviation of repeated measurements. Type B, or systematic uncertainties pertain to series of observations or measurements and can be obtained based on manufacturer specifications, calibration data, or behavior of the materials and measurement tools utilized. Uncertainties are combined using a square root of the sum-of-the-squares.

MC transport simulations were run with enough histories to achieve <1% error. The materials and geometries used in MC transport simulations are based on manufacturer specifications, however products like VeroClear (3D-printed phantom) or EFH fluid did not have detailed specifications for elemental composition by weight. Therefore, the accuracy in MC attenuation calculations for EFH fluid are not as accurate as PDMS calculations with a known material composition. The tumor phantom in MC calculations was assumed to be water. Lastly, the fluid distribution in the presence of a magnet was modeled off physical measurements and from MVCT images. MVCT images had a resolution >2mm, which adds uncertainty when measuring fluid geometry. These quantified film uncertainties and MC uncertainties explain the differences that are seen in Figures 4.6 and Table 4.5.

The estimated total uncertainties are calculated for single source film measurements (HVL measurements) as well as COMS plaque measurements (which required consideration of added positional errors and the Silastic insert thickness). Total uncertainties were estimated to be 8.0% for single source film measurements and 10.1% for loaded COMS plaque film measurements (Table 4.7).

Table 4.7 Film Measurement Estimated Uncertainties

Measurement Description	Relative Propagated Uncertainty (%)		Reference
I. Dose to Water for Single ^{125}I Source			
	Type A	Type B	
Source Position*		6.0	
Transfer of AKS from ADCL to NIST to clinic		2.6	TG-138
Source strength**		1.9	
Exposure time		0.1	
Combined Uncertainty	0.0	6.8	
Total Uncertainty	6.8		
II. Dose to Water for COMS Plaque			
	Type A	Type B	
Source Position***		8.0	
Silastic Insert Thickness		2.0	
Calculation compared to TPS		2.0	
Transfer of AKS from ADCL to NIST to clinic		2.6	
Source strength**		1.9	
Exposure time		0.1	
Total Uncertainty	9.1		
III. EBT3 Film			
	Type A	Type B	
Response curves, fitting procedure		3.0	
Dose resolution of the system		1.8	
Film reproducibility	0.2		
Film uniformity		0.2	
Relative orientation of the film		0.2	
Reproducibility of the response of scanner	0.3		
Homogeneity of scanner		2.0	
Read out time (24 vs 72 hours)		1.0	
Combined Uncertainty	0.4	4.2	
Total Uncertainty	4.2		
Total and Expanded Uncertainty	**(k = 1)**	(k=2)	
Dose to Water for ^{125}I Source + EBT3 Film + MC	**8.0**	16.0	
Dose to Water for COMS Plaque + EBT3 Film + MC	**10.1**	20.1	

*Inverse Square Law for measurements displaced by 0.3 mm at 11 mm from the source

**Measured source strength is compared to manufacturer-determined source strength

***Inverse Square Law, plus possible angular rotation of the plaque by ±2°

4.6 Discussion

The results from film and MC measured attenuation demonstrate that a low HVL (1.29 mm for PDMS) would only require a small volume to limit dose to normal tissues of the eye. The designed concave magnet attracted fluid toward the edge of the plaque, where high tissue dose is probable. The horizontal film and MC measurements indicate strong agreement between the phantom measurements and simulated plaque. All three tumor heights and fluid volumes modeled in MC simulations matched film measurements well within the estimated uncertainty. This finding implies that with careful fluid geometry, MC simulations are a suitable and efficient way to simulate fluid attenuation for futures studies or treatment planning applications.

MC calculated vertical dose distribution best displays dose reduced throughout the eye. The most clinically useful results come from Table 4.6, showing percent dose reduced at increasing tumor to structure (ST) distances. Such information can help a physician or physicist determine how much dose reduction is expected given the tumor size and ST distance. To illustrate, a 20 mm COMS plaque patient experiencing radiation retinopathy is pulled from the retrospective study. The patient had a 4.2 mm tumor height. Distance and dosimetry data are recorded in Table 4.8. Data from Table 4.6 is interpolated to measure dose reduction for structures around the 4.2 mm tumor height. With less than 1 ml PDMS it is estimated that the patient's new dose to the macula, optic disc and lens would reduce to 9.2, 4.6, and 5.9 Gy, respectively.

Table 4.8 Example of Patient Dose Reduction

OAR	Distance to Tumor Margin (mm)	Original Dose (Gy)	Dose with 0.8ml PDMS (Gy)
Macula	9.7	69.9	9.4
Optic Disc	12.8	32.2	4.2
Lens	16.7	14.42	5.9

The example in Table 4.7 demonstrates the extent of dose reduction COMS patients can achieve. It is likely that this patient would not have incurred radiation side effects with the extensive attenuation provided by the PDMS fluid. The results in Figure 4.6 also tell us that at ST > 2.7 mm, 50% or more of the dose is reduced with only 0.8 ml of PDMS. Referring to Chapter 3 Table 3.6, it was noted that 50% of the dose reduced to the OARs would reduce the number of patients with D_{Macula}>52 Gy, D_{OD}>42 Gy, and D_{Lens}>16Gy from 50% to 21, 15, and 12%, respectively. This implies that tissues with ST > 2.7 mm are estimated to have smaller probabilities of unwanted side effects. These proportions are an underestimate, as dose reduction increases beyond 50% with increasing distance from the tumor margin.

During horizontal film measurements the 8 mm tumor showed a reduced central dose axis compared to the smaller tumor heights studied. This led to the evaluation of 1.8 ml EFH for the 8 mm tumor height. Interestingly, the peripheral dose was less affected by the tumor size than the central dose. Despite the original logic that larger tumors may require more fluid volume, adequate OAR coverage is achievable with small volumes (<1 ml) of fluid. When using such small fluid volume, vitreal replacement during the implant may be unnecessary.

Advantages

The attenuation results presented in this work are more extensive and feasible compared to patients undergoing proton therapy, or existing intraocular shielding interventions. The designed plaque has the same source geometry, therefore no momentous change to treatment planning is necessary. Proton therapy is advantageous to tissues in close proximity of the tumor due to minimal exit dose, but tissues falling in the path of the entrance dose may cause unwanted side effects including cataract formation, or loss of clinically useful vision years after treatment[58]. Additionally, proton centers lack accessibility for all patients, making the PDMS-Magnetic plaque the most accessible and effective method to reduce unwanted side effects.

While silicone oil has proven to be a strong intraocular shield, the magnitude of attenuation from PDMS is much more effective. Oliver et al. simulated a silicone filled eye with a 16 mm COMS plaque. At 7.6 mm from the tumor margin, silicone oil (filling the entire vitreous) achieves up to 35% dose reduction. In comparison, it is estimated that PDMS would achieve over 80% dose reduction at this distance from the tumor. In addition to more attenuation, especially closer to the tumor margin, PDMS intraocular shield would require a smaller amount and be removed from the eye, limiting long term exposure of an external media in the eye.

Limitations

Only the 20 mm COMS plaque was used in this work. Further data should be collected before applying results to other plaque sizes. Additionally, only three tumor heights were evaluated for fluid and dose distribution. While the results could be interpolated, future work may involve more tumor heights simulated MC, especially large 10 mm tumors, or an interpolation of the data evaluated. Only heterogeneous plaque measurements were performed.

Low energy dosimetry poses many challenges and limitations, which is highlighted in Table 4.8 of itemized uncertainties. Slight changes in distance present large errors due to the steep dose gradient of brachytherapy sources. Therefore, the setups used for film calibration and fluid measurements have high uncertainty values (8 and 10%). Additionally, comparison among film and MC fluid measurement is difficult due to discrepancies in fluid geometry around the magnetic field. Fluid volume and shape were simulated as closely as possible based on measurements and MVCT imaging, as well as volume calculations in GAMOS.

Lastly, film plaque measurements were only performed with EFH. When significant quantities are available, PDMS measurements should be performed to complement the MC results. Despite these limitations, film and MC measurements prove that the proposed magnet and fluid amount can significantly reduce dose at normal tissue coordinates.

CHAPTER 5: MULTIPHYSICS SIMULATION RESULTS

5.1 Magnetic Field and Gauss Lines

The modeled NdFeB magnet, magnetic field lines, and flux density is shown in Figure 5.1. The maximum magnetic flux density is 1.44 T. The gaussian lines are shown in Figure 5.2 and Table 5.1.

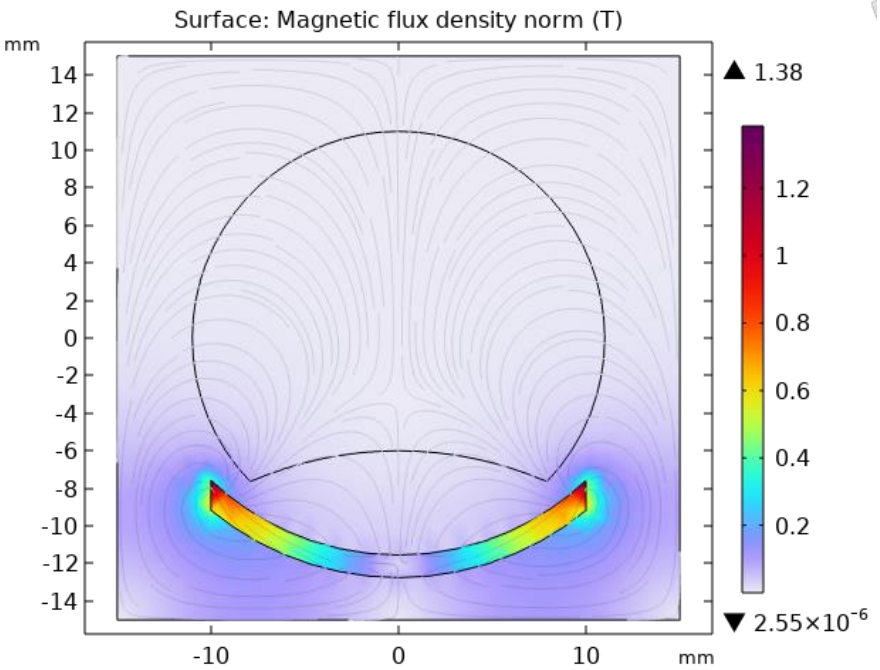

Figure 5.1 Custom Magnet, Flux Density and Magnetic Field Lines

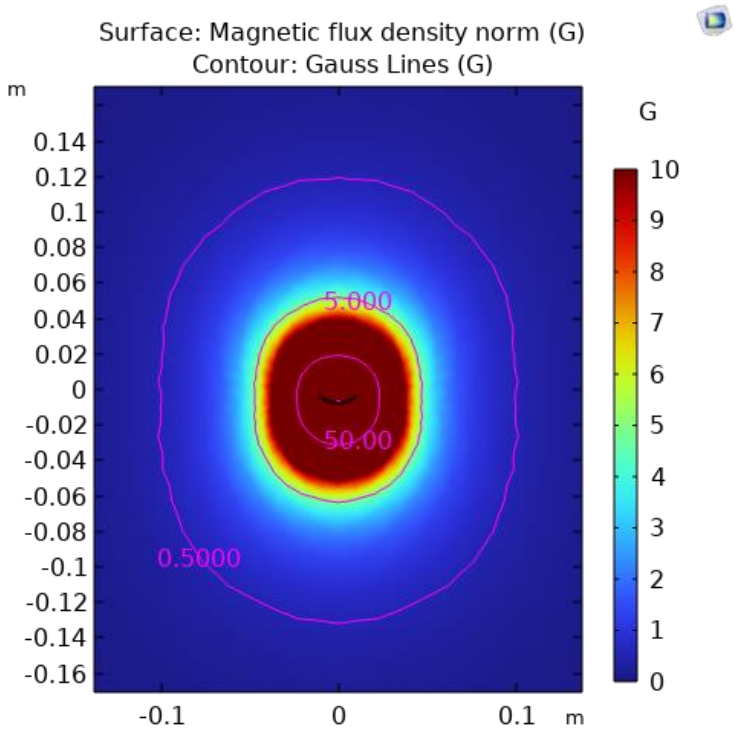

Figure 5.2 Gauss Lines – Custom Magnet

Table 5.1 Gauss Lines - Custom Magnet

Gauss (G)	Vertical Distance (m)
50	0.03
5	0.05
0.5	0.13

Based on the modeled magnet and simulation calculations, the following recommendations should be made for patients with an implanted magnet: (i) patients should avoid proximity to ferromagnetic objects and keep a 30 cm radius from potential hazards; (ii) patients should not undergo MRI imaging while device is implanted. The recommended distance of 30 cm is an overestimate that can be used for added precaution. According to the COMSOL simulations, beyond 13 cm the magnetic flux density is lower than the earth's magnetic field (0.5 G). In comparison, for MRI safety the 5 Gauss line is used as a precautionary distance to avoid

ferromagnetic objects and magnetic field exposure to the general public. At close distances to the eye with a magnetic implanted device, especially within the 5 Gauss line (5 cm), patients should avoid ferromagnetic alloys or materials containing considerable amounts of iron, nickel, or cobalt.

Further studies need to be addressed to determine the safety of a ferromagnetic implant for patients with cochlear implants, insulin pumps, cardiac pacemakers, or other electronically active devices that exist within 13 cm of the eye. Common hazards may also include, but are not limited to stainless steel appliances, cookware, whiteboards, or even eyeglasses. Based on the magnetic field produced by the plaque, it is proposed that patients wear a magnet on a necklace the week prior to implant to become familiar with potentially hazardous ferromagnetic materials.

5.2 Fluid Flow

The fluid's ability to move against the direction of gravity is displayed in Figure 5.3. The remaining figures display the fluid flow out of a needle toward a 3-, 5- and 8-mm tumor height. The fluid moves briskly toward the magnet edges, where the magnetic flux density is strongest, creating a torus shape. In the 8mm tumor (1.8 ml of fluid), the larger amount of fluid creates more shielding along the edge of the eye and tumor.

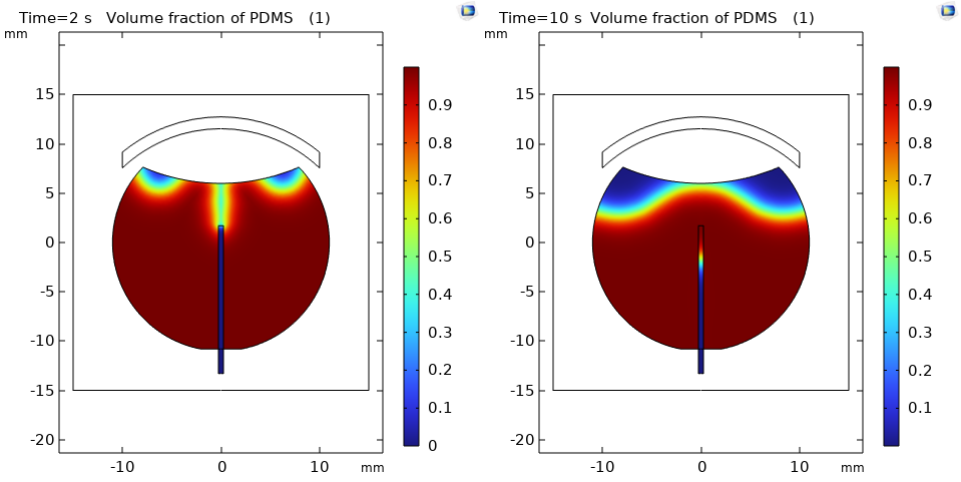

Figure 5.3 Fluid flowing toward a 5 mm tumor height against the direction of gravity.

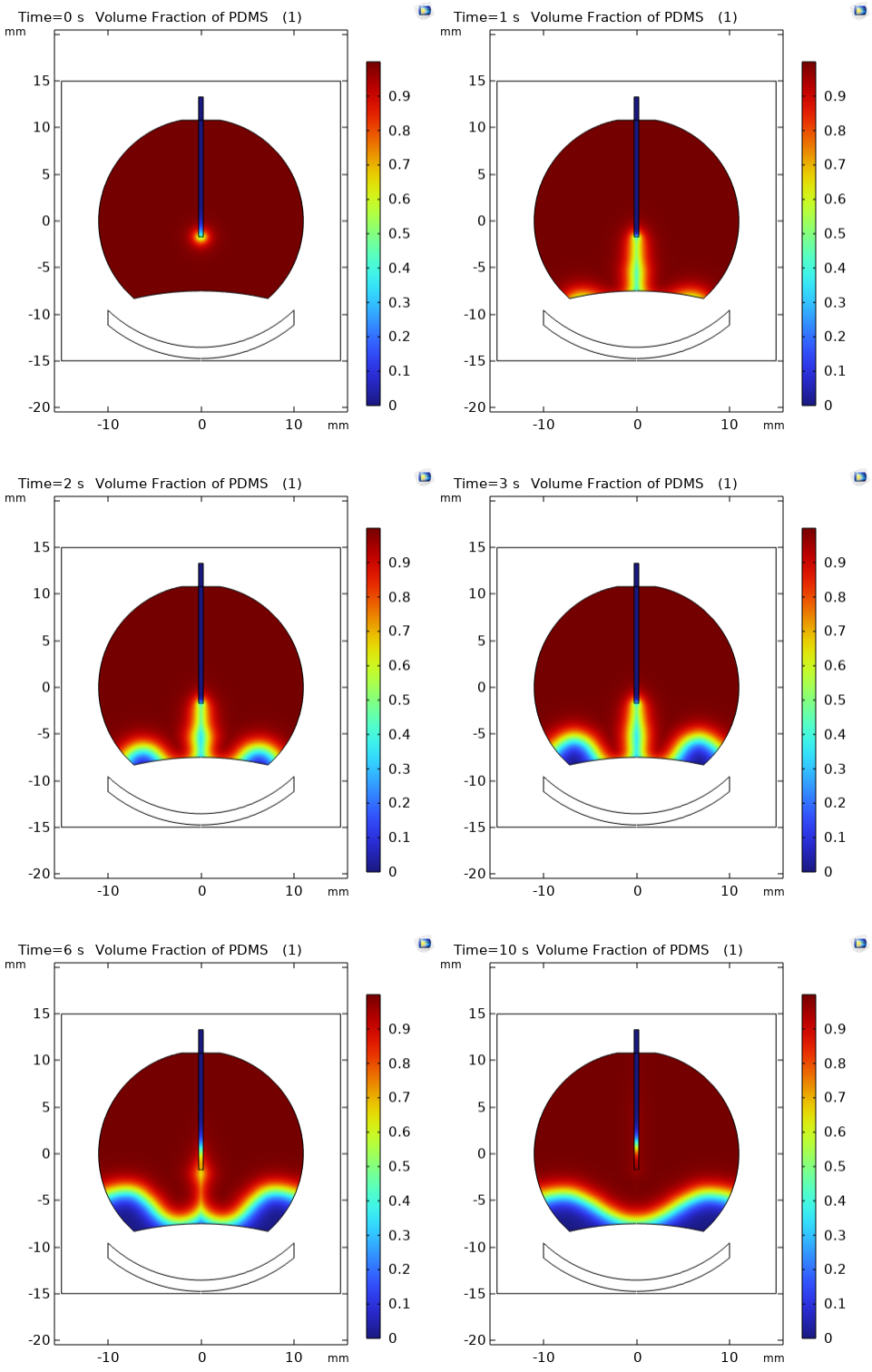

Figure 5.4 Fluid flow modeled in a 3 mm tumor – 0.8 ml PDMS

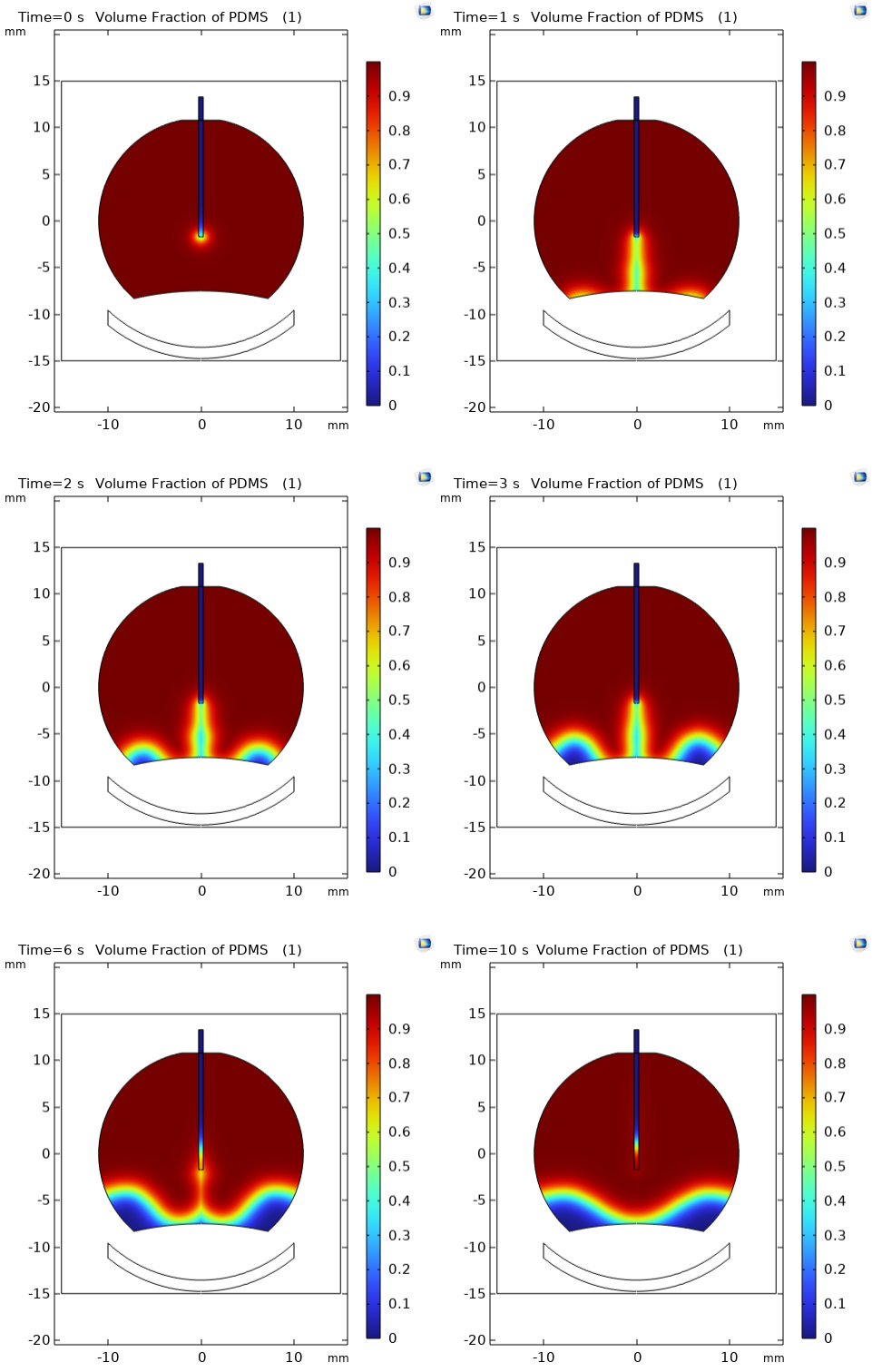

Figure 5.5 Fluid flow modeled in a 5 mm tumor – 0.8 ml PDMS

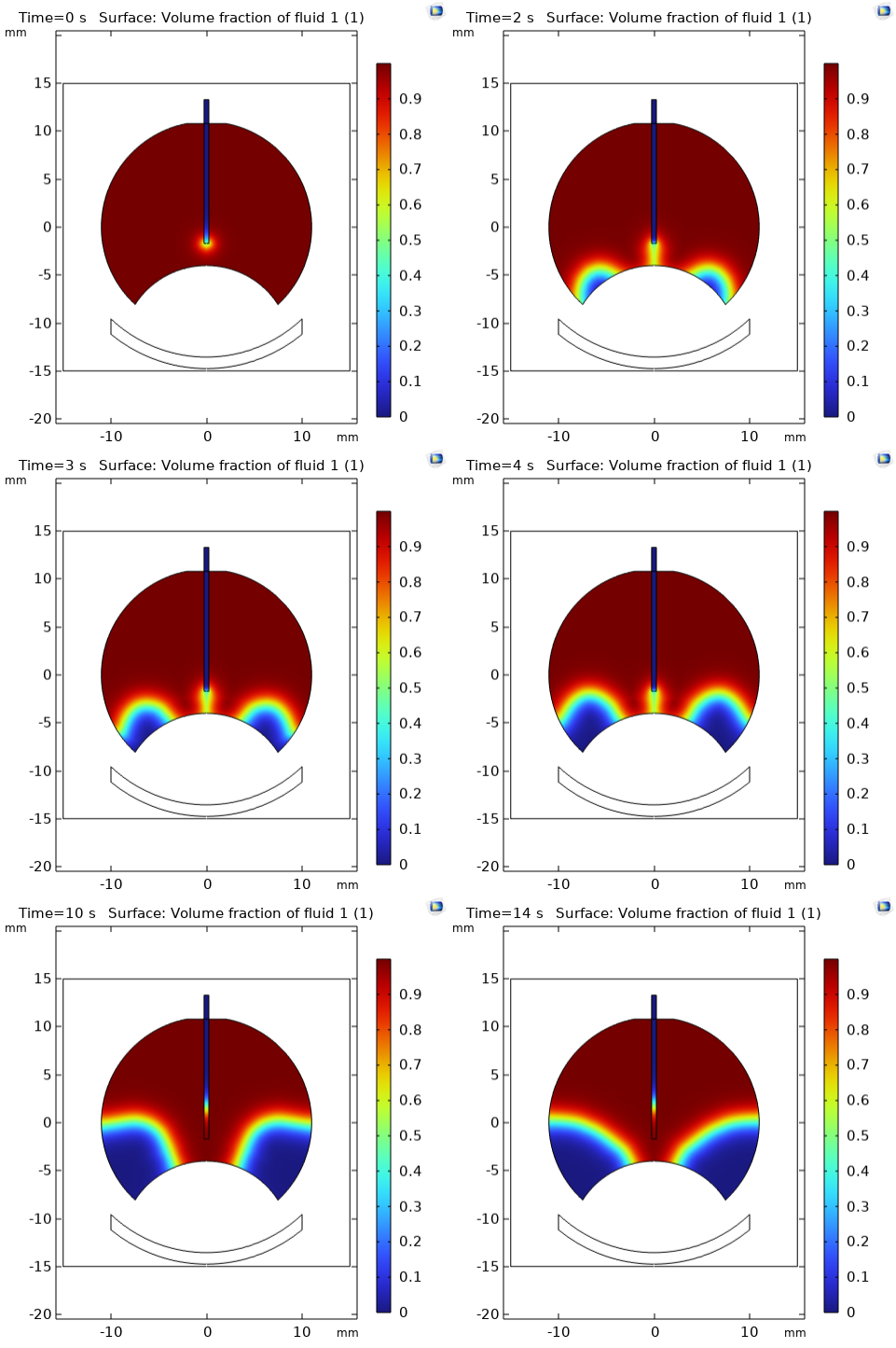

Figure 5.6 Fluid flow modeled in an 8 mm tumor – 1.8 ml PDMS

CHAPTER 6: CONCLUSIONS AND RECOMMENDATIONS FOR FUTURE WORK

In this work a novel intraocular shielding device was introduced and evaluated to limit excessive normal tissue dose in eye plaque brachytherapy for uveal melanoma patients. By effectively limiting high dose to normal tissue, the chance of complications after brachytherapy may decline. The prototype was designed with minimal modifications to the existing COMS plaque and treatment planning techniques. Three goals were completed in this work. The first was to retrospectively determine toxicity incidence rates for normal tissues, in addition to defining reasonable dose levels to avoid such toxicities. The second was to characterize the fluid attenuation properties and evaluate the effectiveness of the plaque prototype with film dosimetry and Monte Carlo (MC) calculations. Finally, Multiphysics simulations characterized fluid flow in addition to the discussion of properties and safety consideration of the magnetic plaque.

The need for effective dose reduction strategies was outlined in the retrospective study. Most patients experienced radiation retinopathy and/or cataracts. Around 40% of patients experience moderate vision decline. The relative risk analyses showed that high dose to the macula and optic disc are related to radiation retinopathy and vision decline while cataracts are related to high lens dose. Additionally, radiation retinopathy overtime may depend on a macula dose >52 Gy and an optic disc dose >42 Gy. Patients approaching these planned dose levels should be counseled accordingly to alleviate likely side effects. Such patients would be candidates for the proposed intraocular shielding device.

The attenuation properties of PDMS-Magnetite were evaluated with film and MC methods. The PDMS fluid had a measured HVL of approximately 1.29 mm. The fluid moved briskly toward the convex magnet, creating a torus-like fluid shape, which provides excellent coverage to normal tissue points near the plaque edge. EFH measurements showed more attenuation along the edge of

the eye rather than the central axis. This is beneficial as the need for attenuation and dose reduction axis along the sclera or periphery of the eye. It was shown that film and MC EFH fluid measurements agreed, therefore PDMS measurements were conducted with MC simulations. Small amounts of PDMS (<1 ml) showed that at distance greater than 2.7 mm from the tumor edge, normal tissue dose can be reduced by more than 50%. This value approaches 80% or more with increasing distance from the tumor. Such levels of dose reduction can significantly reduce likelihood of normal tissue toxicity after plaque brachytherapy for uveal melanoma patients.

The magnetic plaque design proved to be effective in moving the PDMS briskly and around the tumor. The NdFeB magnet is strong enough to work against gravity or other forces due to motion of the eye. Additionally, the magnetic flux density proved to be minimal at distances greater than 13 cm from the plaque.

Future work should include pre-clinical trials and implementation of modified treatment planning for the proposed intraocular device. Most brachytherapy TPS do not correct for inhomogeneities, therefore a correction factor would need to be considered for normal tissues points with the expected amount of shielding [109]. Future work might also involve the evaluation of various plaque diameters, tumor sizes, and fluid amounts using MC methods. It may be possible to create a table of expected dose reduction based on the plaque diameter, tumor size, volume of fluid, and the normal tissue coordinate, similar to Table 4.6. Additionally, COMSOL simulations could be created for individual tumor sizes and fluid volumes for treatment planning purposes.

In addition, the PDMS fluid synthesis should be reproducible and designed to yield higher quantities to meet the needs of uveal melanoma patients. The magnetic plaque and fluid will require sterilization at temperatures below 100 degrees Celsius to protect the intrinsic magnetic properties, such as EO gas sterilization. Moreover, the fluid will require further biocompatibility testing to work toward FDA approval of a PDMS intraocular shielding device. Histology evaluation in vitro

and in vivo are the next steps in determining the safety and efficacy of the proposed device. Collaboration among physicists, polymer chemists, radiation oncologists, and surgical ophthalmologists is crucial.

In many aspects of radiation therapy, normal tissue limits dictate the treatment planning process to achieve best possible outcome and quality of life for the patient. Management of excessive dose should be a new priority in eye plaque brachytherapy with the introduction of this high-Z intraocular shielding device. This study provided proof of concept that the intraocular shielding method can significantly reduce the likelihood of normal tissue radiation toxicity for uveal melanoma patients.

BIBLIOGRAPHY

[1] Tanderup K, Ménard C, Polgar C, Christian J, Kirisits C, Pötter R. Advancements in brachytherapy. Adv Drug Deliv Rev 2017;109:15–25. https://doi.org/10.1016/j.addr.2016.09.002.

[2] Nath R, Anderson LL, Luxton G, Weaver K, Williamson J, Meigooni A. Dosimetry of interstitial brachytherapy sources: Recommendations of the AAPM Radiation Therapy Committee Task Group No. 43. Med Phys 1995;22:209–34.

[3] International Commission on Radiation Units and Measurements. Dose and Volume Specifications for Reporting Intracavitary Therapy. ICRU Report No. 38. Bethesda, MD: 1985.

[4] Kahn F, Gibbons J. The Physics of Radiation Therapy. 5th ed. 2014.

[5] Chiu-Tsao ST, Astrahan MA, Finger PT, Followill DS, Meigooni AS, Melhus CS, et al. Dosimetry of 125I and 103Pd COMS eye plaques for intraocular tumors: Report of Task Group 129 by the AAPM and ABS. Med Phys 2012;39:6161–84. https://doi.org/10.1118/1.4749933.

[6] Margo CE. The collaborative ocular melanoma study: An overview. Cancer Control 2004;11:304–9. https://doi.org/10.1177/107327480401100504.

[7] Jovanovic P, Mihajlovic M, Djordjevic-Jocic J, Vlajkovic S, Cekic S, Stefanovic V. Ocular melanoma: An overview of the current status. Int J Clin Exp Pathol 2013;6:1230–44.

[8] Aronow ME, Topham AK, Singh AD. Uveal Melanoma: 5-Year Update on Incidence, Treatment, and Survival (SEER 1973-2013). Ocul Oncol Pathol 2018;4:145–51. https://doi.org/10.1159/000480640.

[9] Moore R. Choroidal sarcoma treated by the intraocular insertion of radon seeds. Br J Ophthalmol 1930;14:145–52. https://doi.org/10.1136/bjo.14.4.145.

[10] Moore R, Stallard H, Milner J. Retinal gliomata treated by radon seeds. Br J Ophthalmol 1931;15:673–96. https://doi.org/10.1136/bjo.15.12.673.

[11] Stallard H. Radiotherapy of malignant intra-ocular neoplasms. Br J Ophthalmol 1948;32:618–39. https://doi.org/10.1136/bjo.32.9.618.

[12] Stallard H. Radiotherapy for malignant melanoma of the choroid. Br J Ophthalmol 1966;50:147–55. https://doi.org/10.1136/bjo.50.3.147.

[13] Lommatzsch PK. Experiences in the treatment of malignant melanoma of the choroid with 106Ru-106Rh beta-ray applicators. Trans Ophthalmol Soc United Kingdom 1973;93:119–32.

[14] Sealy R, le Roux PL, Rapley F, Hering E, Shackleton D, Sevel D. The treatment of ophthalmic tumours with low-energy sources. Br J Radiol 1976;49:551–4. https://doi.org/10.1259/0007-1285-49-582-551.

[15] Stannard C, Sauerwein W, Maree G, Lecuona K. Radiotherapy for ocular tumours. Eye 2013;27:119–27. https://doi.org/10.1038/eye.2012.241.

[16] COMS Group. Collaborative Ocular Melanoma Study Group. Design and methods of a clinical trial for a rare condition: The Collaborative Ocular Melanoma Study.

COMS Report No. 3. Control Clin Trials 1993;14:362–91. https://doi.org/https://doi.org/10.1016/0197-2456(93)90052-F.

[17] COMS Group. The Collaborative Ocular Melanoma Study (COMS) randomized trial of pre-enucleation radiation of large choroidal melanoma II: initial mortality findings COMS report no. 10. Am J Ophthalmol 1998;125:779–96. https://doi.org/https://doi.org/10.1016/S0002-9394(98)00039-7.

[18] Marr B. The COMS randomized trail of iodine 125 brachytherapy for choroidal melanoma: Twelve-yeare mortality rates and prognostic factors: COMS Report No. 28. Evidence-Based Eye Care 2007;8:156–8.

[19] McCauley Cutsinger S, Forsman R, Corner S, Deufel CL. Experimental validation of a new COMS-like 24 mm eye plaque for the treatment of large ocular melanoma tumors. Brachytherapy 2019;18:890–7. https://doi.org/10.1016/j.brachy.2019.07.005.

[20] Melia M. Quality of life after iodine 125 brachytherapy vs enucleation for choroidal melanoma: 5-year results from the Collaborative Ocular Melanoma Study: COMS QOLS Report No. 3. Arch Ophthalmol 2006.

[21] Nanda S, Reynolds S, Kaiser P. Ten-year follow-up of fellow eyes of patients enrolled in Collaborative Ocular Melanoma Study randomized trials: COMS report no. 22. Evidence-Based Eye Care 2004;5:206–7.

[22] Lee YC, Lin SC, Kim Y. A practical approach to estimating optic disc dose and macula dose without treatment planning in ocular brachytherapy using 125I

COMS plaques. Radiat Oncol 2018;13:1–11. https://doi.org/10.1186/s13014-018-1166-z.

[23] Nag S, Quivey JM, Earle JD, Followill D, Fontanesi J, Finger PT. The American Brachytherapy Society recommendations for brachytherapy of uveal melanomas. Int J Radiat Oncol Biol Phys 2003;56:544–55. https://doi.org/10.1016/S0360-3016(03)00006-3.

[24] Rivard MJ, Coursey BM, DeWerd LA, Hanson WF, Huq MS, Ibbott GS, et al. Update of AAPM Task Group No. 43 Report: A revised AAPM protocol for brachytherapy dose calculations. Med Phys 2004;31:633–74. https://doi.org/10.1118/1.1646040.

[25] King RP. Geometry function of a linear brachytherapy source. J Appl Clin Med Phys 2001;2:69. https://doi.org/10.1120/1.1349413.

[26] Peddada K V., Sangani R, Menon H, Verma V. Complications and adverse events of plaque brachytherapy for ocular melanoma. J Contemp Brachytherapy 2019;11:392–7. https://doi.org/10.5114/jcb.2019.87407.

[27] Pilotto E, Vujosevic S, De Belvis V, Parrozzani R, Boccassini B, Midena E. Long-term choroidal vascular changes after iodine brachytherapy versus transpupillary thermotherapy for choroidal melanoma. Eur J Ophthalmol 2009;19:646–53. https://doi.org/10.1177/112067210901900420.

[28] Sagoo M, Shields CL, Emrich J, Mashayekhi A, Komarnicky L, Shields JA. Plaque radiotherapy for juxtapapillary choroidal melanoma: treatment

complications and visual outcomes in 650 consecutive cases. JAMA Opthalmol 2014;132:697–702. https://doi.org/10.1001/jamaophthalmol.2014.111 Full text linksCite.

[29] Takiar V, Voong KR, Gombos DS, Mourtada F, Rechner LA, Lawyer AA, et al. A choice of radionuclide: Comparative outcomes and toxicity of ruthenium-106 and iodine-125 in the definitive treatment of uveal melanoma. Pract Radiat Oncol 2015;5:e169–76. https://doi.org/10.1016/j.prro.2014.09.005.

[30] Puusaari I, Heikkonen J, Kivelä T. Effect of radiation dose on ocular complications after iodine brachytherapy for large uveal melanoma: Empirical data and simulation of collimating plaques. Investig Ophthalmol Vis Sci 2004;45:3425–34. https://doi.org/10.1167/iovs.04-0066.

[31] Shields JA, Shields CL, De Potter P, Cu-Unjieng A, Hernandez C, Brady LW. Plaque radiotherapy for uveal melanoma. Int Ophthalmol Clin 1993;33:129–35. https://doi.org/10.1097/00004397-199303330-00018.

[32] Miguel D, De Frutos-Baraja JM, López-Lara F, Saornil MA, García-Álvarez C, Alonso P, et al. Radiobiological doses, tumor, and treatment features influence on local control, enucleation rates, and survival after episcleral brachytherapy. A 20-year retrospective analysis from a single-institution: Part I. J Contemp Brachytherapy 2018;10:337–46. https://doi.org/10.5114/jcb.2018.77849.

[33] Wagner A, Chen A, Cook T, Faber D, Winward K, Sause W. Outcomes and Control Rates for I-125 Plaque Brachytherapy for Uveal Melanoma: A

Community-Based Institutional Experience. ISRN Ophthalmol 2014;2014:1–7. https://doi.org/10.1155/2014/950975.

[34] Oliver SCN, Leu MY, DeMarco JJ, Chow PE, Lee SP, McCannel TA. Attenuation of iodine 125 radiation with vitreous substitutes in the treatment of uveal melanoma. Arch Ophthalmol 2010;128:888–93. https://doi.org/10.1001/archophthalmol.2010.117.

[35] Emami B. Tolerance of Normal Tissue to Irradiation. Int J Radiat Oncol Biol Phys 1991;21:109–22.

[36] Cruess AF, Augsburger JJ, Shields JA, Donoso LA, Amsel J. Visual Results Following Cobalt Plaque Radiotherapy for Posterior Uveal Melanomas. Ophthalmology 1984;91:131–6. https://doi.org/10.1016/S0161-6420(84)34317-2.

[37] COMS Group. Incidence of Cataract and Outcomes after Cataract Surgery in the First 5 Years after Iodine 125 Brachytherapy in the Collaborative Ocular Melanoma Study COMS Report No. 27. Ophthalmology 2007;114:1363–71. https://doi.org/https://doi.org/10.1016/j.ophtha.2006.10.039.

[38] Leonard KL, Gagne NL, Mignano JE, Duker JS, Bannon EA, Rivard MJ. A 17-year retrospective study of institutional results for eye plaque brachytherapy of uveal melanoma using 125I, 103Pd, and 131Cs and historical perspective. Brachytherapy 2011;10:331–9. https://doi.org/10.1016/j.brachy.2011.01.006.

[39] Henk JM, Whitelocke RAF, Warrington AP, Bessell EM. Radiation dose to the lens and cataract formation. Int J Radiat Oncol Biol Phys 1993;25:815–20.

https://doi.org/10.1016/0360-3016(93)90310-R.

[40] Nguyen SM, Sison J, Jones M, Berry J, Kim J, Murphree A, et al. Lens Dose-Response Prediction Modeling and Cataract Incidence in Patients With Retinoblastoma After Lens-Sparing or Whole-Eye Radiation Therapy. Int J Radiat Oncol Biol Phys 2019;103:1143–50. https://doi.org/doi:10.1016/j.ijrobp.2018.12.004.

[41] Radin PP, Lumbroso-Le Rouic L, Levy-Gabriel C, Dendale R, Sastre X, Desjardins L. Scleral necrosis after radiation therapy for uveal melanomas: Report of 23 cases. Graefe's Arch Clin Exp Ophthalmol 2008;246:1731–6. https://doi.org/10.1007/s00417-008-0920-6.

[42] Kaliki S, Shields CL, Rojanaporn D, Badal J, Devisetty L, Emrich J, et al. Scleral necrosis after plaque radiotherapy of uveal melanoma: A case-control study. Ophthalmology 2013;120:1004–11. https://doi.org/10.1016/j.ophtha.2012.10.021.

[43] Melia BM, Abramson DH, Albert DM, Boldt HC, Earle JD, Hanson WF, et al. Collaborative Ocular Melanoma Study (COMS) randomized trial of I-125 brachytherapy for medium choroidal melanoma: I. Visual acuity after 3 years, COMS Report No. 16. Ophthalmology 2001;108:348–66. https://doi.org/10.1016/S0161-6420(00)00526-1.

[44] Finger PT, Ho TK, Fastenberg DM, Hyman RA, Stroh EM, Packer S, et al. Intraocular radiation blocking. Investig Ophthalmol Vis Sci 1990;31:1724–30.

[45] McCannel TA, McCannel CA. Iodine 125 brachytherapy with vitrectomy and

silicone oil in the treatment of uveal melanoma: 1-to-1 matched case-control series. Int J Radiat Oncol Biol Phys 2014;89:347–52. https://doi.org/10.1016/j.ijrobp.2014.02.021.

[46] Ahuja Y, Kapoor KG, Thomson RM, Furutani KM, Shultz RW, Stafford SL, et al. The effects of intraocular silicone oil placement prior to iodine 125 brachytherapy for uveal melanoma: A clinical case series. Eye 2012;26:1487–9. https://doi.org/10.1038/eye.2012.158.

[47] Attix FH. Introduction to Radiological Physics and Radiation Dosimetry. 1st ed. Wiley-VCH Verlag GmbH & Co. KGaA, Weinheim; 1986.

[48] Rezaei H, Zabihzadeh M, Ghorbani M, Goli Ahmadabad F, Mostaghimi H. Evaluation of dose enhancement in presence of gold nanoparticles in eye brachytherapy by 103Pd source. Australas Phys Eng Sci Med 2017;40:545–53. https://doi.org/10.1007/s13246-017-0555-1.

[49] Masse F, Ouellette M, Lamoureux G, Boisselier E. Gold nanoparticles in ophthalmology. Med Res Rev 2019;39:302–27. https://doi.org/10.1002/med.21509.

[50] Reichstein D. Current treatments and preventive strategies for radiation retinopathy. Curr Opin Ophthalmol 2015;26:157–66. https://doi.org/10.1097/ICU.0000000000000141.

[51] Finger PT, Chin KJ, Semenova EA. Intravitreal anti-VEGF therapy for macular radiation retinopathy: a 10-year study. Eur J Ophthalmol 2016;26:60–6.

https://doi.org/10.5301/ejo.5000670.

[52] Mason JO, Albert MA, Persaud TO, Vail RS. Intravitreal bevacizumab treatment for radiation macular edema after plaque radiotherapy for choroidal melanoma. Retina 2007;27:903–7. https://doi.org/10.1097/IAE.0b013e31806e6042.

[53] Henein C, Awwad S, Ibeanu N, Vlatakis S, Brocchini S, Khaw PT, et al. Hydrodynamics of intravitreal injections into liquid vitreous substitutes. Pharmaceutics 2019;11:1–19. https://doi.org/10.3390/pharmaceutics11080371.

[54] Yang J, Manson D, Marr BP, Carvajal RD. Treatment of uveal melanoma: where are we now? Ther Adv Med Oncol 2018;10:1–17. https://doi.org/10.1177/1758834018757175.

[55] Mishra KK. Particle thearpy is ideal for the treatment of ocular malenomas (Point - Counterpoint). Med Phys 2016;43:631–4. https://doi.org/http://dx.doi.org/10.1118/1.4939223.

[56] Char DH, Kroll SM, Castro J, Friedman AH, Robertson DM. Long-term follow-up after uveal melanoma charged particle therapy. Trans Am Ophthalmol Soc 1997;95:171–91.

[57] Gragoudas ES. Proton beam irradiation of uveal melanomas: The first 30 years. The Weisenfeld lecture. Investig Ophthalmol Vis Sci 2006;47:4666–73. https://doi.org/10.1167/iovs.06-0659.

[58] Damato B, Kacperek A, Errington D, Heimann H. Proton beam radiotherapy of uveal melanoma. Saudi J Ophthalmol 2013;27:151–7.

https://doi.org/10.1016/j.sjopt.2013.06.014.

[59] Peeters A, Grutters JPC, Pijls-Johannesma M, Reimoser S, De Ruysscher D, Severens JL, et al. How costly is particle therapy? Cost analysis of external beam radiotherapy with carbon-ions, protons and photons. Radiother Oncol 2010;95:45–53. https://doi.org/10.1016/j.radonc.2009.12.002.

[60] Parker T, Rigney G, Kallos J, Stefko ST, Kano H, Niranjan A, et al. Gamma knife radiosurgery for uveal melanomas and metastases: a systematic review and meta-analysis. Lancet Oncol 2020;21:1526–36. https://doi.org/10.1016/S1470-2045(20)30459-9.

[61] Boone J, McNitt-Gray MF, Hernandez A. Monte Carlo Basics for Radiation Dose Assessment in Diagnostic Radiology. J Am Coll Radiol 2017;14:793–4. https://doi.org/10.1016/j.jacr.2017.02.010.

[62] Andreo P. Monte Carlo simulations in radiotherapy dosimetry. Radiat Oncol 2018;13:1–15. https://doi.org/10.1186/s13014-018-1065-3.

[63] Harrison RL. Introduction to Monte Carlo simulation. AIP Conf Proc 2009;1204:17–21. https://doi.org/10.1063/1.3295638.

[64] Allison J, Amako K, Apostolakis J, Araujo H, Dubois PA, Asai M, et al. Geant4 developments and applications. IEEE Trans Nucl Sci 2006;53:270–8. https://doi.org/10.1109/TNS.2006.869826.

[65] Allison J, Amako K, Apostolakis J, Arce P, Asai M, Aso T, et al. Recent developments in GEANT4. Nucl Instruments Methods Phys Res Sect A Accel

Spectrometers, Detect Assoc Equip 2016;835:186–225. https://doi.org/10.1016/j.nima.2016.06.125.

[66] Agostinelli S, Allison J, Amako K, Apostolakis J, Araujo H, Arce P, et al. GEANT4 - A simulation toolkit. Nucl Instruments Methods Phys Res Sect A Accel Spectrometers, Detect Assoc Equip 2003;506:250–303. https://doi.org/10.1016/S0168-9002(03)01368-8.

[67] Sechopoulos I, Rogers DWO, Bazalova-Carter M, Bolch WE, Heath EC, McNitt-Gray MF, et al. RECORDS: Improved Reporting of montE CarlO RaDiation transport Studies: Report of the AAPM Research Committee Task Group 268. Med Phys 2018;45:e1–5. https://doi.org/10.1002/mp.12702.

[68] Niroomand-Rad A, Blackwell CR, Coursey BM, Gall KP, Galvin JM, McLaughlin WL, et al. Radiochromic film dosimetry: Recommendations of AAPM Radiation Therapy Committee Task Group 55. Med Phys 1998;25:2093–115. https://doi.org/10.1118/1.598407.

[69] McLaughlin WL, Yun-Dong C, Soares CG, Miller A, Van Dyk G, Lewis DF. Sensitometry of the response of a new radiochromic film dosimeter to gamma radiation and electron beams. Nucl Inst Methods Phys Res A 1991;302:165–76. https://doi.org/10.1016/0168-9002(91)90506-L.

[70] Niroomand-Rad A, Chiu-Tsao S, Grams MP, Lewis DF, Soares CG, Van Battum LJ, et al. Radiochromic Film Dosimetry: An Update to TG-55. Med Phys 2020. https://doi.org/10.1002/mp.14497.

[71] Wu K, Su D, Liu J, Saha R, Wang JP. Magnetic nanoparticles in nanomedicine: A review of recent advances. Nanotechnology 2019;30. https://doi.org/10.1088/1361-6528/ab4241.

[72] Wong J, Prout J, Seifalian A. Magnetic Nanoparticles: New Perspectives in Drug Delivery. Curr Pharm Des 2017;23:2908–17. https://doi.org/10.2174/1381612823666170215104659.

[73] Spirou S V., Basini M, Lascialfari A, Sangregorio C, Innocenti C. Magnetic hyperthermia and radiation therapy: Radiobiological principles and current practice. Nanomaterials 2018;8:1–22. https://doi.org/10.3390/nano8060401.

[74] Giannaccini M, Giannini M, Calatayud MP, Goya GF, Cuschieri A, Dente L, et al. Magnetic nanoparticles as intraocular drug delivery system to target Retinal Pigmented Epithelium (RPE). Int J Mol Sci 2014;15:1590–605. https://doi.org/10.3390/ijms15011590.

[75] Zhou J, Hou J, Rao J, Zhou C, Liu Y, Gao W. Magnetically directed enzyme/prodrug prostate cancer therapy based on β-glucosidase/amygdalin. Int J Nanomedicine 2020;15:4639–57. https://doi.org/10.2147/IJN.S242359.

[76] Chang D, Lim M, Goos JACM, Qiao R, Ng YY, Mansfeld FM, et al. Biologically targeted magnetic hyperthermia: Potential and limitations. Front Pharmacol 2018;9. https://doi.org/10.3389/fphar.2018.00831.

[77] Stephen Z, Kievit FM, Zhang M. Magnetite Nanoparticles for Medical MR Imaging. Mater Today 2011;14:330–8. https://doi.org/10.1038/jid.2014.371.

[78] Holligan DL, Gillies GT, Dailey JP. Magnetic guidance of ferrofluidic nanoparticles in an in vitro model of intraocular retinal repair. Nanotechnology 2003;14:661–6. https://doi.org/10.1088/0957-4484/14/6/318.

[79] Mefford OT, Woodward RC, Goff JD, Vadala TP, St. Pierre TG, Dailey JP, et al. Field-induced motion of ferrofluids through immiscible viscous media: Testbed for restorative treatment of retinal detachment. J Magn Magn Mater 2007;311:347–53. https://doi.org/10.1016/j.jmmm.2006.10.1174.

[80] Riffle JS, Thompson Mefford O, Carroll MRJ, Vadala ML, Goff JD, Mejia-Ariza R, et al. Size analysis of PDMS-magnetite nanoparticle complexes: Experiment and theory. Chem Mater 2008;20:2185–91. https://doi.org/10.1021/cm702730p.

[81] Dailey JP, Phillips JP, Li C, Riffle JS. Synthesis of silicone magnetic fluid for use in eye surgery. J Magn Magn Mater 1999;194:140–8. https://doi.org/10.1016/S0304-8853(98)00562-9.

[82] Häfeli UO, Riffle JS, Harris-Shekhawat L, Carmichael-Baranauskas A, Mark F, Dailey JP, et al. Cell uptake and in vitro toxicity of magnetic nanoparticles suitable for drug delivery. Mol Pharm 2009;6:1417–28. https://doi.org/10.1021/mp900083m.

[83] Häfeli UO, Pauer GJ. In vitro and in vivo toxicity of magnetic microspheres. J Magn Magn Mater 1999;194:76–82. https://doi.org/10.1016/S0304-8853(98)00560-5.

[84] Zysler R, Berra A, Gurman P, Auciello O, Saravia M. Material for Medical Use

comprising Nanoparticles with Superparamagnetic Properties and Its Utilization in Surgery. U.S. Patent 20130225906, 2013.

[85] Raju HB, Hu Y, Vedula A, Dubovy SR, Goldberg JL. Evaluation of magnetic micro- and nanoparticle toxicity to ocular tissues. PLoS One 2011;6. https://doi.org/10.1371/journal.pone.0017452.

[86] ISO 10993: Biological evaluation of medical devices. 2018.

[87] Goode J. Use of International Standard ISO 10993-1, "Biological evaluation of medical devices - Part 1: Evaluation and testing within a risk management process." Dep Heal Hum Serv Food Drug Adm 2016:68. https://doi.org/http://www.fda.gov/downloads/medicaldevices/deviceregulationandguidance/guidancedocuments/ucm348890.pdf.

[88] COMSOL Mutliphysics n.d.

[89] Meaning of blindness as defined in the law. United States: 1980.

[90] Kline R. Coordinate localization of eye plaque for Collaborative Ocular Melanoma Study (COMS) n.d. http://rpc.mdanderson.org/rpc/credentialing/COMS.htm (accessed February 28, 2022).

[91] Althouse AD. Adjust for Multiple Comparisons? It's Not That Simple. Ann Thorac Surg 2016;101:1644–5. https://doi.org/10.1016/j.athoracsur.2015.11.024.

[92] Nath R, Anderson LL, Luxton G, Weaver K, Williamson JF, Meigooni AS. Dosimetry of interstitial brachytherapy sources: Recommendations of the AAPM Radiation Therapy Committee Task Group No. 43. Med Phys 1994;22:209–34.

https://doi.org/https://doi.org/10.1118/1.597458.

[93] Oare CC, Deufel CL, McCauley Cutsinger J, De La Fuente Herman T, Ferreira C. On the importance of quality assurance (QA) for COMS eye plaque Silastic inserts: A guide to measurement methods, typical variations, and an example of how QA intercepted a manufacturing aberration. J Appl Clin Med Phys 2021;22:72–82. https://doi.org/10.1002/acm2.13325.

[94] Niroomand-Rad A, Chiu-Tsao ST, Grams MP, Lewis DF, Soares CG, Van Battum LJ, et al. Report of AAPM Task Group 235 Radiochromic Film Dosimetry: An Update to TG-55. Med Phys 2020;47:5986–6025. https://doi.org/10.1002/mp.14497.

[95] Arce P, Ignacio Lagares J, Harkness L, Pérez-Astudillo D, Cañadas M, Rato P, et al. Gamos: A framework to do Geant4 simulations in different physics fields with an user-friendly interface. Nucl Instruments Methods Phys Res Sect A Accel Spectrometers, Detect Assoc Equip 2014;735:304–13. https://doi.org/10.1016/j.nima.2013.09.036.

[96] Arce P, Rato P, Cañadas M, Lagares JI. GAMOS: A GEANT4-based easy and flexible framework for nuclear medicine applications. IEEE Nucl Sci Symp Conf Rec 2008:3162–8. https://doi.org/10.1109/NSSMIC.2008.4775023.

[97] Meigooni AS, Hayes JL, Zhang H, Sowards K. Experimental and theoretical determination of dosimetric characteristics of IsoAid ADVANTAGE™ 125I brachytherapy source. Med Phys 2002;29:2152–8.

https://doi.org/10.1118/1.1500395.

[98] Rivard MJ, Melhus CS, Kirk BL. Brachytherapy dosimetry parameters calculated for a new 103Pd source. Med Phys 2004;31:2466–70. https://doi.org/10.1118/1.1781552.

[99] Taylor REP, Yegin G, Rogers DWO. Benchmarking BrachyDose: Voxel based EGSnrc Monte Carlo calculations of TG-43 dosimetry parameters. Med Phys 2007;34:445–57. https://doi.org/10.1118/1.2400843.

[100] Bronskill MJ, Carson PL, Einstein S, Koshinen M, Lassen M, Mun SK, et al. Site Planning for Magnetic Resonance - Report of AAPM NMR Task Group No. 20. New York, NY: 1987.

[101] Gunduz K, Shields CL, Shields JA, Cater J, Freire JE, Brady L V. Radiation retinopathy following plaque radiotherapy for posterior uveal melanoma. Arch Ophthalmol 1999;117:609–14. https://doi.org/10.1001/archopht.117.5.609.

[102] Espensen CA, Appelt AL, Fog LS, Gothelf AB, Thariat J, Kiilgaard JF. Predicting visual acuity deterioration and radiation-induced toxicities after brachytherapy for choroidal melanomas. Cancers (Basel) 2019;11. https://doi.org/10.3390/cancers11081124.

[103] Group. COMS. Ten-year follow up of fellow eyes enrolled in Colaborative Ocular Melanoma Study randomized trials: COMS report no. 22. Ophthalmology 2004;5:206–7. https://doi.org/10.1016/j.ophtha.2003.08.029.

[104] Rivard MJ, Butler WM, DeWerd LA, Huq MS, Ibbott GS, Meigooni AS, et al.

Supplement to the 2004 update of the AAPM Task Group No. 43 Report. Med Phys 2007;34:2187–205. https://doi.org/10.1118/1.2736790.

[105] Solberg TD. Dosimetric parameters of three new solid core I-125 brachytherapy sources. J Appl Clin Med Phys 2002;3:119. https://doi.org/10.1120/1.1464086.

[106] Fardi Z, Taherparvar P. A Monte Carlo investigation of the dose distribution for new I-125 Low Dose Rate brachytherapy source in water and in different media. Polish J Med Phys Eng 2019;25:15–22. https://doi.org/10.2478/pjmpe-2019-0003.

[107] Zaker N, Zehtabian M, Sina S, Koontz C, Meigooni AS. Comparison of TG-43 dosimetric parameters of brachytherapy sources obtained by three different versions of MCNP codes. J Appl Clin Med Phys 2016;17:379–90. https://doi.org/10.1120/jacmp.v17i2.5797.

[108] DeWerd LA, Ibbott GS, Meigooni AS, Mitch MG, Rivard MJ, Stump KE, et al. A dosimetric uncertainty analysis for photon-emitting brachytherapy sources: Report of AAPM Task Group No. 138 and GEC-ESTRO. Med Phys 2011;38:782–801. https://doi.org/10.1118/1.3533720.

[109] Thomson RM, Furutani KM, Kaulich TW, Mourtada F, Rivard MJ, Soares CG, et al. AAPM recommendations on medical physics practices for ocular plaque brachytherapy: Report of task group 221. Med Phys 2020;47:e92–124. https://doi.org/10.1002/mp.13996.

[110] Meigooni AS, Dini SA, Sowards K, Hayes JL, Al-Otoom A. Experimental determination of the TG-43 dosimetric characteristics of Echoseed™ model 6733

125I brachytherapy source. Med Phys 2002;29:939–42. https://doi.org/10.1118/1.1470210.

[111] Geant4 Reference Physics Manual. version 10. n.d.

APPENDIX: MONTE CARLO SIMULATIONS

Table A.1 Monte Carlo simulation parameters

Item Name	Description	Reference
Code, Version	Geant4 GAMOS, Version 6.1.0 (2020)	[64,95,96]
Validation	Previously validated	
Timing	CPU time was on the order of 10^3 minutes	
Source Description	^{125}I Spectrum Obtained from TG-43U1 Geometry: Silver core cylinder (diameter: 0.5 mm, length: 3 mm) with a 1 μm silver halide layer evenly distributed with ^{125}I. The source is sealed inside a titanium cylinder (diameter: 0.8 mm, length: 4.5 mm, thickness: 0.05 mm), with rounded titanium ends (thickness: 0.05 mm). The source is filled with air (40% humidity). Materials: composition based on NIST definitions	[24,104,105,110]
Cross-sections	GmEMExtendedPhysics list	[111]
Transport Parameters	Range cuts: 0.0001 mm	
Variance reduction techniques used	NA	
Scored Quantities	GmG4PSDoseDeposit in the geometry or voxel of interest Voxel sizes: 0.1 x 0.1 x 0.1 mm^3 at $r \leq 1$ cm 0.5 x 0.5 x 0.5 mm^3 at $3 \leq r < 5$ cm 1 x 1 x 1 mm^3 at $r > 5$ cm	
Statistical uncertainty	1 x 10^9 runs (histories) Type A uncertainties < 0.1% at $r \leq 5$ cm <0.5% at $r > 5$ cm	
Statistical Methods	NA	
Post-Processing	Conversion of Gy/Event to Gy by calculating the number of events (i.e., photons) emitted from an ^{125}I source with known exposure time and activity.	

Template obtained from AAPM TG-268 [67]

Sample GAMOS Input for Homogenous Geometry for a 20 mm COMS Plaque

The following Input, Geometry, and Parallel Geometry files are used in GAMOS version 6.1.0 to measure vertical dose distribution with a modeled 20 mm COMS plaque and 24 ^{125}I sources. The source and COMS plaque geometries are each described per manufacturer specifications in TG-43U1S1, and TG-129 [5,104].

INPUT FILE:

```
#Call relevant geometry files
/gamos/setParam GmGeometryFromText:FileName world2_phantom.geom
/gamos/setParam GmGeometryFromText:FileNameParallel sources.geom 1
/gamos/setParam GmPhysicsParallel:LayeredMaterial 1
/gamos/geometry GmGeometryFromText

#Random number generator
/gamos/random/setSeeds 1001 1001

#Choose physics list
/gamos/physicsList GmEMExtendedPhysics
/gamos/generator GmGenerator

#Set energy cuts (range) to 0.0001 mm for low energy Iodine
/run/setCut 0.0001
/run/initialize

#Add physics processes
/gamos/physics/addParallelProcess
/gamos/physics/addPhysics decay
/gamos/physics/addPhysics radioactiveDecay

#Source distributed in geant4 volume
/gamos/generator/addIsotopeSource myIodineSource I125 0.0021*Ci
/gamos/generator/positionDist myIodineSource GmGenerDistPositionInG4Volumes mySource
RCap LCap

#Calculate Dose
/gamos/scoring/createMFDetector detector phantom
/gamos/scoring/addScorer2MFD scorer GmG4PSDoseDeposit detector
/gamos/scoring/addPrinter2Scorer GmPSPrinter3ddose scorer
/gamos/scoring/addPrinter2Scorer GmPSPrinterCout scorer

#Run 10^9 Events (Histories)
/run/beamOn 1000000000
```

GEOMETRY FILE:

```
// Build World
:VOLU world BOX 20.*cm 20.*cm 20.*cm G4_WATER

// Build Medium Properties
:MIXT modulay 15.8 4
  Au 0.77
  Ag 0.14
  Cu 0.08
  Pd 0.01

:MIXT silastic 1.12 5
  Si 0.399
  O 0.289
  C 0.249
  H 0.063
  Pt 0.00005

// Build Geometry
:ROTM RM0 0. 0. 0.

//Silastic Insert
:SOLID silastic1 SPHERE 12.3*mm 14.55*mm 0 360 0 90
:SOLID tube 10*mm 30*mm 30*mm
:SOLID silastic_insert1 SUBTRACTION silastic1 tube RM0 0 0 0
:VOLU silastic_insert silastic_insert1 silastic
:PLACE silastic_insert 1 world RM0 0 0 -11.3

//Gold Alloy Backing
:SOLID backing1 SPHERE 14.55*mm 15.05*mm 0 360 0 90
:SOLID tube2 TUBE 10.5*mm 30*mm 30*mm
:VOLU backing SUBTRACTION backing1 tube2 RM0 0 0 0 modulay
:VOLU ring TUBE 10*mm 10.5*mm 1.5*mm modulay

:PLACE backing 1 world RM0 0 0 -11.3
:PLACE ring 1 backing RM0 0 0 8.6
:COLOR backing 0 0 0
:COLOR ring 0 0 0

//Dose scoring geometry, perpendicular to plaque, 0.5 x 0.5 x 0.5 mm3 voxels
:VOLU phantom_container BOX 15*mm 15*mm 0.25 G4_WATER
:PLACE phantom_container 1 world RM0 0 0 -11.3
:VOLU phantom BOX 0.25 0.25 0.25 G4_WATER
:PLACE_PARAM phantom 1 phantom_container PHANTOM 60 60 1 1 1 1
```

PARALLEL GEOMETRY FILE (SOURCES):

```
//Define Rotation Matrices for Seeds in 20 mm COMS Plaque
:ROTM RM22 0 0 0
:ROTM RM1 0. 90. 0.
:ROTM RM2 90. 200. 0.
:ROTM RM3 90. 240. 0.
:ROTM RM4 90. 280. 0.
:ROTM RM5 90. 320. 0.
:ROTM RM6 90. 40. 0.
:ROTM RM7 90. 80. 0.
:ROTM RM8 90. 120. 0.
:ROTM RM9 90. 160 0.
:ROTM RM10 90. 193. 0.
:ROTM RM11 90. 244. 0.
:ROTM RM12 90. 296. 0.
:ROTM RM13 90. 347. 0.
:ROTM RM14 90. 39. 0.
:ROTM RM15 90. 141. 0.
:ROTM RM16 90. 216. 0.
:ROTM RM17 90. 288. 0.
:ROTM RM18 90. 72. 0.
:ROTM RM19 90. 144. 0.
:ROTM RM20 90 270 0.
:ROTM RM21 90. 0 0

// Titanium Geometry
:SOLID central_tube TUBE 0.35 .4 1.85
:SOLID right_side SPHERE 0 0.4 0 360*degree 0 90*degree
:SOLID left_side SPHERE 0 0.4 0 360*degree 90*degree 180*degree

:SOLID seeda UNION central_tube right_side RM22 0 0. 1.85
:VOLU BRACHY_SOURCE UNION seeda left_side RM22 0 0. -1.85 G4_Ti

//Air in 40% humidity conditions according to TG43
:MIXT Air_Humid40 0.00120 5
  G4_H   0.000732
  G4_C   0.000123
  G4_N   0.750325
  G4_O   0.236077
  G4_Ar  0.012743

//Create Air in tube cavity
:VOLU central_air TUBE 0 .35 1.85 Air_Humid40
:PLACE central_air 1 BRACHY_SOURCE RM22 0 0 0
:VOLU right_air SPHERE 1 1.25 0 360*degree 0*degree 16.26*degree Air_Humid40
:PLACE right_air 1 BRACHY_SOURCE RM22 0 0 0.65
:VOLU left_air SPHERE 1 1.25 0 360*degree 163.74*degree 180*degree Air_Humid40
:PLACE left_air 1 BRACHY_SOURCE RM22 0 0 -0.65
```

```
//Create silver marker
:VOLU  Marker    TUBE 0. 0.25 1.5 G4_Ag
:PLACE Marker    1 BRACHY_SOURCE RM22 0. 0. 0.
:COLOR Marker    1 1 0
:VIS Marker ON

// Create I125 Layer, 0.1 micrometer deposited on silver iodide
:VOLU mySource TUBE 0.25 0.251 1.5 G4_SILVER_IODIDE
:PLACE mySource 1 BRACHY_SOURCE RM22 0. 0. 0.

//Create I125 Layer – End Caps
:VOLU LCap TUBE 0 0.251 0.0005 G4_SILVER_IODIDE
:PLACE LCap 1 BRACHY_SOURCE RM22 0. 0. -1.5005
:VOLU RCap TUBE 0 0.251 0.0005 G4_SILVER_IODIDEq     1
:PLACE RCap 1 BRACHY_SOURCE RM22 0. 0. 1.5005

:COLOR BRACHY_SOURCE 1 0 1
:VIS BRACHY_SOURCE ON

// Place seeds in location according to TG-129
// 0 0 0 is the inner sclera.
:PLACE BRACHY_SOURCE 1 world RM2 -8.08 -02.94 -0.64
:PLACE BRACHY_SOURCE 2 world RM3 -4.30 -7.45 -0.64
:PLACE BRACHY_SOURCE 3 world RM4 1.49 -8.47 -0.64
:PLACE BRACHY_SOURCE 4 world RM5 6.59 -5.53 -0.64
:PLACE BRACHY_SOURCE 5 world RM21 8.60 0 -0.64
:PLACE BRACHY_SOURCE 6 world RM6 6.59 5.53 -0.64
:PLACE BRACHY_SOURCE 7 world RM7 1.49 8.47 -0.64
:PLACE BRACHY_SOURCE 8 world RM8 -4.30 7.45 -0.64
:PLACE BRACHY_SOURCE 9 world RM9 -8.08 02.94 -0.64
:PLACE BRACHY_SOURCE 10 world RM10 -6.53 -1.49 0.65
:PLACE BRACHY_SOURCE 11 world RM11 -2.91 -6.04 0.65
:PLACE BRACHY_SOURCE 12 world RM12 2.91 -6.04 0.65
:PLACE BRACHY_SOURCE 13 world RM13 6.53 -1.49 0.65
:PLACE BRACHY_SOURCE 14 world RM14 5.24 4.18 0.65
:PLACE BRACHY_SOURCE 15 world RM1 0 6.70 0.65
:PLACE BRACHY_SOURCE 16 world RM15 -5.24 4.18 0.65
:PLACE BRACHY_SOURCE 17 world RM16 -3.80 -2.76 1.57
:PLACE BRACHY_SOURCE 18 world RM17 1.45 -4.47 1.57
:PLACE BRACHY_SOURCE 19 world RM21 4.7 0 1.57
:PLACE BRACHY_SOURCE 20 world RM18 1.45 4.47 1.57
:PLACE BRACHY_SOURCE 21 world RM19 -3.80 2.76 1.57
:PLACE BRACHY_SOURCE 22 world RM20 0 -2.25 2.21
:PLACE BRACHY_SOURCE 23 world RM1 0 2.25 2.21
:PLACE BRACHY_SOURCE 24 world RM1 0. 0 2.40
```